SLAC – 319
UC – 28
(A)

PRODUCTION OF HIGH INTENSITY ELECTRON BUNCHES FOR THE SLAC LINEAR COLLIDER*

Mary Beth James

Stanford Linear Accelerator Center
Stanford University
Stanford, California 94305

August 1987

Prepared for the Department of Energy
under contract number DE-AC03-76SF00515

Printed in the United States of America. Available from the National Technical Information Service, U.S. Department of Commerce, 5285 Port Royal Road, Springfield, Virginia 22161. Price: Printed Copy A09, Microfiche A01.

* Ph.D. Dissertation

ABSTRACT

PRODUCTION OF HIGH INTENSITY ELECTRON BUNCHES FOR THE SLAC LINEAR COLLIDER

Mary Beth James
Department of Applied Physics
Stanford University
Stanford Linear Accelerator Center

This thesis describes the design and performance of a high intensity electron injector for the SLAC Linear Collider.

Motivation for the collider and the specifications for the injector are discussed. The specifications include:

- Two electron bunches, ~59 ns apart,
- For each bunch, 5×10^{10} electrons captured in one accelerator RF cycle,
- Bunch length and shape which result in a $\pm 1\%$ energy spectrum at a beam energy of 1.2 GeV,
- Invariant transverse emittance in both x- and y-planes no greater than 3×10^{-4} radian meters.

An analytic theory of the bunching and capture of electrons by RF fields is discussed in the limit of low space charge and small signal. The design and performance of SLAC's main injector are described to illustrate a successful application of this theory. The bunching and capture of electrons by RF fields are then discussed in the limit of high space charge and large signal, and a description of the design of the collider injector follows.

In the limit of high space charge forces and large RF signals, the beam dynamics are considerably more complex and numerical simulations are required to predict particle motion. A computer code which models the longitudinal dynamics of electrons in the presence of space charge and RF fields is described.

The results of the simulations, the resulting collider injector design and the various components which make up the collider injector are described. These include the gun, subharmonic bunchers, traveling-wave buncher and velocity-of-light accelerator section. Finally, the performance of the injector is described including the beam intensity, bunch length, transverse emittance and energy spectrum.

While the final operating conditions differ somewhat from the design, the performance of the collider injector is in good agreement with the numerical simulations and meets all of the collider specifications.

Acknowledgements

All accomplishments belong to many people; this effort is no exception. I thank Roger Miller for taking on an apprentice. I thank Jim Clendenin for being a good physicist and helping much more than he knows. I thank Roger Miller, Jim Clendenin, Joe Sodja and Jack Truher for building CID and teaching me most everything. I thank Ron Koontz, Larry Feathers, Jim Hodgers, Fred Hooker, George Leger and Boni Cordova for their support and friendship. I thank the people of MCC for help and comradery, especially in the wee hours. I thank the people of Accelerator Physics and the Test Lab for their support, patience, and boundless faith that this project would, indeed, come to an end some day.

I thank Gregory Loew for dragging me, kicking and screaming, toward a substantially more lucid description of this work. I thank Bette-Jane Ferandin for creating a beautiful manuscript from the harried scratches of a frazzled graduate student, and for her patience and poise under fire. I thank Barbara Woo for much patient help with the computer graphics. I thank the people of Technical Illustrations for reworking most of the figures three times.

I thank Alain Schwartzman for many a late night work session. I thank Rick Iverson for supporting me in all of the above endeavors and believing when I couldn't that this whole thing was a good idea. I thank Pat Burchat for being so graceful about finishing first.

I thank Marshall, Melissa, Linda, Deano, Roger, Lee, Howie, Mary S., Carina, Harry, Frank, Pat, Barb and Theo, Ric, Amy, Tony, Jeff, Jeanne, Matt, Peter, Jane B., Alain, Sue, Frances, Dave, the Ted Mac Amateur Hour, Michele, Eric, Mary Lu, Jane W., Paul, and Rick for making this task take much longer than it should have. To paraphrase Mark Twain, "Life is what happens while you're procrastinating, and a good life it is!"

Finally, God bless Mom, Dad, David, Tom, Peter, Ann and Catherine. Lucky me.

This work was supported by the U.S. Department of Energy under contract number DE-AC03-76SF00515.

TABLE OF CONTENTS

LIST OF TABLES

LIST OF FIGURES

CHAPTER 1.
INTRODUCTION

This thesis describes the design and performance of a high current, two-bunch electron injector. The injector is part of SLAC's new accelerator facility, the SLAC Linear Collider (SLC), in which 50 GeV electrons will be incident on 50 GeV positrons. The resulting 100 GeV in the center of mass will enable particle physicists to explore the spectroscopy of the Z^0 particle, as well as to investigate other physics.

Traditionally, colliding beam storage rings have been the mainstay of e^+e^- physics. Particles stored in storage rings lose energy to synchrotron radiation at a rate proportional to the fourth power of energy,

$$\frac{\textit{energy lost to synchrotron radiation}}{\textit{turn}} \propto \frac{\gamma^4}{R} \tag{1.1}$$

where γ is the normalized energy of the particle and R is the mean magnetic radius of the storage ring. To minimize the combined costs of capital and operating expenses, one normally chooses $R \propto \gamma^2$. Thus the RF power needed to replace energy lost to synchrotron radiation is proportional to γ^2. In linear colliders, losses due to synchrotron radiation are negligible. Both capital and operating (i.e., RF power) costs increase linearly with increasing energy. Figure 1.1 is a sketch of cost versus energy for storage rings and linear colliders. At some beam energy (though the exact energy is a matter of debate) linear colliders become more cost effective than storage rings.

The luminosity of colliding beam facilities can be expressed as

$$L = \frac{fN^-N^+}{4\pi\sigma_x\sigma_y} = \frac{fN^-N^+}{4\pi\sqrt{\epsilon_x\beta_x^*}\sqrt{\epsilon_y\beta_y^*}} \tag{1.2}$$

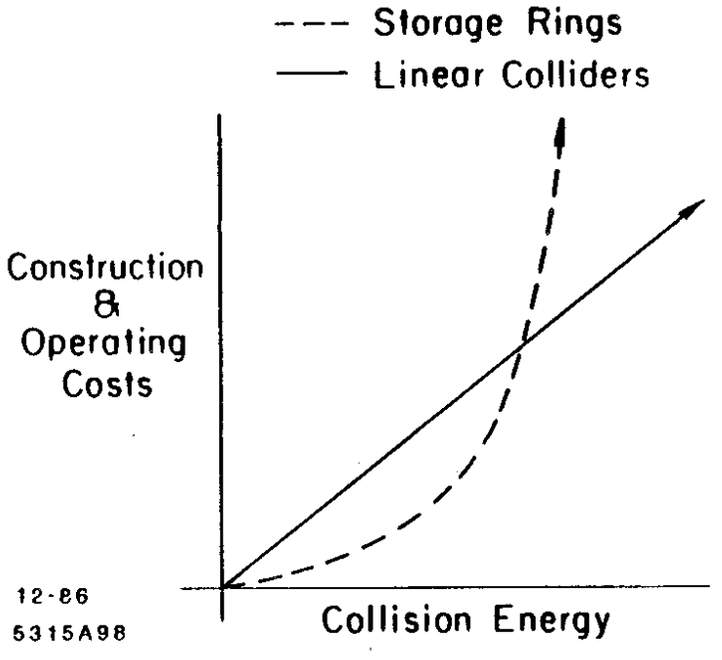

Fig. 1.1. Scaling of cost versus center-of-mass energy for storage rings and linear colliders.

where

f = number of beam collisions/second

N^- = number of electrons in a bunch

N^+ = number of positrons in a bunch

$\epsilon_x(\epsilon_y)$ = transverse emittance in horizontal (vertical) plane

$\beta_x^*(\beta_y^*)$ = beta function of the focusing lattice in the horizontal (vertical) plane at the interaction point

$\sigma_x(\sigma_y)$ = $\sqrt{\epsilon_x\beta_x^*}\,(\sqrt{\epsilon_y\beta_y^*})$ = horizontal (vertical) rms radius of a Gaussian bunch.

In the left-hand column of Table 1.1 the components contributing to the PEP storage ring luminosity are listed. In the right-hand column the specifications for achieving the design luminosity of the SLC are given. Note first that the frequency of beam collisions at PEP is approximately 4×10^5 per second. In contrast, the frequency of beam collisions in the SLC is limited by the repetition rate of the linac, which is at most 180 pps. Note also that the PEP bunches contain 3×10^{11} electrons or positrons per bunch. These bunches are made by "stacking" pulses from the linac. In the SLC, each linac electron bunch collides once with a positron bunch and is lost. The pre-SLC linac could produce and accelerate only 10^9 electrons and 10^8 positrons per bunch. These two effects combine to produce a loss of luminosity on the order of 2×10^9. As shown in Table 1.1, the loss in luminosity is recovered by increasing n, the number of electrons or positrons produced and accelerated in each bunch, by decreasing the transverse emittance of the beam in both planes, and by decreasing the value of the β function of the focusing lattice at the interaction point. The center column of Table 1.1 lists the major systems necessary to achieve each improvement in luminosity.

Table 1.1. Comparison of achieved luminosity at PEP with design luminosity at SLC.

PEP (Attained)	Systems Necessary to Achieve Satisfactory Luminosity	SLC (Specified)
$L = \frac{N^+N^-f}{4\pi\sigma^2} \cong \frac{2\times10^{31}}{cm^2 sec}$		$L = \frac{N^+N^-f}{4\pi\sigma^2} \cong \frac{1\times10^{30}}{cm^2 sec}$
$N^- = 3\times10^{11}$ $n = \frac{1\times10^9 e^-}{bunch}$ from linac	New Electron Source Linac Upgrade	$N^- = 5\times10^{10}$ $n = \frac{5\times10^{10} e^-}{bunch}$
$N^+ = 3\times10^{11}$ $n = \frac{1\times10^9 e^+}{bunch}$ from linac	New Positron Source Linac Upgrade	$N^+ = 5\times10^{10}$ $n = \frac{5\times10^{10} e^+}{bunch}$
$f = 4\times10^5 \frac{Beam\ Crossings}{sec}$		$f = 180 \frac{Beam\ Crossings}{sec}$
$\sigma_x\sigma_y \simeq 1.4\times10^{-4}$ cm^2		$\sigma^2 = 4\times10^{-8}$ cm^2
$\gamma\epsilon_x \simeq 3\times10^{-3}$ rad m $\gamma\epsilon_y \simeq 2\times10^{-4}$ rad m	Damping Rings Linac Upgrade	$\gamma\epsilon_x = 3\times10^{-5}$ rad m $\gamma\epsilon_y = 3\times10^{-5}$ rad m
$\beta_x = 2.7$ m $\beta_y = .11$ m	Final Focus	$\beta_x = .013$ m $\beta_y = .013$ m

SLAC's linear collider is shown in schematic form in Fig. 1.2. A detailed discussion of the design specifications and system descriptions can be found in Refs. 1 and 2. For our purposes, it is sufficient to give a brief description of the SLC so that the specifications of the electron injector can be placed in a proper context.

The SLC consists of

- A high current electron injector,
- Two small storage rings to damp the beams' transverse emittances,
- A high current positron source,
- An extensively upgraded linac,
- The collider arcs, and
- The final focus.

It is instructive to describe one complete cycle of collider operation.[3]

1. The electron injector produces two bunches, ~59 ns apart.
2. The bunches are accelerated through the first 100 meters of the accelerator, gaining energy to 1.21 GeV.
3. The bunches enter the north damping ring where their transverse phase space is reduced by a factor of ten in 5.5 ms.
4. The electron bunches are extracted from the ring, their bunch lengths compressed, and reinjected into the linac.
5. The two bunches are accelerated through approximately 1800 meters of linac gaining energy to 33 GeV.
6. The second electron bunch is diverted by a fast kicker and strikes the positron target (on the first two cycles of operation, the first e^- bunch is wasted).
7. Positrons of energy 2-20 MeV are captured and accelerated to 200 MeV.

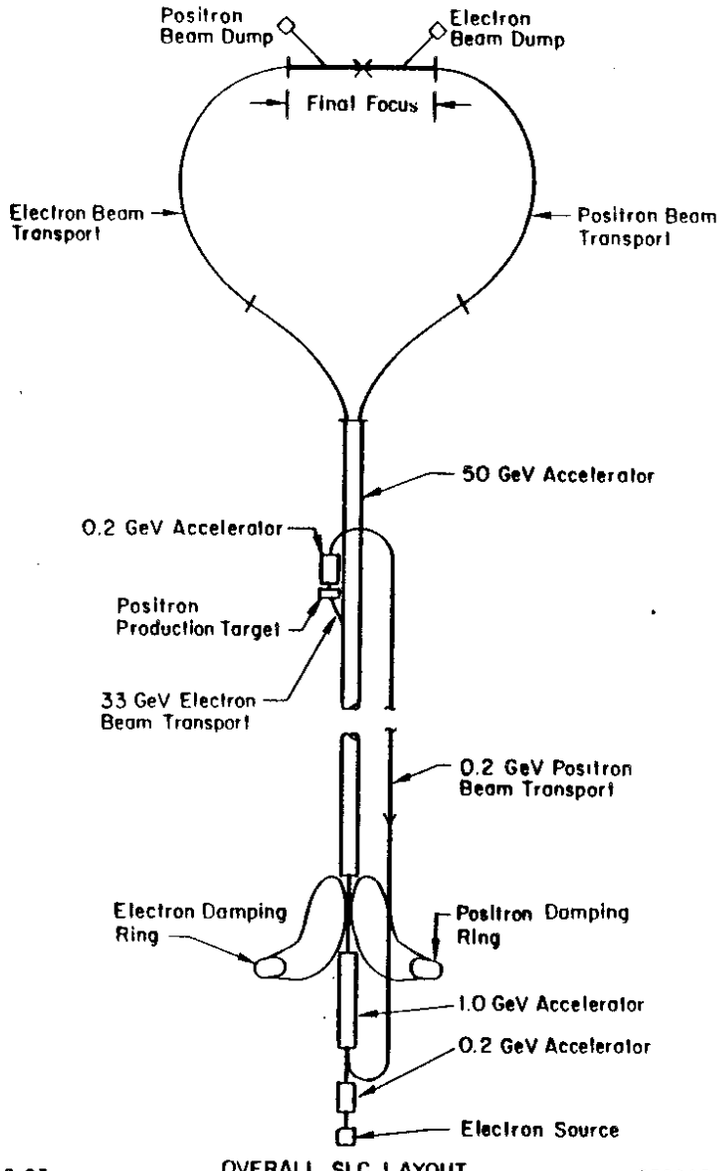

Fig.1.2. Schematic diagram of the SLAC Linear Collider.

8. The positrons are bent through 180° and transported back to the front of the linac, then bent through another 180° and injected into the linac.

9. Almost simultaneously the electron injector produces two more bunches of electrons and the three bunches are accelerated to 1.21 GeV.

10. The positron bunch enters the south damping ring where its transverse emittance damps for 11 ms (two machine pulses at 180 pps). Meanwhile the electron bunches enter the north damping ring and are damped for 5.5 ms.

11. After the 5.5 ms the two e^- bunches are extracted and steps 4 through 10 are repeated. The e^+ bunch so generated enters the south damping ring in a bucket on the opposite side of the ring from the first positron bunch.

12. The first e^+ bunch (now fully damped) is extracted from the south damping ring 5.5 ms later. The two e^- bunches are extracted from the north damping ring and all three bunches are accelerated, the first two bunches to 50 GeV.

13. The positron bunch is deflected into the south arc, the first e^- bunch into the north arc and the two collide at the interaction point where interesting physics is hopefully produced. The bunches are then discarded. The second e^- bunch is deflected at the 33 GeV point to produce the next positron bunch.

14. The cycle is repeated.

The goal of the collider injector is to prepare a high-intensity electron bunch whose six-dimensional emittance at the end of Sector 1 is within the damping ring acceptance. The six-dimensional damping ring acceptance is summarized in Table 1.2. The invariant transverse beam emittance in both the x and y planes must be no greater than 3×10^{-4} radian-meters. The energy acceptance of the damping ring is $\pm 1\%$.

Since the damping ring operates at the fourth subharmonic of the linac frequency, it is possible for the ring to capture two electron bunches accelerated by adjacent RF crests in the linac. However, in the linac the second bunch sees significantly different accelerating fields from the first. Should this difference exceed $\pm 1\%$, the two bunches would not fit within the damping rings energy acceptance.

Table 1.2. Damping ring acceptance.

ϵ_x	$\leq 3 \times 10^{-4}$ radian meters (invariant)
ϵ_y	$\leq 3 \times 10^{-4}$ radian meters (invariant)
E	$= 1.21$ GeV
$\Delta E/E$	$\leq \pm 1\%$
Bunch length	≤ 20 cm

To estimate the energy spread between two adjacent bunches, we write the power per unit length extracted from the linac by the first bunch as

$$\frac{dU}{dt} = \frac{dq}{dt} E \tag{1.3}$$

where

U = energy/unit length stored in the linac,
q = electron charge, and
E = electric field.

The electric field across a linac cavity as a function of energy stored per unit length is given by

$$E^2 = \omega \frac{r}{Q_0} U \tag{1.4}$$

where

ω = frequency of the RF fields, and
r/Q_0 = shunt impedance of the accelerating structure.

Combining (1.3) and (1.4) we have

$$\int \frac{dU}{\sqrt{U}} = \int dq \sqrt{\omega \frac{r}{Q_0}} \tag{1.5}$$

integrating we have

$$2\sqrt{U} = \sqrt{\omega \frac{r}{Q_0}}\, Q_{bunch}$$

where Q_{bunch} = total charge in the first e^- bunch. Rearranging and substituting $E = \sqrt{\omega (r/Q_0) U}$ we see that the change in the field seen by the second bunch due to energy extracted by the first bunch is

$$E_{BL} = \frac{1}{2} \omega \frac{r}{Q_0} Q_{bunch}$$

where we have assumed that the time between bunches is small compared to the filling time of the structure, but large enough that the higher order modes induced by the first bunch have lost coherence. This effect is known as beam loading.

For SLAC's accelerator structure, $r/Q_0 = 4.4\, k\Omega$/meter. For $Q_{bunch} = 2.5 \times 10^{10}\, e^-$

$$E_{BL} = .16 \frac{MeV}{meter}$$

The field gradient necessary to achieve 1.21 GeV at the damping ring is $E_{ACC} = 13.9$ MeV/meter. Thus the change in field seen by the second bunch is

$$\frac{E_{BL}}{E_{ACC}} = \frac{.16}{13.9} = 1.2\%$$

Given a 1.2% energy difference between the two bunches, for both to fall within the damping ring energy acceptance, each must have an internal energy spread no greater than $\pm 0.4\%$. As we shall later see, $\pm 0.4\%$ is an unrealistic upper limit on the bunches' internal energy spread.

Beam loading occurs within a single bunch as well as between bunches. As discussed in Chapter 2, we can mitigate beam loading in a single bunch by capturing the bunch forward of the RF crest. Using this technique, we can achieve an acceptable energy spread at the entrance to the damping ring provided we capture all 5×10^{10} electrons into a single RF cycle.

The acceptable longitudinal phase spread of the bunch at the end of the injector is limited not by the phase acceptance of the damping ring but by the fact that the phase spread and shape of the bunch determine the energy spread at the entrance to the damping rings.

We can now summarize the specifications of the collider injector. The specifications include:

- Two electron bunches, ~59 ns apart,
- For each bunch, 5×10^{10} electrons captured in one accelerator RF cycle,
- Bunch length and shape which result in a $\pm 1\%$ energy spectrum at a beam energy of 1.2 GeV,
- Invariant transverse emittance in both the x and y planes no greater than 3×10^{-4} radian meter.

This thesis is concerned with the problem of the longitudinal capture of high space charge single bunches.

In Section 2.1, we discuss an analytic theory of bunching and capture of electrons by RF fields in the low space charge, small signal limit.[4] We review Miller's[4,5] design of SLAC's first injector to illustrate a successful application of the theory.

In Section 2.2 we discuss the design of the collider injector, emphasizing that the design arose from considering the high space charge, large signal case as a perturbation of SLAC's successful solution to the low space charge, small signal bunching problem.

In the collider injector, space charge forces and large RF signals greatly complicate the beam dynamics. We must numerically simulate the beam dynamics to have confidence in our design strategy. In Section 2.3 we discuss a computer code which models the longitudinal dynamics of electrons in the presence of space charge and RF fields. In order to design a simple, one-dimensional model of the longitudinal beam dynamics, we make certain assumptions about the radial extent of the beam. In Section 2.4 we discuss radial focusing of the beam to achieve a stable beam radius throughout a given region. In addition, we present an approximate calculation which demonstrates that in this design a smaller longitudinal emittance results in transverse emittance growth.

In Section 3.1 we describe the components which make up the collider injector including the gun, subharmonic bunchers, traveling-wave buncher and velocity-of-light accelerator section. In Section 3.2 we compare the performance of the injector to its calculated performance. While the final operating conditions differ somewhat from the design, the performance is in good agreement with the numerical simulation and meets all of the collider specifications. Finally, in Section 3.3 we discuss radial emittance measurements and compare them to the expected emittance.

CHAPTER 2.
DESIGN OF CID, THE COLLIDER INJECTOR

2.1 Bunching in the Low Space Charge Limit

2.1.1 Low Space Charge Beam Dynamics

Before discussing longitudinal bunching in the presence of large space charge forces, it is instructive to review the dynamics of bunching in the low space charge limit. In both cases the problem is the same: a continuous stream of low energy electrons must be bunched into a small fraction of one RF wavelength. Each bunch must then be captured onto the accelerating RF wave. Our actual problem of longitudinal bunching in the presence of large space charge forces is considerably more complex than its low space charge counterpart, and computer simulations are necessary give us confidence in our design strategy. Because the Collider Injector Development (CID) design arose from considering the high current case as a perturbation of SLAC's successful solution to the low space charge bunching problem, a somewhat detailed discussion of buncher design in the low space charge limit is appropriate.

For low space charge beams, designers often employ tapered loaded waveguides with variable phase velocities and field strengths to accomplish bunching, but tapered waveguides must be "custom tailored" to specific initial parameters and desired output. Another approach is to design a bunching system where bunching and capture are accomplished by a series of constant phase velocity, constant field strength structures. This approach is more robust as the phases and field strengths of each component can be varied independently to compensate for minor design or fabrication errors and to optimize bunching over a range of gun voltages, klystron powers and waveguide temperatures. SLAC's low current injector designed by Miller[4,5] uses three bunching elements, a "gap-and-drift" prebuncher, a traveling-wave buncher with phase velocity less than c and a traveling-wave capture region whose velocity equals c.

With certain simplifying assumptions, we can derive analytic expressions for the z position and energy of electrons traversing these three structures. These expressions lead to longitudinal phase space plots which give considerable physical insight into the bunching process. The analysis presented here uses Dôme's[6] approach and notation The same equations are derived and discussed in Slater[7] and Chu.[8]

In the "gap-and-drift" buncher, a continuous stream of electrons passes through a gap in a resonant structure excited by a sinusoidally time-dependent electric field [see Fig. (2.1)]. For the sake of simplicity we assume that the field across the gap is constant in space and purely sinusoidal in time, i.e., no higher order harmonics contribute to the field. Then the change in energy of each electron as it traverses the gap is given by

$$\Delta\gamma m_0 c^2 = (-eE\sin\theta_0)\Delta z_{gap}$$

or

$$\Delta\gamma(\theta) = -\alpha\sin\theta_0\xi_{gap} \tag{2.1}$$

where

m_0	=	electron rest mass
e	=	electron charge
c	=	velocity of light
γ	=	total energy$/m_0c^2$ = normalized electron energy
E	=	peak electric field in resonant structure
$\theta_0 = -\omega t$	=	where ω is the resonant frequency of the structure ($t = 0$ at the field null)
Δz_{gap}	=	length of gap in resonant structure
α	=	$eE\lambda/m_0c^2$ = normalized electric field
ξ_{gap}	=	$\Delta z_{gap}/\lambda$ = normalized length of gap
λ	=	$2\pi c/\omega$ = free space wave length of the field

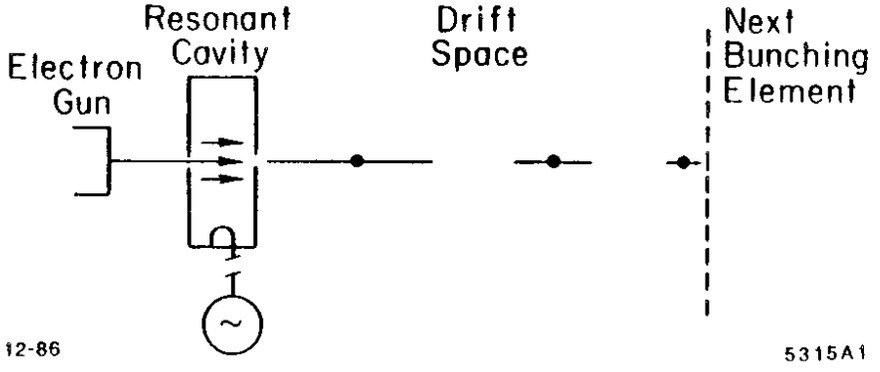

Fig. 2.1. Schematic of gap-and-drift prebuncher.

Electrons which reach the gap when $\omega t < 0$ are decelerated while electrons which arrive at the gap when $\omega t > 0$ gain energy. As the electrons traverse the drift space following the gap, they bunch around the electrons which crossed the gap at $\theta = 0$. For peak gap voltages small compared to the initial electron energy, the normalized electron momentum can be approximated as

$$p(\theta) = p_0 \left(1 - \frac{\gamma_0 \alpha}{p_0^2} \xi_{gap} \sin\theta\right) \tag{2.2}$$

where

$p = \sqrt{\gamma^2 - 1}$ = normalized momentum

γ_0, p_0 = initial normalized energy and momentum of the dc electrons.

Figure 2.2 is a plot of the longitudinal phase space in the gap-and-drift buncher. The horizontal axis is $\theta = -\omega t$ where t is the difference in time between the arrival at a given z of the reference particle, which crosses the gap at $\theta_0 = 0$, and the arrival at the same z of another electron which crosses the gap at some other θ_0. The vertical axis is γ, normalized energy of the electron. The vertical lines represent the change in energy, $\Delta\gamma(\theta)$, across the gap; an impulse function is assumed for simplicity. After the gap, electron trajectories are represented by the horizontal lines, as γ is independent of θ in the drift space. As the electrons traverse the drift space, θ changes as

$$\theta(z) = \theta_0 + \frac{2\pi z}{\lambda}\left(\frac{1}{\beta_0} - \frac{1}{\beta}\right)$$

In differential form we have

$$\frac{\Delta\theta}{\Delta z} = \frac{2\pi}{\lambda}\left(\frac{1}{\beta_0} - \frac{1}{\beta}\right)$$

or

$$\frac{\Delta\theta}{\Delta\xi} = 2\pi\left(\frac{1}{\beta_0} - \frac{1}{\beta}\right) \tag{2.3}$$

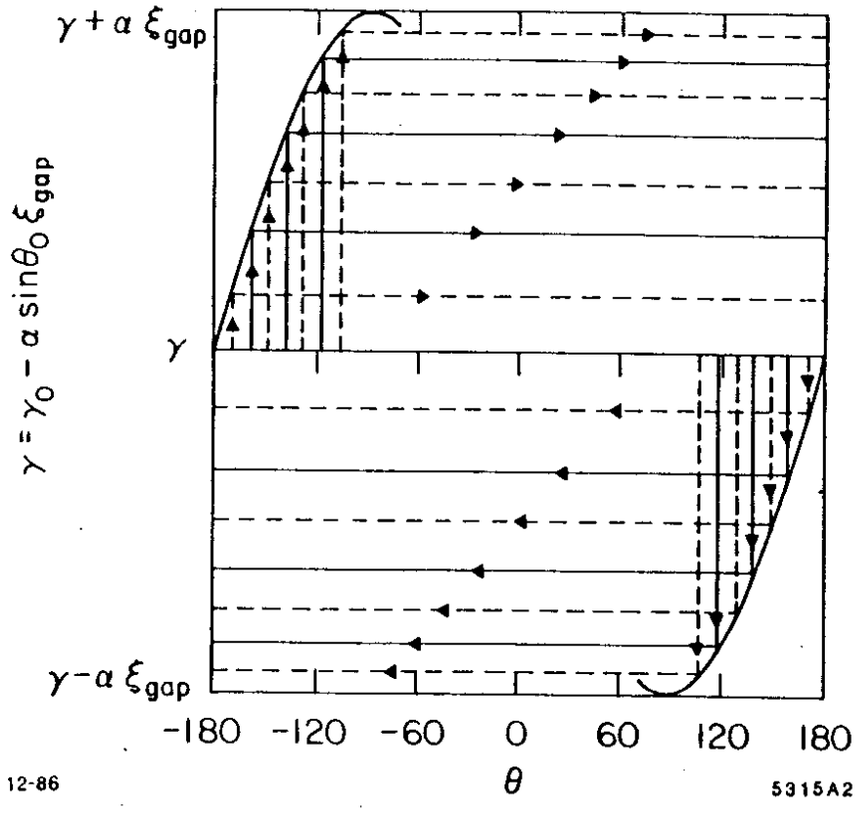

Fig. 2.2. Gap-and-drift prebuncher phase space (from Dôme[6]).

where

ξ = z/λ = normalized distance beyond the gap

$\beta = v/c$ = normalized electron velocity

β_0 = initial normalized velocity of the dc electrons.

For each particle traversing the gap-and-drift buncher, we can integrate Eq. 2.3 to find θ as a function of ξ along the drift space. In Fig. 2.3, we illustrate the bunching properties of the gap-and-drift prebuncher using an initially uniform stream of electrons with $\beta = .5$. The curve labeled $\xi = 0$ shows the phase and energy of the particles immediately following the gap with peak voltage $\alpha\,\xi_{gap} = .02$. Particles traversing the gap at $\theta_0 = -90°$ have the highest energy, while particles traversing the gap at $+90°$ have the lowest. After drifting one free space wavelength, the positions of the particles in phase space are given by the curve labeled $\xi = 1.0$. We see that the particles which traversed the gap at $\theta_0 = -90°$ now have $\theta = -45°$. After drifting 1.8 free-space wavelengths, the particles with $\theta_0 = -90°$ have overtaken the particle which traversed the gap at $\theta_0 = 0$. At $\xi = 1.8$, electrons initially occupying $\sim 240°$ of phase are bunched into $\sim 70°$ of phase.

Now let us consider the bunching properties of a traveling-wave structure. Again, assume for simplicity that the accelerating wave is a sinusoidal traveling wave with phase velocity β_w and that higher space harmonics present can be neglected. At a given z along the waveguide, electrons gain energy per unit length given by

$$\frac{d\gamma m_0 c^2}{dz} = -eE\sin\theta$$

or

$$\frac{d\gamma}{d\xi} = -\alpha\sin\theta \tag{2.4}$$

where

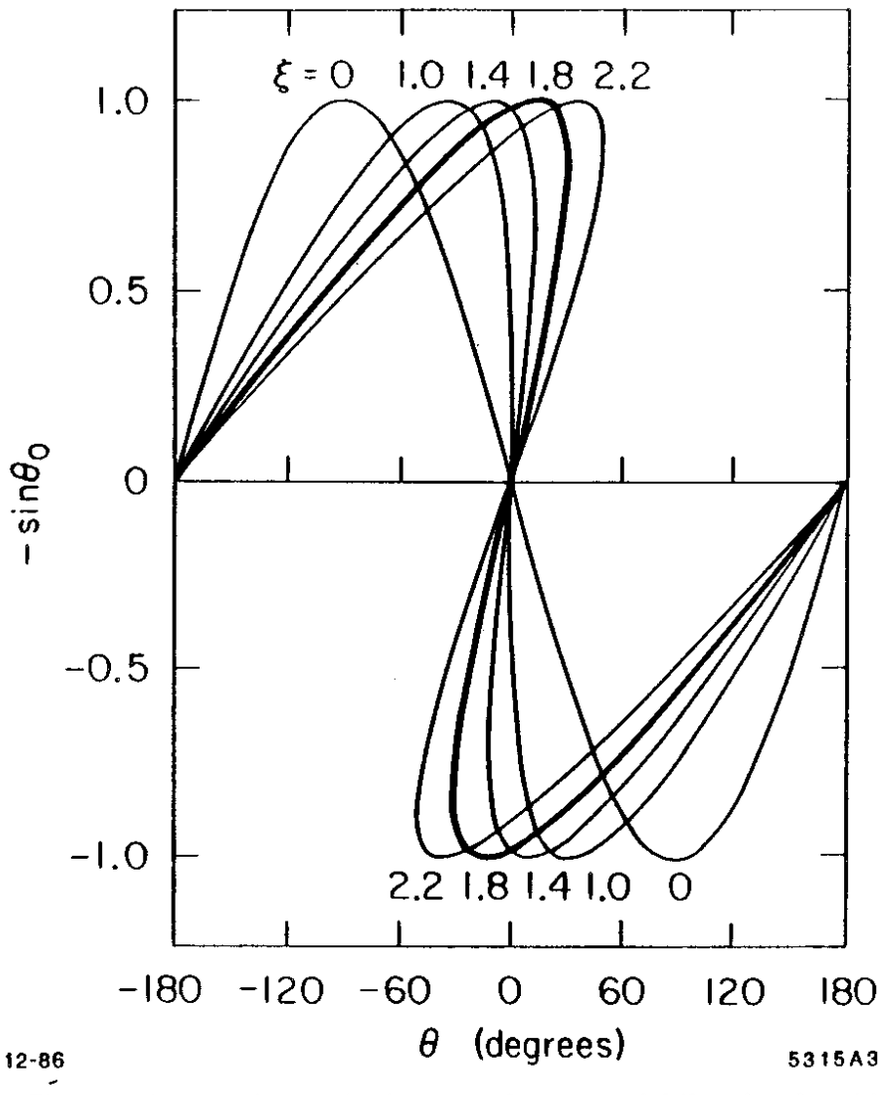

Fig. 2.3. Constant ξ curves in phase space for a gap-and-drift prebuncher with $\beta_0 = 0.5$, $\alpha\xi_{gap} = .02$. The $\xi = 0$ curve represents the phases and energies of the particles immediately downstream of the RF voltage gap. The $\xi = 1.8$ curve represents the phases of the same particles 1.8 wavelengths downstream. Considerable bunching has occurred.

θ = $-\omega t$,

t = difference in time between the arrival of the traveling wave phase null at a given z and the arrival of the electron at the same z, and

ξ = z/λ = normalized distance along the axis of the buncher.

The variation in phase per unit length of the electrons is given by

$$\frac{d\theta}{dz} = \frac{2\pi}{\lambda}\left(\frac{1}{\beta_w} - \frac{1}{\beta}\right) \quad \text{or} \quad \frac{d\theta}{d\xi} = 2\pi\left(\frac{1}{\beta_w} - \frac{1}{\beta}\right) \quad . \tag{2.5}$$

Equations (2.4) and (2.5) can be combined to yield

$$2\pi\left(\frac{1}{\beta_w} - \frac{\gamma}{\sqrt{\gamma^2 - 1}}\right) d\gamma = -\alpha \sin\theta d\theta \quad . \tag{2.6}$$

For the present discussion we have assumed that the phase velocity β_w and the field strength α are constant in the traveling-wave structure. For β_w and α constant we can integrate Eq. (2.6) to yield

$$\frac{\gamma}{\beta_w} - (\gamma^2 - 1)^{1/2} = \frac{\alpha}{2\pi}\cos\theta + H \tag{2.7}$$

where H is a constant of integration. Since we are interested in longitudinal phase space plots, it is useful to rewrite Eq. (2.7) in terms of the normalized momentum $p = \sqrt{\gamma^2 - 1} = \beta\gamma$. Equation (2.7) yields

$$\frac{(p^2 + 1)^{1/2}}{\beta_w} - p = \frac{\alpha}{2\pi}\cos\theta + H \quad . \tag{2.8}$$

To solve for the constant in Eq. (2.8) let us define a new function

$$y = \frac{(p^2 + 1)^{1/2}}{\beta_w} - p = \frac{\alpha}{2\pi}\cos\theta + H \quad . \tag{2.8a}$$

Let us also define θ_m as the value of θ when y is at its minimum. The value of p corresponding to the minimum value of y is given by

$$\frac{dy}{dp} = \frac{p}{\beta_w\sqrt{p^2+1}} - 1 = 0 \quad .$$

Substituting $p = \gamma\beta$ we have

$$\frac{\gamma\beta}{\beta_w\gamma} - 1 = 0 \quad \text{or} \quad \beta = \beta_w \quad .$$

Thus the minimum value of y occurs when $p = \gamma_w\beta_w$ where γ_w is the energy of an electron synchronous with the traveling-wave

$$y_{min} = \frac{1}{\gamma_w\beta_w} = \frac{\alpha}{2\pi}\cos\theta_m + H \quad . \tag{2.9}$$

Subtracting Eq. (2.9) from (2.8) and writing $\gamma_w\beta_w = p_w$ we have

$$\frac{(p^2+1)^{1/2}}{\beta_w} - p - \frac{1}{p_w} = \frac{\alpha}{2\pi}(\cos\theta - \cos\theta_m) \quad . \tag{2.10}$$

Equation (2.10) is plotted in Fig. 2.4 for $\beta_w < 1$. The plot shows the trajectories of electrons in longitudinal phase space. As the cosine is an even function, all orbits are symmetric about the line $\theta = 0$. Curves labeled u represent unbound orbits (i.e., electrons not captured by the wave) while curves labeled b represent bound orbits. The bound electrons follow closed paths about the point $\theta = 0$, $p = p_w$, i.e., in real space the bound electrons oscillate about the traveling-wave field null. Electrons going slower than the wave (lower right quadrant) lose energy (and velocity) until they fall behind the phase null ($\theta = 0$). They then begin to gain energy (lower left quadrant) until they are synchronous with the wave ($p = p_w$, $\theta = -\theta_m$). They continue to gain energy and velocity (upper left quadrant) until they pass the phase null ($\theta = 0$). They then lose energy (upper right quadrant) until they are slower than the synchronous velocity, and the cycle begins again. For each bound orbit, θ_m is the maximum phase excursion and occurs when $p = p_w$.

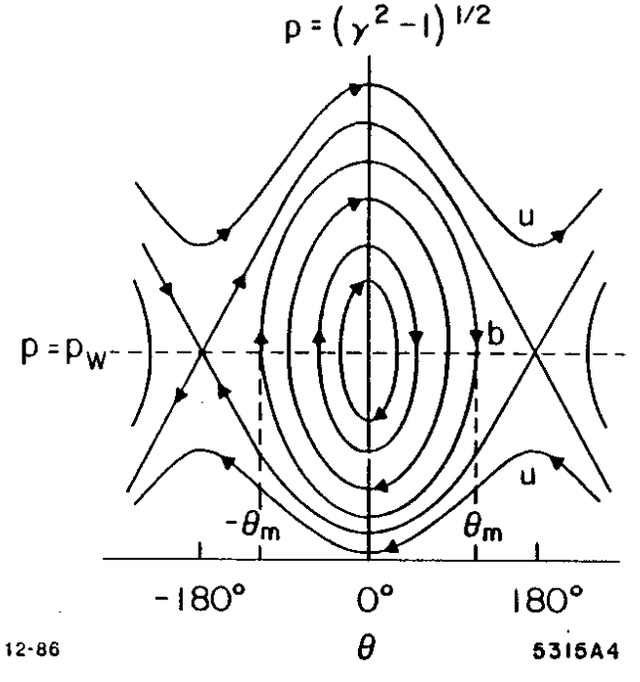

Fig. 2.4. Constant phase velocity buncher phase space for $\beta_w < 1$ (from Dôme[6]).

While Fig. 2.4 nicely illustrates the orbits of bound electrons in phase space, it gives us no insight into the rate at which various electrons execute their orbits. Dôme[6] has shown that for $\alpha \ll \pi\beta_w/2\gamma_w$ one can derive an analytic expression for θ as a function of ξ. The actual derivation is laborious but the results are informative. The dashed lines of Fig. 2.5 are the bound orbits of Fig. 2.4. Electrons leaving the gun can be represented as a monoenergetic beam evenly distributed along the z-axis. If the initial electron energy is $\gamma = \gamma_w$ at the entrance to the buncher ($\xi = 0$), the electrons will be continuously distributed along the $p = p_w$ axis of Fig. 2.5. As the electrons traverse the waveguide, they sweep out the constant ξ curves (solid lines) of Fig. 2.5. The density of electrons as a function of phase is not constant as the points at $-180°$, $0°$, and $+180°$ are fixed. Figure 2.5 nicely illustrates the bunching properties of a $\beta_w < 1$ traveling-wave buncher in the limit of low space charge and small velocity modulation ($\alpha/2\pi \ll \beta_w/\gamma_w$).

Now let us consider the motion of electrons in the presence of a traveling-wave with $\beta_w = 1$. Equation (2.10) is still valid, but the bound orbits in phase space are no longer closed curves. As electrons gain energy, they asymptotically approach the velocity of the wave and asymptotically approach θ_m. Since infinite momentum would be needed to achieve $\beta = \beta_w$, which corresponds to $\theta = \theta_m$, it is customary to write $\theta_m = \theta_\infty$ and Eq. (2.10) becomes

$$(p^2 + 1)^{1/2} - p = \frac{\alpha}{2\pi}(\cos\theta - \cos\theta_\infty) \tag{2.11}$$

or

$$\sqrt{\frac{1-\beta}{1+\beta}} = \frac{\alpha}{2\pi}(\cos\theta - \cos\theta_\infty) \quad . \tag{2.11a}$$

Equation (2.11) is plotted in Fig. 2.6. Again curves labeled u represent unbound orbits while curves labeled b are bound orbits. As in the $\beta_w < 1$ case, the curves are symmetric about $\theta = 0$. Unlike the $\beta_w < 1$ case, the electrons do not oscillate about the wave null, since it is not possible for electrons to reach

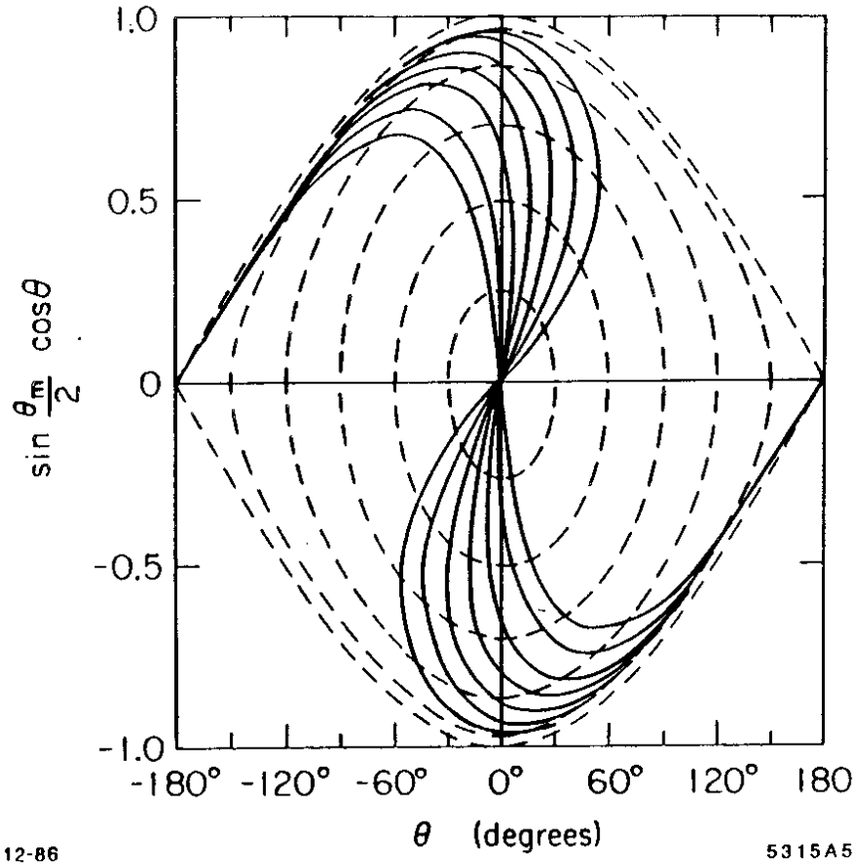

Fig. 2.5. Bunching in a traveling-wave structure. The dashed curves are the phase space orbits of the individual particles. The solid horizontal line represents a continuous monoenergetic beam at the entrance to the buncher with $\beta_0 = \beta_w$. The solid curves show the phase space occupied by the beam at seven locations on the z axis.

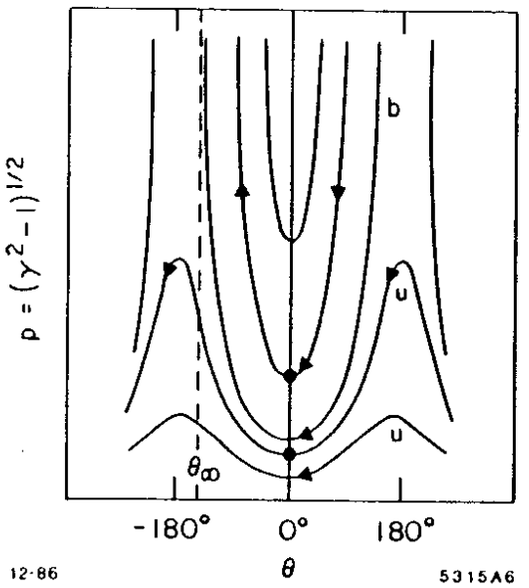

Fig. 2.6. Constant phase velocity capture region phase space ($\beta_w = 1$). Particles initially ahead of the phase null are decelerated, eventually falling behind the null where they are accelerated. Since $\beta_w = 1$, they can never achieve a velocity greater than the wave.

or exceed the speed of the wave. Instead, electrons in each orbit approach the synchronous velocity $\beta = 1$ at θ_∞ for that orbit. The electrons are said to be "captured" by the RF wave.

For $\gamma > 10$, β does not change significantly as γ increases, and bunching by velocity modulation due to the RF wave is no longer feasible. Thus the position of an electron in phase space as it enters the velocity-of-light structure determines its final phase, and therefore, its energy.

In the low space charge limit, the electron energy at the end of the accelerator is nearly proportional to $\sin\theta_\infty$.* Figure 2.7 suggests that the best spectrum is obtained if the asymptotic phases of the electrons, θ_∞, fall within a narrow range around $\theta_\infty = -90°$. To see this quantitatively, note that for electrons with the same initial momentum and entrance angles clustered near θ_0, Eq. (2.11) yields

$$-\sin\theta_\infty d\theta_\infty = -\sin\theta_0 d\theta_0$$

or

$$\Delta\theta_\infty = \frac{\sin\theta_0 \Delta\theta_0}{\sin\theta_\infty} \quad . \tag{2.12}$$

Thus the narrowest spread in final phase will occur for electrons whose entrance angles are very near zero and whose asymptotic angles are near $-90°$. For the entrance angle $\theta_0 = 0$ Eq. (2.11a) yields

$$\cos\theta_\infty^0 = 1 - \frac{2\pi}{\alpha}\sqrt{\frac{1-\beta}{1+\beta}} \tag{2.13}$$

where θ_∞^0 is the asymptotic phase of particle with $\theta_0 = 0$.

Figure 2.8 is a sketch of the phase space orbits for particles which will be captured at the extreme phases of the final bunch. Particles on the upper curve,

* This assumes, of course, that later accelerator sections are in phase with the capture region RF.

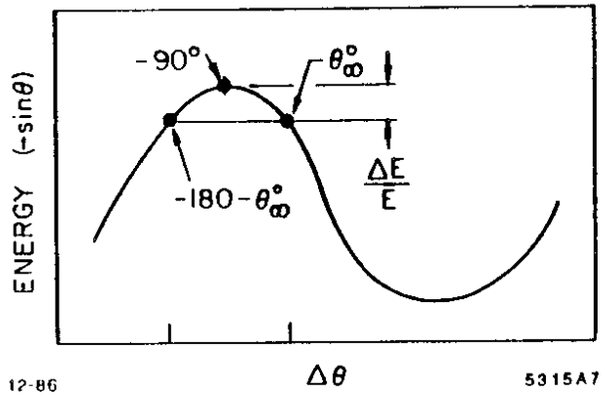

Fig. 2.7. Particle energy as a function of asymptotic phase.

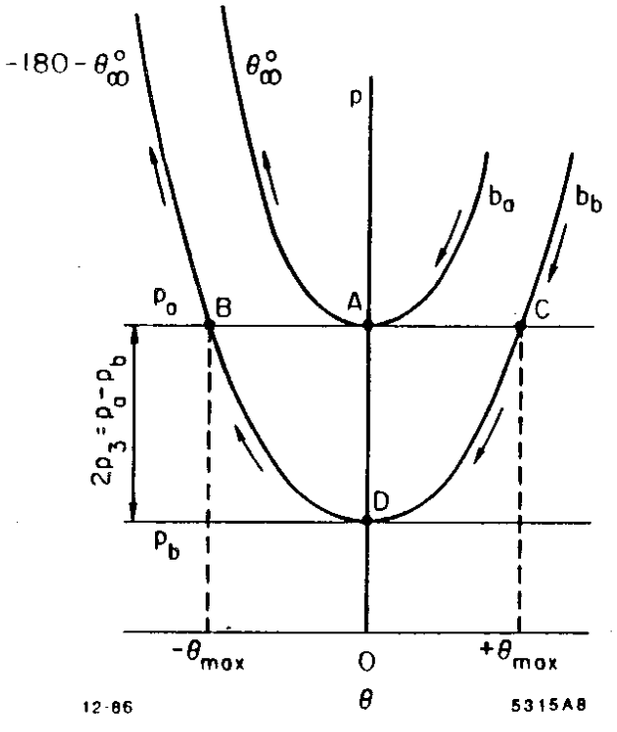

Fig. 2.8. Capture region admittance. Initial phase space which will be captured into energy spread $\Delta E/E$. $\pm\theta_{max}$ are the extreme phases of entering particles which will be captured into $\Delta E/E$ energy spread (for $p \leq p_a$).

which include the point A ($\theta_0 = 0$, $p = p_a$) have asymptotic phase θ^0_∞. Particles on the lower curve, which includes points $B(\theta_0 = -\theta_{max}, p = p_a)$ and $C(\theta_0 = \theta_{max}, p = p_a)$ have asymptotic phase $-180° - \theta^0_\infty$. Note that all electrons with the initial momentum $p = p_a$ will have asymptotic phases behind θ^0_∞. To capture the most particles within an allowed energy spread, $\Delta E/E$, θ^0_∞ should be forward of the RF crest ($-90°$) (see Fig. 2.7) and satisfy the equation

$$1 - (-\sin\theta^0_\infty) = \frac{\Delta E}{E} \quad . \tag{2.14}$$

Assuming the desired $\Delta E/E \ll 1$ (it will usually be .01 or less), Eq. (2.14) yields

$$\cos\theta^0_\infty \simeq \sqrt{2\frac{\Delta E}{E}} \quad . \tag{2.15}$$

Substituting into Eq. (2.13) we have

$$\sqrt{2\frac{\Delta E}{E}} = 1 - \frac{2\pi}{\alpha}\sqrt{\frac{1-\beta}{1+\beta}} \quad . \tag{2.16}$$

From Eq. 2.13 we see that for a given initial β, θ^0_∞ is determined solely by the value of α. Thus, to capture the most electrons within the allowed energy spread, $\Delta E/E$, we must choose α such that

$$\alpha = \frac{2\pi}{1 - \sqrt{2\frac{\Delta E}{E}}}\sqrt{\frac{1-\beta}{1+\beta}} \quad . \tag{2.17}$$

Figure 2.9 is a plot of the optimum values of α versus initial normalized electron velocity for $\Delta E/E = .01$. We see that for low initial values of β, high fields are needed in the capture region to obtain adequate bunching and spectrum.

From Fig. 2.8 we see that all electrons whose final phases are between θ^0_∞ and $-\pi - \theta^0_\infty$ will have the desired final energies. The extreme initial phase extents,

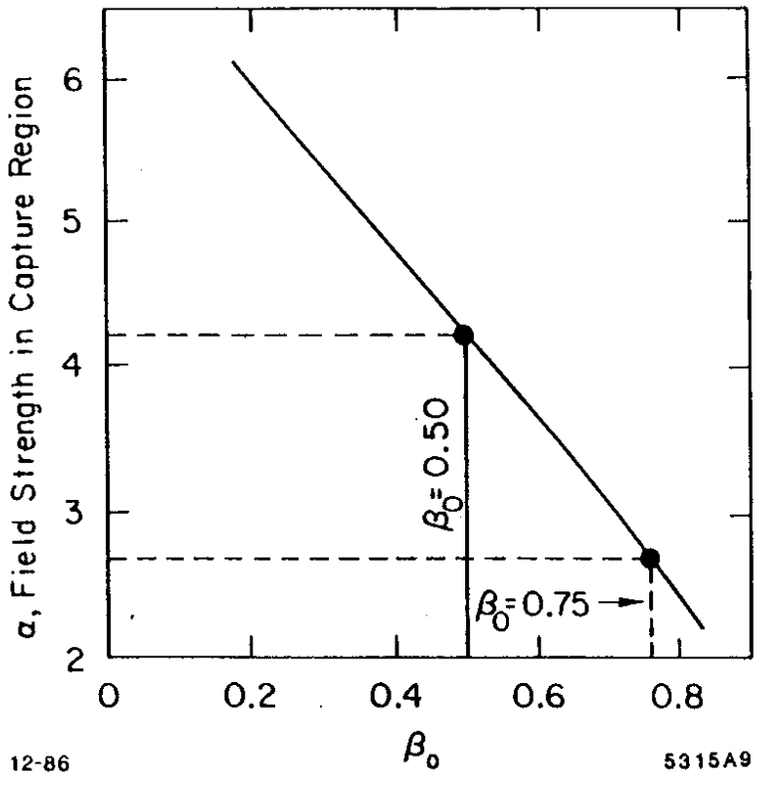

Fig. 2.9. Field strength in capture region necessary for optimum bunching of electrons with initial energy β_0 into a bunch with $\Delta E/E = 0.01$ (from Dôme[6]).

$\pm\theta_{max}$ have final phase $\theta_\infty = -\pi - \theta^0_\infty$. Using Eqs. (2.11a), (2.13) and (2.15), we find

$$\begin{aligned}\theta_{max} &= \cos^{-1}\left(1 - 2\cos\theta^0_\infty\right) \\ &= \cos^{-1}\left(1 - 2\sqrt{\frac{2\Delta E}{E}}\right)\end{aligned} \tag{2.18}$$

As the tolerance on final energy spread tightens, the acceptable phase extent of incoming electrons grows smaller.

The preceding discussion [Eqs. (2.12) through (2.18)] was limited to electrons with the same incident energy, namely those electrons with $p = p_a$, in Fig. 2.8. In general, electrons entering a velocity-of-light structure will already have undergone some velocity modulation in a gap-and-drift or $\beta_w < 1$ traveling-wave buncher. From the same figure we see that all particles whose orbits lie between b_a and b_b have asymptotic phases between θ^0_∞ and $-\pi - \theta^0_\infty$, and thus fall within the acceptable final spectrum. In particular, if we superimpose the constant ξ curves of Figs. 2.3 and 2.5 onto Fig. 2.8 [see Figs. 2.10(a) and 2.10(b)], we see that it is sometimes possible to match the longitudinal emittance of the $\beta_w < 1$ structure directly to the admittance of the $\beta_w = 1$ capture region. The best matching (i.e., the most current within the allowed energy spread) between the buncher emittance and the capture region admittance occurs when the fold-over points A and B of the ξ curves lie close to the b_b curve.

Dôme[6] has calculated that proper matching of $\beta_0 = .5$ electrons from either a drift-and-gap or a $\beta_w < 1$ traveling-wave buncher to the $\beta_w = 1$ capture region results in the capture of greater than 70% of the initially continuous stream of electrons into a spectrum of 1%.

If the desired final phase extent (and resulting energy spread) is quite small, $\Delta E/E \ll 0.01$, problems arise in matching the emittance of either buncher discussed above directly to the admittance of the capture region. From Eq. (2.18) and Fig. 2.8 we see that as the required final energy spread narrows, the admit-

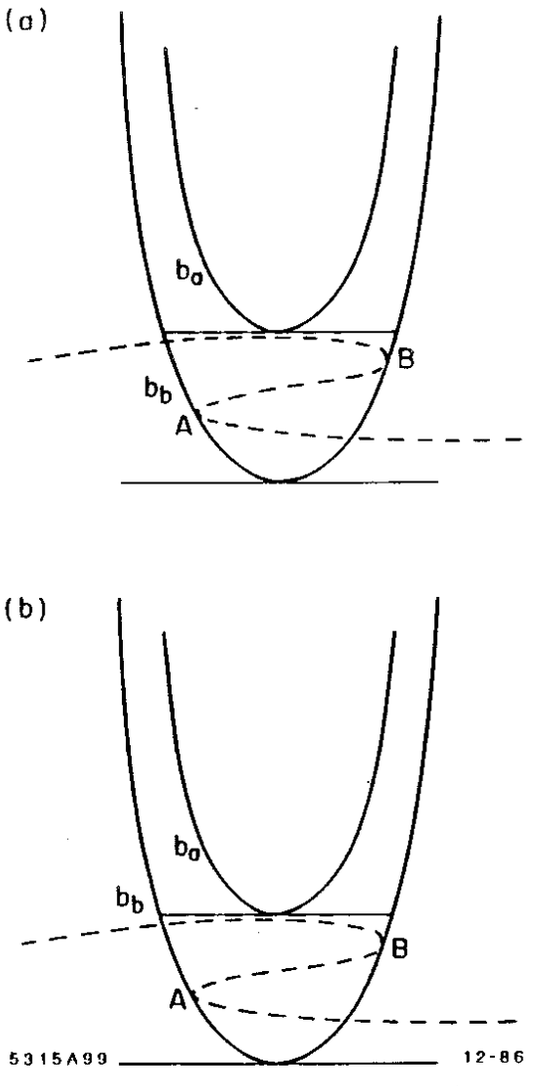

Fig. 2.10. (a) A constant ξ curve of Fig. 2.3 (the gap-and-drift buncher) superimposed on the phase space orbits of the $\beta_w = 1$ capture region. (b) A constant ξ curve of Fig. 2.5 (the $\beta_w < 1$ traveling-wave buncher) superimposed on the phase space orbits of the $\beta_w = 1$ capture region.

tance of the capture region grows smaller in both phase and momentum extent; as θ_{max} decreases, $p_a - p_b$ also decreases.

It is clear from Figs. 2.3 and 2.5 that bunching of a dc beam due to a sinusoidal field is inherently nonlinear. It is not possible to make the resulting bunch arbitrarily short while retaining significant current. As the acceptable final phase extent of the beam shrinks, less and less current from the buncher fits into the capture region admittance.

In order to have a narrow spectrum without unduly low currents, we can capture more electrons into the final phase extent if we use an intermediate bunching element to match the emittance of the prebuncher to the admittance of the capture region. Lichtenberg[9] suggested the use of impedance matching concepts for matching beam emittances to machine admittances in longitudinal phase space. He defined the "impedance" as the ratio of the momentum extent of the bunch to its phase extent in longitudinal phase space. This concept led Miller[5] to the idea of matching the emittance of the prebuncher to the admittance of the accelerator with a $\beta_w < 1$ traveling-wave buncher used as a quarter-wave transformer. Figure. 2.11 illustrates the principle of the quarter-wave transformer. In general, the prebuncher emittance has a relatively large phase extent and small momentum extent. The capture region admittance has smaller phase extent and larger momentum extent. We choose the phase velocity β_w of the buncher such that $\beta_0 < \beta_w < 1$. Electrons from the prebuncher with mean momentum p_0 are injected at the phase null. After a quarter of a cycle in phase space, the buncher has transformed the initially large phase extent (small momentum extent) into a smaller phase extent (and larger momentum extent). The electrons have also gained energy.

To find the optimum characteristics of the quarter-wave transformer, it is useful to circumscribe the final prebuncher emittance with the ellipse at the bottom of Fig. 2.11. The ellipse has principal axes $\theta_1 = (c - d)/2$ and $p_1 = (a - b)/2$ and area $\pi\theta_1 p_1$. Given that the initial phase extent θ_1 is appreciably

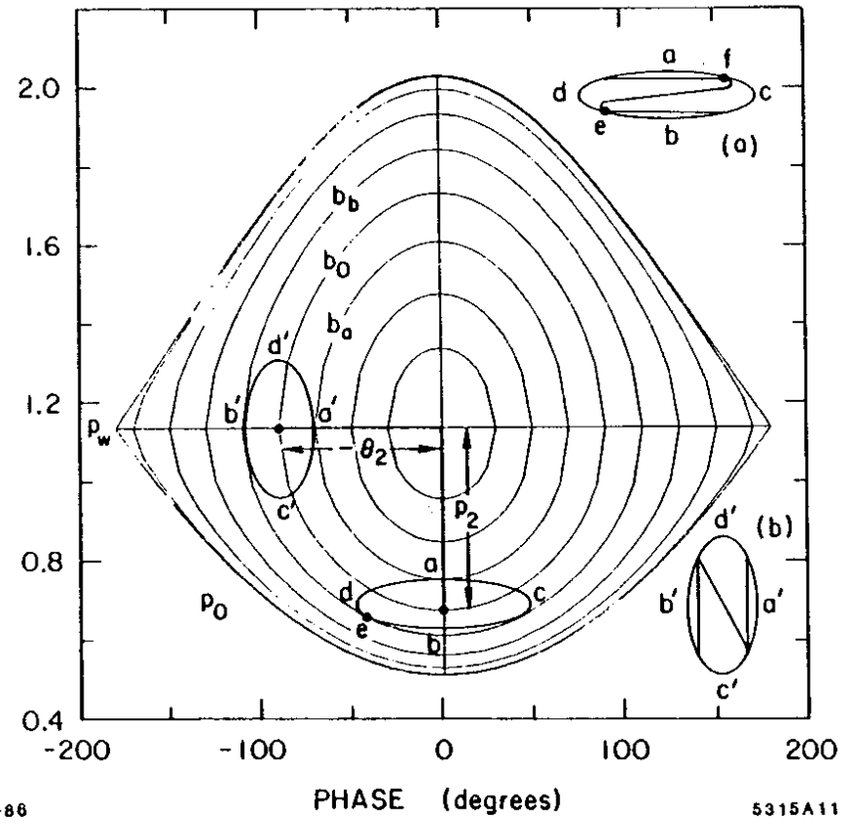

Fig. 2.11. Beam emittance at the end of the prebuncher mapped into the beam emittance at the entrance to the catpure region is accomplished by a quarter-wave transformation in a $\beta_w < 1$ traveling-wave structure. (a) Beam emittance at the entrance to the buncher circumscribed by ellipse a, c, b, d. (b) Beam emittance at the end of the buncher circumscribed by ellipse a', c', b', d'.

smaller than 180° and that $p_1 \ll p_w - p_0$, we can assume that the mapping of the prebuncher emittance ellipse from one region of phase space to another does not distort the ellipse appreciably. As the ellipse moves through one-quarter of a cycle in the buncher, phase space points a, b, c, and d are mapped to points a', b', c', d'. All points within the prebuncher ellipse (Fig. 2.11a) are mapped into the capture region ellipse (2.11b), with principal axes $\theta_3 = (a' - b')/2$ and $p_3 = (d' - c')/2$. Note from Fig. 2.11 that the beam ellipse rotates about the particle initially at the point $(0, p_0)$ which moves in orbit b_0 to the point $(-\theta_2, p_w)$ a quarter-cycle later. Assuming phase space orbits b_0, b_a and b_b are similar curves,

$$\frac{p_w - a}{|\, a' \,|} = \frac{p_w - b}{|\, b' \,|} = \frac{p_w - p_0}{|\, -\theta_2 \,|} \quad .$$

Defining $p_2 = p_w - p_0$ and rearranging, we have

$$a - b = \frac{p_2}{|\, -\theta_2 \,|} \left(|\, b' \,| - |\, a' \,| \right)$$

or

$$p_1 = \frac{p_2}{\theta_2} \theta_3 \quad . \tag{2.19}$$

Similarly, we find

$$\frac{d' - c'}{p_2} = \frac{c - d}{\theta_2}$$

or

$$p_3 = \frac{p_2}{\theta_2} \theta_1 \quad . \tag{2.20}$$

From Eqs. (2.19) and (2.20) the conditions for mapping the prebuncher emittance to the capture region admittance are

$$p_3 \theta_3 = p_1 \theta_1 \tag{2.21}$$

and

$$\frac{p_2}{\theta_2} = \sqrt{\frac{p_1}{\theta_1} \frac{p_3}{\theta_3}} \quad . \tag{2.22}$$

From Eq. (2.21) we see that the areas of the prebuncher and capture region ellipses must be equal. Any decrease in the phase extent of the beam results in momentum spread growth by the same factor. From Eq. (2.22) we see that the buncher orbit ellipticity p_2/θ_2 must be the geometric mean of p_1/θ_1 and p_3/θ_3 to match the prebuncher emittance to the capture region admittance, as would be expected by the analogy with transmission line matching.

2.1.2 Design of the SLAC Main Injector

To illustrate the previous discussion let us examine the design of SLAC's low current injector[4,5] (see Fig. 2.12). A continuous stream of electrons from the gun are bunched in a gap-and-drift prebuncher. The beam from the prebuncher is injected into a $\beta_w = .75$ traveling-wave buncher used as a quarter-wave transformer. Electrons then enter a standard SLAC accelerator section, the first 30 cm of which acts as the capture region.

The SLAC injector was designed with an electron gun voltage of 80 kV. At this voltage the gun could be housed in a reasonably small space without oil or high dielectric strength gas needed as an insulator, allowing easy access for troubleshooting and repair. As is evident from Fig. 2.9, the capture of electrons with mean energy of 80 kV (and mean velocity $\beta_0 = .5$) requires electric fields in the capture region of 210 kV/cm. Supplying such fields to a SLAC three-meter accelerator section would require more power than an early SLAC klystron could produce. Therefore, the buncher was designed with $\beta_0 < \beta_w < 1$ to accelerate the beam while matching the phase space ellipse from prebuncher to capture region. Early SLAC klystrons could comfortably produce fields of 130 kV/cm in a SLAC accelerator section which corresponds to $\alpha = 2.7$ in the capture region. From Fig. 2.9 we see that the best capture will occur if electrons enter the capture region with mean velocity $\beta = .75$. The traveling-wave buncher was consequently designed with this phase velocity.

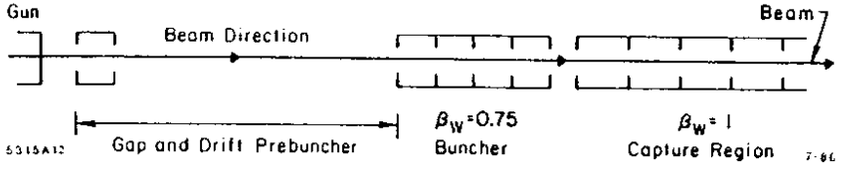

Fig. 2.12. The SLAC low-current, long-pulse injector.

The field strength in the buncher was chosen to match the prebuncher emittance to the capture region admittance. The capture region admittance was determined by the desired final phase (which determines final spectrum). For a desired final bunch length of 4° (which would yield better than 0.1% energy spread in the absence of gun voltage or klystron phase jitter), Eq. (2.18) yields

$$\theta_{max} = \theta_3 = \cos^{-1}(1 - 2\cos 88°) = 21.5° \quad . \tag{2.23}$$

As shown by Dôme[6] (see Fig. 2.3, bold constant $\xi = 1.8$ curve), a gap-and-drift prebuncher can bunch approximately 70% of a dc beam into 75°. Thus the buncher must compress the phase extent by a factor of 1.7. The admittance of the capture region is illustrated in Fig. 2.8. All particles which lie in orbits between b_a and b_b will lie within the allowed energy spectrum at the end of the accelerator section. As a practical matter, the most useful region of this admittance is the cup-shaped region bounded by the line $p = p_a$ on top and the curve b_b on the bottom. We can calculate the maximum momentum acceptance of this region, $2p_3 = p_a - p_b$. For the point $(0, p_a)$, Eq. 2.11 yields

$$y_a = \left(p_a^2 + 1\right)^{1/2} - p_a = \frac{\alpha}{2\pi}\left(1 - \cos\theta_\infty^0\right) \tag{2.24a}$$

where we have reintroduced the function $y = (p_a^2 + 1)^{1/2} - p_a$ from Eq. 2.8a. Solving for p_a we have

$$p_a = \frac{1 - y_a^2}{2y_a} \tag{2.24b}$$

For the point $(0, p_b)$, Eq. 2.11 yields

$$y_b = \left(p_b^2 + 1\right)^{1/2} - p_b = \frac{\alpha}{2\pi}\left[1 - \cos(-\theta_\infty^0)\right] \quad . \tag{2.24c}$$

Again, solving for p_b yields

$$p_b = \frac{1 - y_b^2}{2y_b} \quad . \tag{2.24d}$$

For $\theta_\infty^0 = -88°$ and $\alpha = 2.7$

$$2p_3 = p_a - p_b = 0.10 \quad . \tag{2.25}$$

From Eq. (2.21) we know that a factor of 1.7 compression of phase extent will result in a factor of 1.7 increase in momentum extent. Thus the prebuncher momentum extent $2p_1$ should be no more than 0.06. This requires a prebuncher gap voltage of no more than 7.8 kV. To achieve a 75° bunch, the drift space following the gap at 8 kV should be 36 cm.

At this point, only α in the buncher is undetermined. From Eq. (2.10), we can find the final phases of the particles which enter the buncher at a and e of Fig. 2.11, as these particles move to the buncher emittance phase extrema, θ_m and $\theta_m - 2\theta_3$. Specifically, Eq. (2.10) yields for the particle initially at a with momentum p_a

$$\frac{2\pi y_a}{\alpha} = \frac{2\pi}{\alpha}\left(\frac{\sqrt{p_a^2+1}}{\beta_w} - p_a - \frac{1}{p_w}\right) = 1 - \cos(\theta_m - 2\theta_3) \tag{2.26}$$

and for the particle at e with initial phase θ_e and momentum p_e

$$\frac{2\pi y_e}{\alpha} = \frac{2\pi}{\alpha}\left(\frac{\sqrt{p_e^2+1}}{\beta_w} - p_e - \frac{1}{p_w}\right) = \cos\theta_e - \cos\theta_m \quad . \tag{2.27}$$

Solving for α we find

$$y_a(\cos\theta_e - \cos\theta_m) - y_e\Big[1 - \cos(\theta_m - 2\theta_3)\Big] = 0 \tag{2.28}$$

Equation (2.28) can be solved numerically. For $\theta_1 = 37.5°$, $\theta_3 = 21.5°$ $p_a = .61$ and $p_e = .55$ we find $\pm\theta_m = \pm 148.7$. Substituting into (2.27) we find $\alpha = .33$ which corresponds to a field strength of 16 kV/cm.

The final parameters for a low current injector are summarized in Table 2.1.

Table 2.1. Main injector preliminary design specifications.

Element	kV/cm	Length (cm)	β_w	$\Delta\theta$	Δp	$\Delta E/E$
Gun	—	—	0.5	270°	0	
Gap-and-drift prebuncher	8	36*	—	75°	.06	
Quarter-wave transformer buncher	16	10.5	.75	43°	.10	
Capture region	130	21.0	1.0	4°	—	
End of accelerator section	—	—	—	—	—	0.1%

*Including drift.

The specifications derived here depend on the assumptions of small energy modulations and undistorted mapping in the buncher region. Since we have calculated a bunch of 75° entering the buncher and 43° leaving it, we expect some distortion in the mapping as electrons in outer orbits "lag behind" those in inner orbits.

The final design values for the field strengths, drift length and phase shifts between elements were determined by computer modeling of the injector outlined in Table 2.1. Equations (2.4) and (2.5) were numerically integrated to determine electron orbits in the bunching system. The theoretical performance of the "Table 2.1" injector is summarized in the phase space plots of Fig. 2.13 and 2.14. The numerical results are in excellent agreement with the analytic results.

Figure 2.13(a) shows the beam emittance at the end of the prebuncher drift space. The energy spread introduced by the prebuncher is 20% of the initial energy of the beam and thus the bunching is slightly asymmetric about the center particle (i.e., the particle which passed through the gap at the phase null). The decelerated electrons are further behind the center than the accelerated particles are ahead. From Fig. 2.11 we see that, if anything, we should enter the buncher slightly forward of the phase null, as the electron density is highest at points e and f, and we wish these electrons to fall between orbits b_a and b_b. Hence the

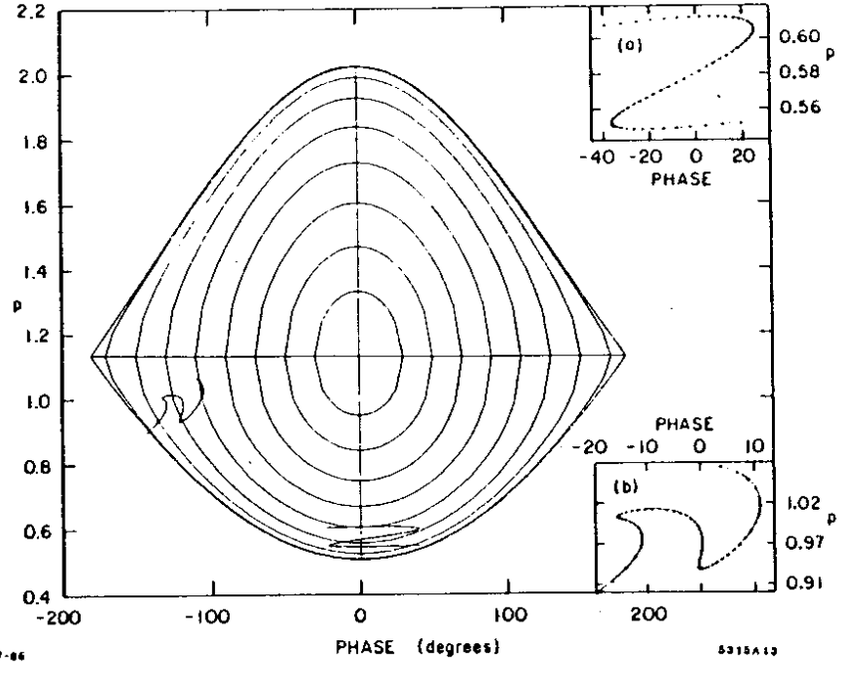

Fig. 2.13. Simulation of particle orbits through the $\beta_w = .75$ traveling-wave buncher in SLAC's low-current injector.

theoretical performance is improved by introducing a phase shift of 15° between the prebuncher and buncher (see Fig. 2.13).

Figure 2.13(b) is a plot of the beam emittance at the output of the buncher. The mapping from prebuncher output to capture region input is reasonably undistorted. The area is also conserved, as $\Delta p \, \Delta\theta = .43$ for both ellipses. Note that the beam enters the buncher as three straight-line segments in a region of curved orbits and emerges as three curved segments in a region of straight orbits.

The beam enters the capture region with 28° of phase extent and a momentum extent of .156. The numerical results predict that the injector described in Table 2.1 will successfully capture 67% of the dc electrons from the gun into 4° of RF phase (Fig. 2.14).

SLAC's main injector has specifications very similar to those in Table 2.1, although the design calls for slightly higher prebuncher and buncher voltages. Figure 2.15 shows two longitudinal beam profile measurements at the end of the injector three-meter-long accelerator section. In curve A, 70% of the gun current is captured into 4° of S-band phase. Experience with the SLAC injector has shown that the discrete, constant-phase velocity element bunching technique described here is indeed robust. Good bunching has been achieved with gun voltages ranging from 50 to 90 kV by proper optimizing of other parameters.[5]

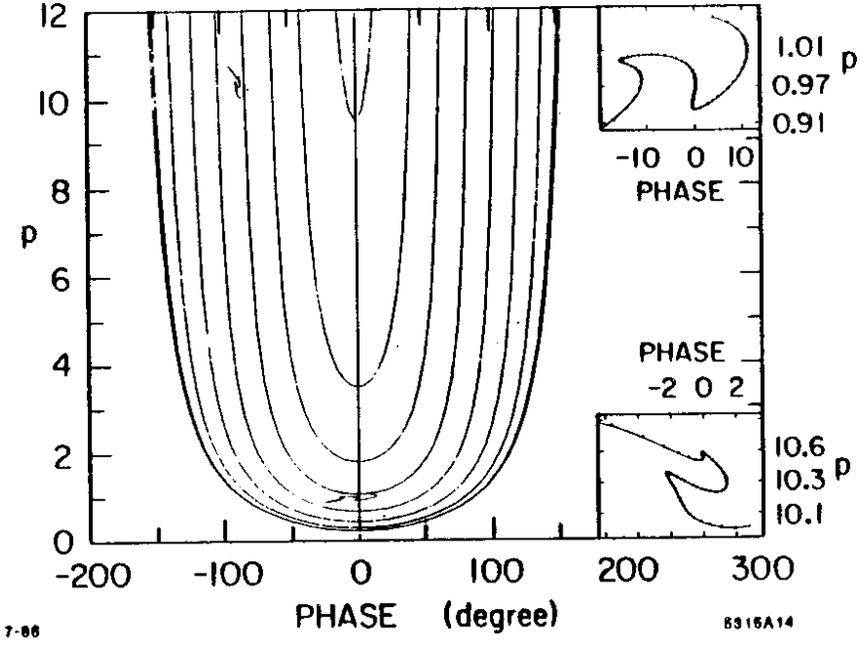

Fig. 2.14. Simulation of particle orbits through the $\beta_w = 1$ capture region in SLAC's low-current injector.

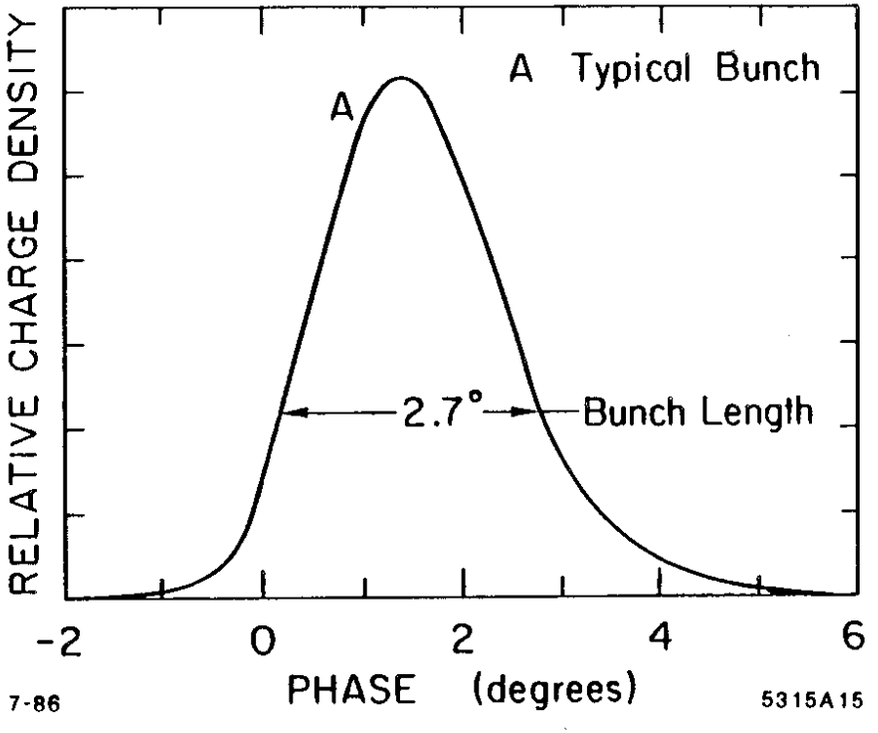

Fig. 2.15. Experimental charge distribution in main injector (from Miller[6]).

2.2 COLLIDER INJECTOR DESIGN

As discussed in the introductory chapter, the collider injector must capture 5 to 7.5 $\times$ 10^{10} electrons on a single RF crest. Averaged over one cycle of RF, this is an accelerated current of 23 to 34 amps, considerably higher than any S-band linear accelerator had operated before, and two orders of magnitude higher than the current shown in Fig. 2.15. In addition, the 1.21 GeV bunch entering the damping ring must have an energy spread no greater than $\pm 1\%$. As we will discuss in greater detail in Section 3.2, this can be accomplished if the final bunch length is of the order of 20° FWHM at S-band.

Bunching and capturing 5×10^{10} electrons in 20° of S-band phase presents two serious complications to the design strategy used in SLAC's main injector. First, SLAC's main injector was designed to bunch and capture a large fraction of the dc gun current onto a series of adjacent RF crests, forming pulses as short as three bunches or as long as 5×10^3 bunches. For reasons we shall explain below, our goal is now different: rather than forming small bunches at 360° intervals and capturing them onto adjacent RF crests, we must now bunch and capture electrons spread over approximately 3500° of S-band onto one RF crest. The second complication to the previous design strategy is that at such high charge densities, space charge forces are no longer negligible.

These complications compromise a number of assumptions that were valid in the low current, multi-bunch pulse case, in particular

- Due to the large phase extent of the initial electrons, we shall see that the beam occupies a large area of phase space in the buncher and we cannot expect mappings from one region to another to be distortion free.
- Due to space charge, particles no longer follow the phase space orbits described in Section 2.1; only the center of mass of the bunch follows these orbits.

Although some very useful assumptions of the last section have less validity here, we begin by considering the design of the CID injector as a perturbation

on the design of the main injector. The same design strategy is employed and outlined below:

1. Use a gap-and-drift prebuncher to accomplish initial bunching.
2. Use a $\beta_w < 1$ buncher as a quarter-wave transformer to match the prebuncher emittance to the capture region admittance.
3. Use a $\beta_w = 1$, high α accelerator section to accomplish final bunching and capture.

The CID injector was initially designed and constructed in a period of 18 months. The analysis presented here is the product of our original design strategy combined with ideas accumulated from working with the actual injector. This section is divided into three parts. In Section 2.2.1 we discuss longitudinal beam dynamics in the low current, large signal limit. This analysis was completed after CID was constructed, and incorporates ideas developed from operational experience. In Section 2.2.2 we present a *Gedanken* injector design which incorporates the analysis of Section 2.2.1. This design is more comprehensive (and more successful, in theory) than our actual CID design. For completeness, in Section 2.2.3 we present our original CID design.

It is instructive to describe the high current design as a two-step process. First, in Section 2.2.1 we examine the problem of bunching and capturing a beam with an initially large phase extent in the absence of space charge. Next, in Section 2.2.2 we "turn on" the space charge forces and adjust our design to accommodate them.

2.2.1 Longitudinal Dynamics in the Low Current, Large Signal Limit

As stated earlier, the CID injector must bunch and capture electrons with an initial phase extent of $\sim$ 3500° of S-band. This is due to the fact that our state-of-the-art pulser electronics for thermionic cathodes could produce no more

than 12 amps of peak current. At this current one would need a gun pulse of 1 ns FWHM (or $\sim 1000°$ at S-band) to produce 7.5×10^{10} electrons. In practice we have found that the gun cannot produce such short pulses at 12 amps, but can yield a Gaussian pulse of 6-8 amps, 2 ns FWHM. To capture electrons out to $\pm 2\sigma$ (or 95% of the charge in the gun pulse) we must capture electrons whose initial phase extent is $\sim 3500°$ or 10 cycles at S-band.

The gap-and-drift buncher must compress this very long bunch by a factor of ten just to get all the electrons into one S-band cycle. As we bunch it with a gap-and-drift prebuncher, space charge forces eventually oppose bunching, leading to a large phase extent at the entrance of the buncher. Therefore we begin our design by optimizing the phase acceptance of the combined buncher/capture region acceptance.

There are five parameters over which we have control to accomplish this optimization, specifically, the phase at which the bunch enters the buncher, the phase velocity of the buncher, β_w, the field strength in the buncher, α_2, the phase at which the bunch enters the capture region, and the field strength in the capture region, α_3.

In the following pages, we calculate the required values of these parameters necessary to map a given emittance at the entrance to the buncher into 16° of phase at the end of the capture region. A bunch of 16° of phase extent captured in the RF crest yields an energy spread of 1%. The logical flow of determining optimum values for the five control parameters is somewhat obscured by the specific calculation. We therefore list all relevant parameters in Table 2.2 with a short explanation of their source. The quantitative details follow in Table 2.3.

Examination of Table 2.2 shows that given $\Delta E/E$, p_0 and the condition for optimum bunching in the buncher and capture regions (Eq. 2.12), all other parameters are fixed or determined by our choice of β_w. Therefore, β_w is the first column of Table 2.3 and we shall discuss the buncher acceptances generated by various choices of β_w.

Table 2.2. Functional Dependence of Injector Parameters.

Parameter	How Determined
$\Delta E/E$, Energy spread	Given
p_0, Mean momentum of electrons entering buncher	Given
$2\theta_3$, Phase acceptance of capture region	Function of $\Delta E/E$ (Eq. 2.30b)
Optimum phase of bunch at entrance to the buncher = 0°	Condition for optimum bunching (Eq. 2.12)
θ_2, Optimum phase of bunch at exit of the buncher = −90°	Condition for optimum bunching (Eq. 2.12)
$p_2 = p_0 - p_w$	Function of p_0 and β_w
α_2, Field strength in the buncher	Function of p_0 and β_w (Eq. 2.29)
Optimum phase of bunch at entrance to capture region = 0°	Condition for optimum bunching (Eq. 2.12)
Optimum phase of bunch at entrance to capture region = −90°	Condition for optimum bunching (Eq. 2.12)
α_3, Field strength in capture region	Function of β_w (Eq. 2.30a)
$2p_3$, Momentum acceptance of capture region	Function of $\Delta E/E$ and α_3 (Eqs. 2.34a or b)
$2p_1$, Momentum acceptance of buncher	Function of $\theta_3 p_2/\theta_2$ (Eq. 2.19)
$2\theta_1$, Phase acceptance of buncher	Function of $p_3 \theta_2/p_2$ (Eq. 2.20)

We begin our quantitative discussion of the conclusions in the Table 2.2 by considering the combined buncher/capture region phase space shown in Fig. 2.16. The emittance of the beam as it leaves the gap-and-drift prebuncher is circumscribed by the ellipse a, c, b, and d. Having traversed a quarter of a cycle in

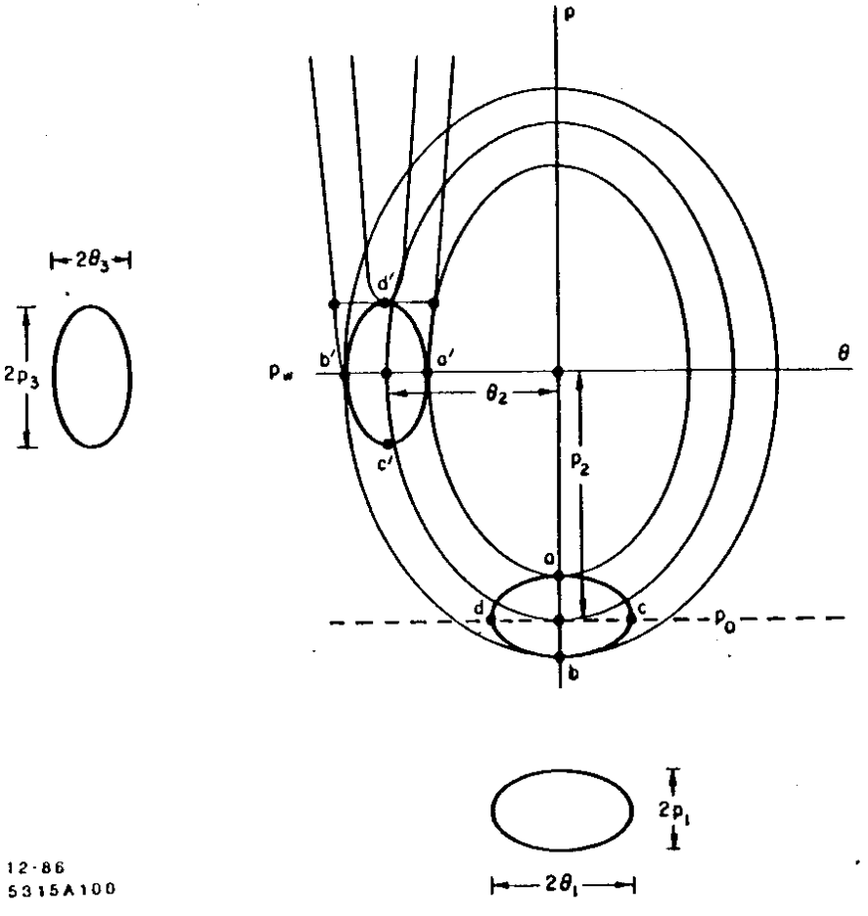

Fig. 2.16. Combined buncher region and capture region phase space.

the buncher phase space, the beam emittance is circumscribed by the new ellipse a', c', b', d'. This ellipse must be contained within the capture region acceptance which yields a 1% energy spectrum at the end of the accelerator section.

The phase spread of the bunch at the output of the buncher is approximately $\theta_m(a') - \theta_m(b') = \Delta\theta_m$. For electrons with the same initial momentum, p_0 (i.e., those on line segment c-d), Eq. (2.12) is also valid for $\beta_w < 1$ traveling wave structures, i.e.,

$$\Delta\theta_m = \frac{\sin\theta\,\Delta\theta}{\sin\theta_m} \quad . \tag{2.12}$$

The spread in phase at the output of the buncher is minimized if the entrance angles are near 0° and the exit angles are near −90°. Assume that the center of the bunch enters the buncher at 0° of phase and with momentum p_0. We can quantify this optimization condition by choosing the field strength and phase velocity of the buncher so that the electron which enters the buncher at (0, p_0) exits the buncher at (−90°, p_w). Equation (2.10) yields

$$\frac{(p_0^2+1)^{1/2}}{\beta_w} - p_0 - \frac{1}{p_w} = \frac{\alpha_2}{2\pi} \tag{2.29}$$

where

p_0 = normalized momentum of the center electron after it has traversed the prebuncher gap

p_w = $\beta_w\gamma_w$, where β_w is the phase velocity of the buncher

α_2 = normalized electric field strength in the buncher.

Equation (2.12) also applies to the capture region; optimum bunching is accomplished when the bunch has initial phases near 0° and asymptotic phases near 90°. We can also quantify this condition by requiring that the particle which leaves the buncher with phase equal to 90° and momentum equal to p_w enters the capture region at 0° of phase and achieves an asymptotic phase of −90°.

Equation (2.11) gives

$$\left[p_w^2+1\right]^{1/2}-p_w=\frac{\alpha_3}{2\pi} \quad . \tag{2.30a}$$

Note that the field strength in the capture region depends only on the phase velocity of the buncher.

We can now calculate the phase and momentum acceptances of the capture region. To find the phase acceptance, note that points a' and b' of Fig. 2.16 transform to an asymptotic phase of $-180°-\theta_\infty^\circ$. From Eqs. (2.11) and (2.30a) we have

$$\theta_3=\arccos[1-\cos\theta_\infty^\circ] \quad . \tag{2.30b}$$

To find the momentum acceptance note that point d' of Fig. 2.16 transforms to θ_∞° and point c' transforms to $-180°-\theta_\infty^\circ$. From Eqs. (2.11) and (2.24) we have

$$y=\sqrt{p^2+1}-p=\frac{\alpha}{2\pi}\left(\cos\theta_0-\cos\theta_\infty^\circ\right) \quad . \tag{2.31}$$

For point d', transformed to θ_∞^0

$$y_{d'}=\frac{\alpha_3}{2\pi}\left(1-\cos\theta_\infty^0\right) \quad p_{d'}=\frac{1-y_{d'}^2}{2y_{d'}} \quad . \tag{2.32a}$$

For point c', transformed to $-180°-\theta_\infty^0$

$$y_{c'}=\frac{\alpha_3}{2\pi}\left(1+\cos\theta_\infty^0\right) \quad p_{c'}=\frac{1-y_{c'}^2}{2y_{c'}} \quad . \tag{2.32b}$$

The momentum acceptance of the capture region, $2p_3$, is given by combining Eqs. (2.32a) and (2.32b)

$$2p_3=p_{d'}-p_{c'}=\frac{1-y_{d'}^2}{2y_{d'}}-\frac{1-y_{c'}^2}{2y_{c'}} \quad . \tag{2.33}$$

After some algebra we find

$$2p_3=p_{d'}-p_{c'}=\frac{1+(\alpha_3/2\pi)^2\sin^2\theta_\infty^0}{(\alpha_3/2\pi)\tan\theta_\infty^0\sin\theta_\infty^0} \quad . \tag{2.34a}$$

We can simplify this expression for the case where the center of the bunch is asymptotically approaching $-90°$. Using the approximations

$$\sin\theta_\infty^0\approx-1$$

$$\cos\theta_\infty^0\approx\theta_\infty^0+\frac{\pi}{2}\equiv\Delta\theta_\infty$$

we find a simple relationship between the asymptotic bunch length and the momentum acceptance of the capture region:

$$p_3=\left(\frac{2\pi}{\alpha_3}+\frac{\alpha_3}{2\pi}\right)\frac{\Delta\theta_\infty}{2} \quad . \tag{2.34b}$$

From Eqs. (2.34) (see Fig. 2.17) we find that p_3 goes to infinity for $\alpha_3=0$ and $\alpha=\infty$, and passes through a broad minimum near $\alpha=2\pi$. To increase p_3, we should move away from $\alpha=2\pi$ in either direction. $\alpha=2\pi$ corresponds to a field strength of $K=300$ kV/cm or 30 MeV/m. SLAC's 30 MW klystrons (available at the time CID was built) can provide a maximum field strength of 17 MeV/meter, or $\alpha=3.5$, thus we have the ability to vary α in the range from 0 to 3.5. The acceptance of the capture region phase space is plotted in Fig. 2.18 for six different values of α from 2 to 4. The phase acceptance remains constant (Eq. 2.30b), while the momentum acceptance increases for decreasing α. Of course, as α gets small, the initial momentum for capture increases (see Fig. 2.9) and the distance needed to capture increases.

From Eqs. (2.30) and (2.34) we see that the momentum acceptance of the capture region depends on the phase velocity, β_w, of the buncher region. As β_w and p_w increase, the momentum acceptance of the capture region increases.

We now examine how the buncher acceptance is affected by choice of phase velocity. To begin, let us assume that the transformation of the phase space ellipse of the beam in the buncher is relatively undistorted (we refer to this in Table 2.3 as the "linear approximation"). Consider again Eqs. (2.19) and (2.20).

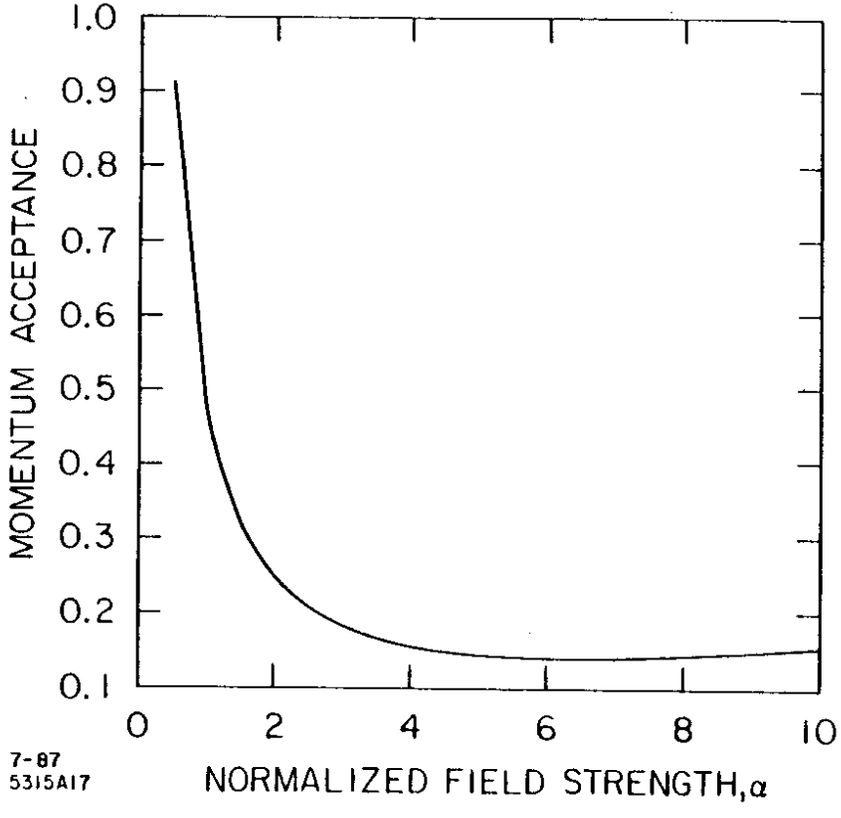

Fig. 2.17. Capture region momentum acceptance as a function of normalized field strength.

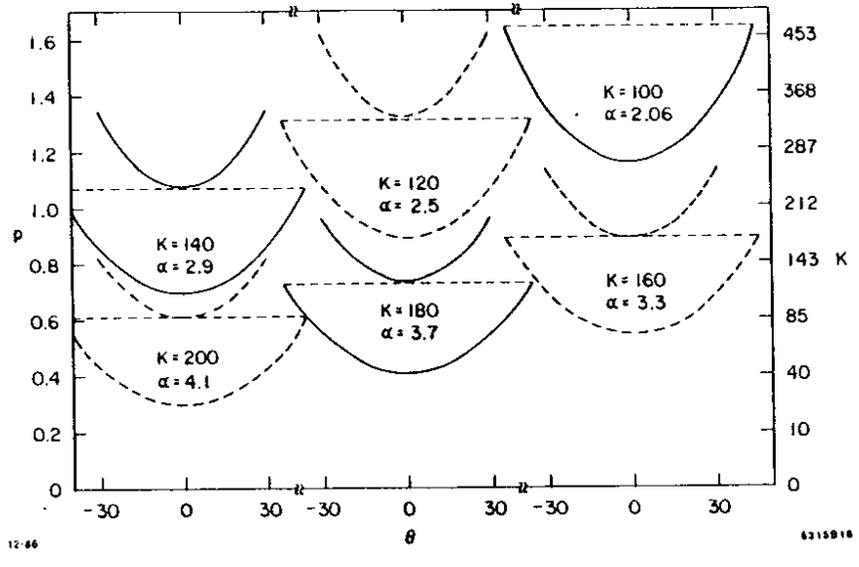

Fig. 2.18. Capture region admittance as a function of normalized field strength. K = electric field strength in kV/cm.

$$p_1 = \frac{\theta_3}{\theta_2}\, p_2 \qquad (2.19) \qquad\qquad \theta_1 = \frac{p_3}{p_2}\, \theta_2 \qquad (2.20)$$

In this case θ_3 is already determined by Eq. (2.30b). As mentioned earlier, maximum phase compression in the buncher is achieved if electrons enter the buncher near the field null and move to $-90°$ in a quarter of the phase space cycle. Thus θ_2 is also determined. From Eq. (2.20) we see that phase acceptance is proportional to the ratio p_3/p_2. Using Eq. (2.34b) and recalling that $p_2 = p_w - p_0$ we have

$$\frac{p_3}{p_2} = \left(\frac{2\pi}{\alpha_3} + \frac{\alpha_3}{2\pi}\right) \frac{\Delta\theta_\infty}{2(p_w - p_0)} \qquad (2.35)$$

Differentiating with respect to p_w we find

$$\frac{d(p_3/p_2)}{dp_w} = -\left(\frac{2\pi}{\alpha_3} + \frac{\alpha_3}{2\pi}\right) \frac{\Delta\theta_\infty}{2(p_w - p_0)^2}$$

Since $\Delta\theta_\infty$, α_3 and $(p_w - p_0)^2$ are all positive quantities,

$$\frac{d\,(p_3/p_2)}{dp_w} = \frac{1}{\theta_2}\,\frac{d\theta_1}{dp_w} < 0 \quad . \qquad (2.36)$$

Thus as the phase velocity β_w of the buncher increases, the phase acceptance decreases, while [by Eq. (2.19)] the momentum acceptance increases.

Using Eqs. (2.19), (2.20), (2.30b), and (2.35) we can calculate the phase and momentum acceptances for a range of phase velocities. The results appear in columns 5 and 6 of Table 2.3.

As mentioned earlier, should the initial phase space occupied by the beam be large, we cannot expect mappings to be undistorted. For an accurate prediction of the effect of buncher phase velocity on phase and momentum acceptance, we must numerically integrate Eqs. (2.4) and (2.5) for key phase space trajectories.

Table 2.3. Buncher admittance as a function of phase velocity, β_w.

$\Delta E/E = .01$, $p_0 = .7410$, $\theta_3 = 30.8°$, and $\theta_2 = -90°$

1	2	3	4	5	6	7	8	9	10	11	12
β_w	p_w	α_3	α_2	Linear Appr. $2p_1$	Linear Appr. $2\theta_1$	$4p_3\theta_3$ $(4p_1\theta_1)$	Integrated Area Cap. Reg.	$2\theta_1$	$2p_1$	Approx. $4\theta_1 p_1$	Integrated Area Buncher
.7071	1.0	2.60	.120	.177	141	25.0	24.2	180	.13	23.4	27.3
.75	1.134	2.37	.230	.269	100	26.8	26.5	150	.21	31.5	29.9
.7682	1.2	2.28	.288	.314	88	27.6	26.9	130	.25	32.3	32.5
.8137	1.4	2.01	.466	.451	68	31.7	31.5	120	.32	38.4	36.1
.8480	1.6	1.80	.639	.588	57	33.4	31.9	100	.40	40.0	40.3
.8742	1.8	1.63	.800	.725	50	36.5	35.3	90	.48	43.2	41.0

Specifically, we wish to know the phase space occupied by the perimeter of the capture region admittance one-quarter cycle earlier in phase space (i.e., at the entrance to the buncher). This shows us the perimeter of the buncher admittance. As a practical matter, it is simpler to have particles move forward in time through the computer code which numerically integrates Eqs. (2.4) and (2.5). This is equivalent to clockwise motion around the phase space orbits of Fig. 2.4. Because these orbits are symmetrical about the $\theta = 0$ axis, we can use a "mirror image" of the capture region perimeter as input to the computer code. A quarter of a cycle later, this input has been transformed to the usable phase space at the entrance to the buncher.

Buncher admittance as a function of buncher phase velocity is illustrated in Figs. 2.19(a-f). The higher enclosed region of each plot represents the acceptance of the capture region for electrons with mean momentum p_w (i.e., the mean momentum of the bunch after one quarter cycle in buncher phase space). Note that for greater clarity the boundary of the capture region phase space is truncated at p_b of Fig. 2.8. The lower region represents the corresponding admittance of the buncher. As predicted in columns 5 and 6 of Table 2.3, as p_w increases the total admittance of the buncher grows (i.e., $\theta_1 p_1$) but the phase acceptance shrinks.

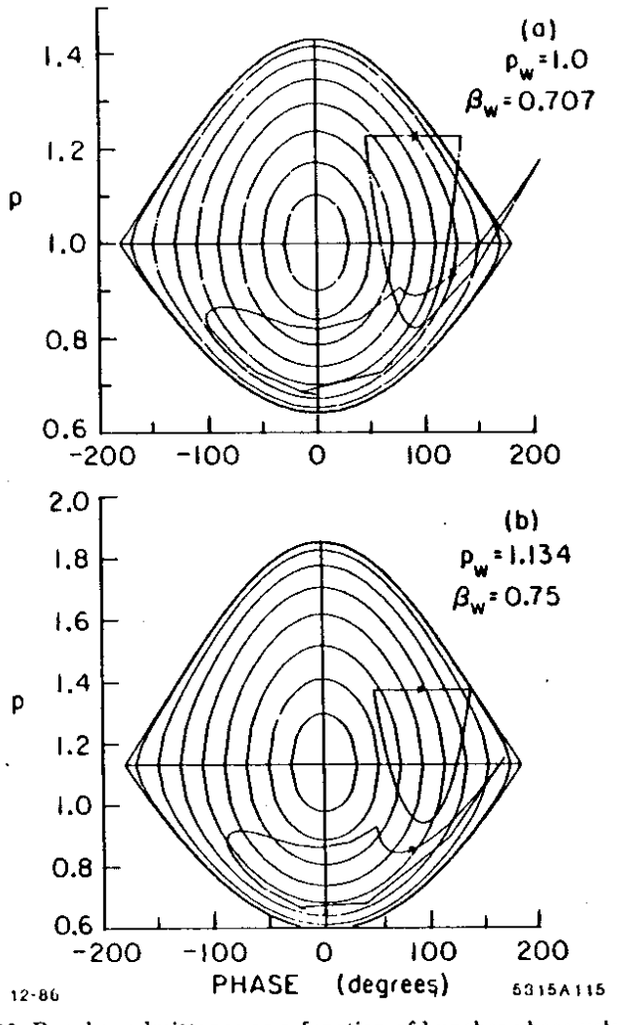

Fig. 2.19. Buncher admittance as a function of buncher phase velocity. The higher enclosed region of each plot is the acceptance of the capture region for $\Delta E/E = .01$. The lower enclosed region is the corresponding buncher admittance for $p_0 = .741$, and a) $p_w = 1.0$, b) $p_w = 1.134$, c) $p_w = 1.2$, d) $p_w = 1.4$, e) $p_w = 1.6$, and f) $p_w = 1.8$

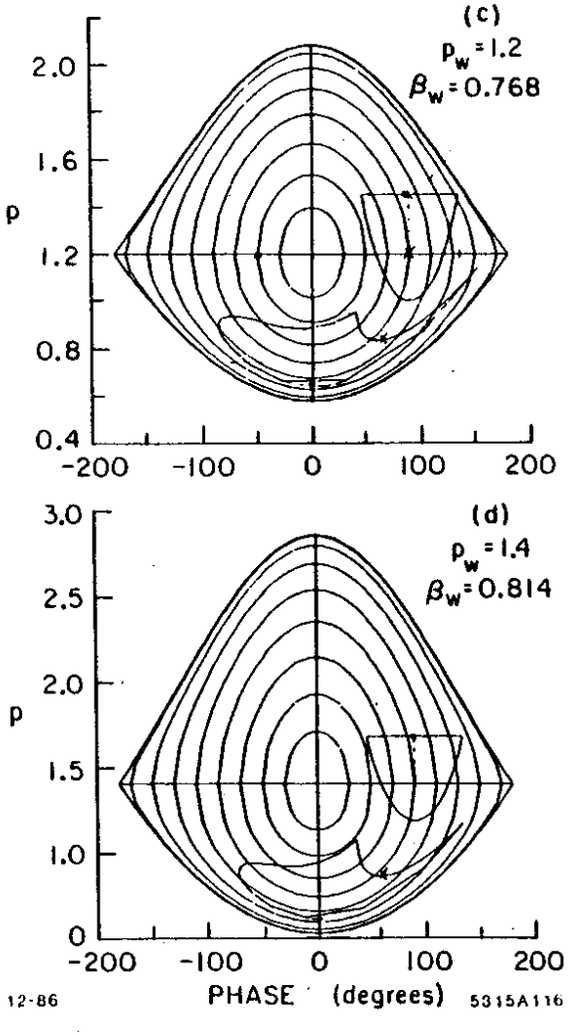

Fig. 2.19(c) and (d)

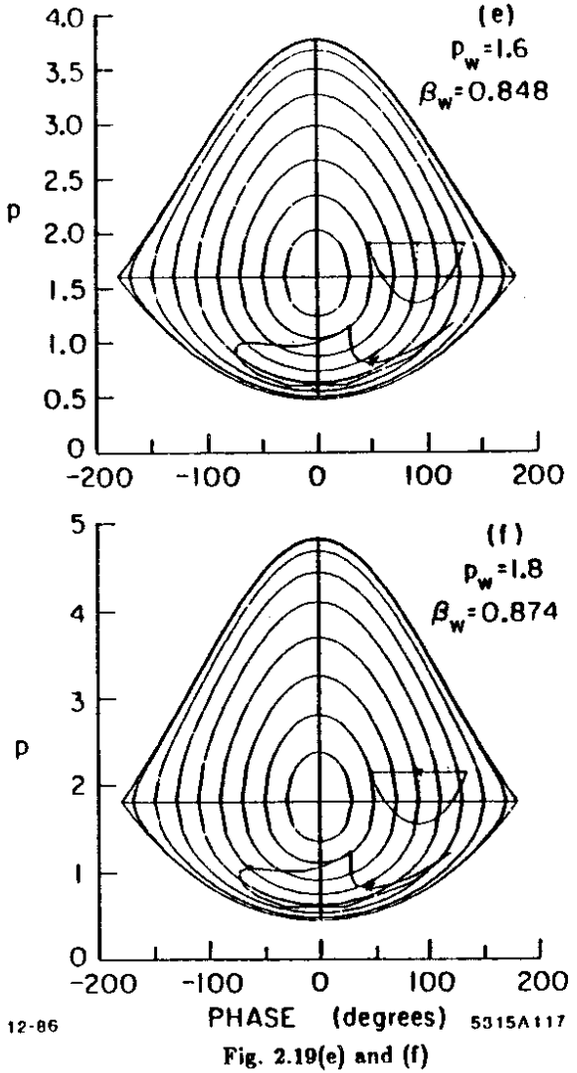

Fig. 2.19(e) and (f)

Columns 9 and 10 of Table 2.3 are the approximate buncher phase and momentum acceptances predicted by Fig. 2.19. Note that as the phase space is distorted during its one-quarter wavelength transformation, the phase acceptances are larger than predicted by the linear theory and the momentum acceptances are smaller. Columns 8 and 12 are the integrated areas of the capture region admittance and the buncher admittance of Fig. 19, respectively. Note that the buncher admittance has a slightly larger area than the capture region admittance for a given phase velocity. However, the shape of the acceptance region may be too distorted to take advantage of this increase.

In the CID injector we can anticipate that phase compression by a gap-and-drift buncher will be limited by opposing space charge forces. Thus we should choose a phase velocity which allows generous phase acceptance, probably in the range of $\beta_w = .70$ to $\beta_w = .80$. At the time SLAC's main injector was built, two extra buncher/capture region sections were manufactured. These consist of a 10.5 cm long $\beta_w = .75$ buncher and a 3 meter velocity-of-light capture region. From Fig. 2.19a-c we see that this section falls within the appropriate range of β_w.

Given a buncher admittance from the phase space plots of Fig. 2.19, we must now optimize the parameters of the gap-and-drift buncher to achieve a beam emittance matched to the buncher admittance. Assume that the gun produces a roughly Gaussian pulse with initial velocity β_0 (see Fig. 2.20). The pulse passes through a short gap at z_0; the center of the pulse crosses z_0 at time $t = 0$. The pulse then drifts for a distance $L = z_f - z_0$; the center particle reaches z_f at time

$$T = \frac{z_f - z_0}{c\beta_s}$$

where β_s is the normalized velocity of the center particle after it has traversed the gap. From Eq. (2.3) we have for each particle

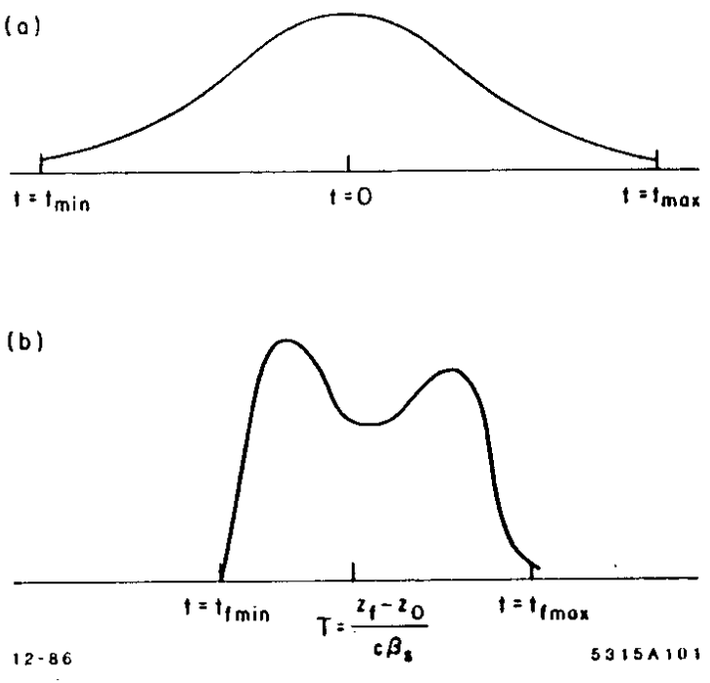

Fig. 2.20. (a) Charge density versus time for a Gaussian-shaped gun pulse. (b) Charge density versus time after sinusoidal gap-and-drift prebuncher with drift length $z_f - z_0$.

$$t_f - t = \frac{L}{c}\left(\frac{1}{\beta} - \frac{1}{\beta_s}\right) \tag{2.37}$$

where

t = time at which the particle crosses z_0

t_f = time at which the particle crosses z_f measured with respect to T.

Perfect bunching is achieved if $t_f = 0$ for each particle. To achieve perfect bunching, we should choose

$$\beta(t) = \left[\frac{1}{\beta_s} - \frac{ct}{L}\right]^{-1} . \tag{2.38}$$

If we choose β_w in the buncher, column 10 of Table 2.3 dictates the minimum and maximum acceptable momenta, p_{max} and p_{min}, with corresponding velocities β_{max} and β_{min}. For good bunching, the particle which enters the gap at the latest time (t_{max} of Fig. 2.20a) should leave the gap with the greatest velocity β_{max}. Likewise the first particle through the gap ($t_{min} = -t_{max}$) should have final velocity β_{min}. Substituting into Eq. 2.38 we have

$$\beta_{max} = \left[\frac{1}{\beta_s} - \frac{ct_{max}}{L}\right]^{-1} \qquad \beta_{min} = \left[\frac{1}{\beta_s} - \frac{ct_{max}}{L}\right]^{-1} . \tag{2.39}$$

We can now solve for β_s and L

$$\beta_s = \frac{2}{1/\beta_{min} + 1/\beta_{max}} \tag{2.40}$$

$$L = \frac{ct_{max}}{1/\beta_s - 1/\beta_{max}} . \tag{2.41}$$

For $\beta_w = .75$ in the buncher, $\beta_{max} = .656$ and $\beta_{min} = .551$. From Eqs. (2.40) and (2.41), we find $\beta_s = .5989$ and $L = 174$ cm. For a 1 ns FWHM Gaussian

gun pulse, the $\pm 2\sigma$ points fall at $\pm .85$ ns. The optimum β versus t curve [from Eq. 2.38)] for a 1 ns gun pulse is graphed in Fig. 2.21. Note that the desired $\beta(t)$ grows slightly faster than linearly, because $1/\beta$ varies linearly with t. The normalized energy, $\gamma_1(t)$, required to achieve this $\beta(t)$ is

$$\gamma_1(t) = \left[1 - \beta(t)^2\right]^{-1/2} = \left[1 - \left(\frac{1}{\beta_s} - \frac{ct}{L}\right)^{-2}\right]^{-1/2} \qquad (2.42)$$

$\gamma_1(t)$ is graphed in Fig. 2.22. We see that over such a large range $\gamma_1(t)$ is far from linear. Thus the best bunching is not accomplished simply by choosing a low enough gap frequency so that the entire gun pulse falls on the linear region of the sine wave. Rather, we should exploit the curvature of the sine function by shifting the phase of the pulse with respect to the null of the sine wave to optimize bunching.

Figure 2.23 suggests that the sine function is most similar to the $\gamma_1(t)$ function if the center of the pulse is shifted to the left of the null and the frequency is chosen such that the pulse subtends approximately 90° of phase. t_{max} then falls in the linear region of the accelerating sine wave and t_{min} falls just after the decelerating crest, that is

$$-45° < \omega t_s < -15° \qquad (2.43a)$$

$$0° < \omega(t_s + t_{max}) < 30° \quad \text{and} \quad -90° < \omega(t_s + t_{min}) < -60° \qquad (2.43b)$$

where

ω = radial frequency of the accelerating field in the gap

ωt_s = phase shift of the center particle with respect to the null of the accelerating field.

The actual energy $\gamma_2(t)$ of a particle after traversing the gap is given by Eq. (2.1) (note that we now write γ as a function of t rather than θ):

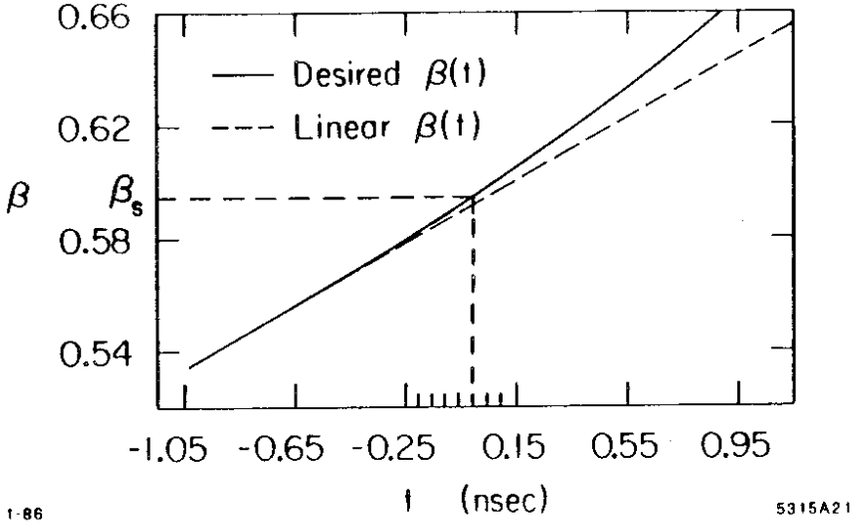

Fig. 2.21. Normalized velocity as a function of time needed to achieve perfect bunching of a Gaussian gun pulse with a σ of 0.5 ns.

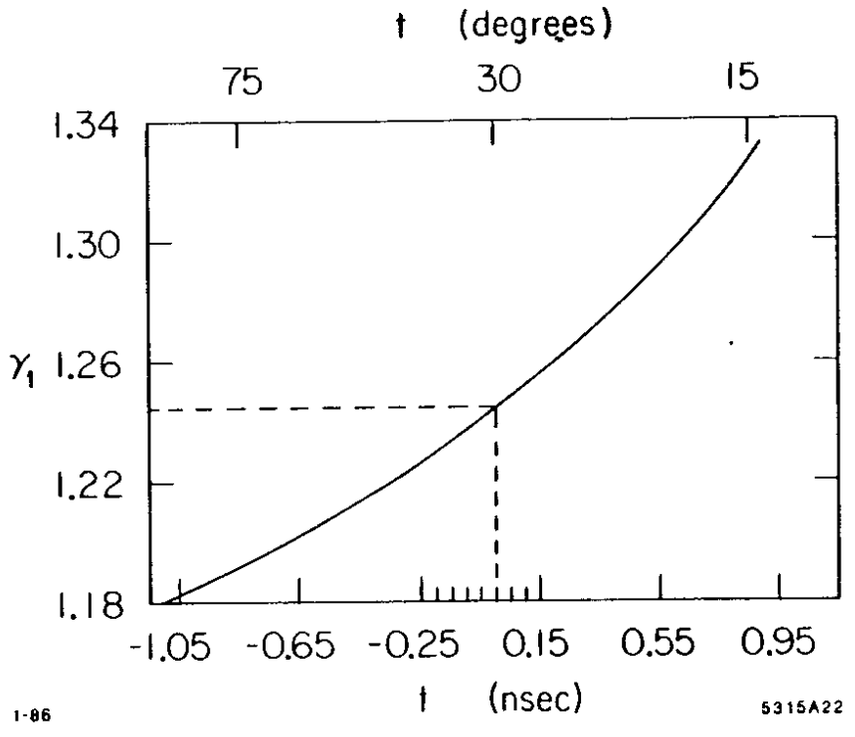

Fig. 2.22. Normalized energy as a function of time needed to achieve perfect bunching of a Gaussian gun pulse with a σ of 0.5 ns.

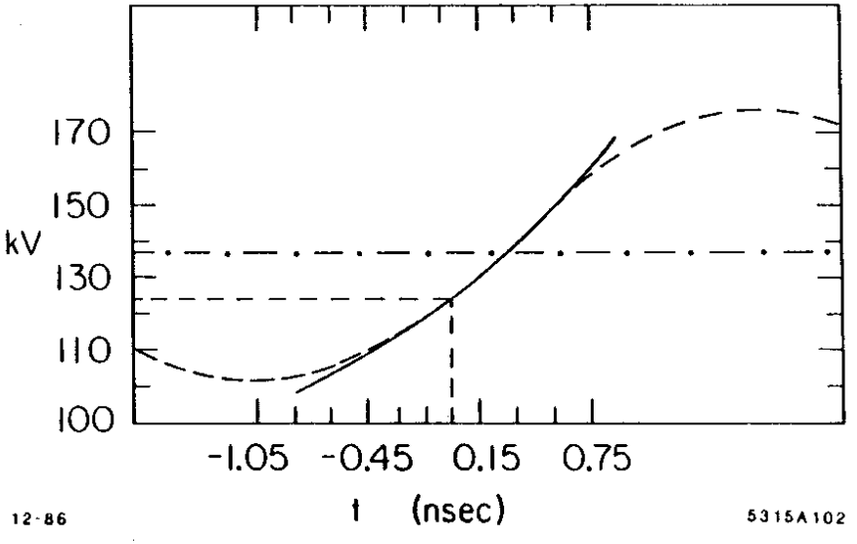

Fig. 2.23. γ versus t curve of Fig. 2.22 superimposed on sine wave.

$$\begin{aligned}\gamma_2(t) &= \gamma_0 + \alpha\xi_{gap}\sin\omega(t_s + t) \\ &= \gamma_0 + \mathcal{E}\sin\omega(t_s + t)\end{aligned} \tag{2.44}$$

where $\mathcal{E} = \alpha\xi_{gap}$ and the slope is

$$\gamma_2'(t) = \omega\mathcal{E}\cos\omega(t_s - t) \quad .$$

We choose the phase shift ωt_s by requiring that the ratio of the slopes at the extremes of the pulse be equal for both γ functions; that is, we choose ωt_s by requiring

$$\frac{\gamma_1'(t_{max})}{\gamma_1'(t_{min})} = \frac{\gamma_2'(t_s + t_{max})}{\gamma_2'(t_s + t_{min})} \quad . \tag{2.45}$$

The slope of $\gamma_2(t)$ in the linear region ($-30° < \omega t < 30°$) is approximately $\omega\alpha\xi_{gap}$. The ratio of this slope at t_{max} to the slope at t_{min} is thus

$$\frac{\gamma_2'(t_s + t_{max})}{\gamma_2'(t_s + t_{min})} \simeq \frac{\omega\alpha\mathcal{E}_{gap}}{\omega\alpha\mathcal{E}_{gap}\cos\omega(t_s + t_{min})} = \frac{1}{\cos\omega(t_s + t_{min})} \quad . \tag{2.46}$$

The slope of $\gamma_1(t)$ is given by

$$\gamma_1'(t) = \frac{c}{L}\left(\frac{1}{\beta_s} - \frac{ct}{L}\right)^{-3}\left[1 - \left(\frac{1}{\beta_s} - \frac{ct}{L}\right)^{-2}\right]^{-3/2} \quad . \tag{2.47}$$

For a gun pulse of 1 ns FWHM, the ratio of $\gamma_1'(t)$ for $t_{max} = +2\sigma = .85$ ns and $t_{min} = -2\sigma = .85$ ns is

$$\frac{\gamma_1'(.85\,\text{ns})}{\gamma_1'(-.85\,\text{ns})} = 2.29 \quad . \tag{2.48}$$

Equating Eqs. (2.46) and (2.48), we have

$$\omega(t_s + t_{min}) = -\arccos\frac{1}{2.29} = -64.1° \quad .$$

Thus the earliest part of the pulse should reach the gap when the phase is $\approx -65°$, which suggests a phase shift of $-20°$ with respect to its original centered position.

As mentioned earlier, we should choose the frequency of the sine wave such that the gun pulse subtends approximately 90° of phase, i.e.,

$$f = \frac{1}{4\sigma}\left(\frac{90}{360}\right) \tag{2.49}$$

where 95% of the pulse charge is contained in $\pm 2\sigma$. For a 1 ns FWHM gun pulse, $4\sigma = 1.7$ ns and Eq. (2.49) yields $f = 146.2$ MHz. The nearest subharmonic of the accelerator frequency (with a reasonable number of harmonics which are also subharmonics of SLAC's 2856 MHz) is the 20th subharmonic $f = 142.8$ MHz.

We now find α_1, the strength of the gap accelerating field, such that $\gamma_2(t)$ is a good fit to $\gamma_1(t)$. In particular, we wish the fit to be as close as possible in the region between $\pm\sigma$, where the initial charge density is highest. We choose the peak voltage of the electric field E such that

$$\gamma_1(\sigma) - \gamma_1(-\sigma) = \gamma_2(\sigma) - \gamma_2(-\sigma)$$

or

$$KE_1(\sigma) - KE_1(-\sigma) = KE_2(\sigma) - KE_2(-\sigma) \tag{2.50}$$

where

KE_1 = kinetic energy of a particle required for perfect bunching

KE_2 = kinetic energy of a particle produced by a sine wave.

Thus

$$E = \frac{KE_1(\sigma) - KE_1(-\sigma)}{\sin(\omega\sigma + \omega t_s) - \sin(-\omega\sigma + \omega t_s)}$$

for $\omega t_s = -20°$ and $\sigma = .425$ ns

$$E = \frac{31.6}{\sin[21.8 - 20] - \sin[-21.8 - 20]} = 45.2\,\text{kV} \quad . \tag{2.51}$$

Initially, we estimated the phase shift by requiring that the ratio of the slopes at the extremes of the pulse be equal for γ_1 and γ_2. Since a good match between γ_1 and γ_2 is most important at the center of the pulse, we correct t_s and E to satisfy Eqs. (2.40) and (2.50). From Eq. (2.40) we find $\beta_s = .5989$ which corresponds to $KE_1(t_s) = 127.1$. Thus we want

$$KE_2(t_s) = KE_0 + E\sin t_s = 150 + 45.2\sin(\omega t_s) = 127\,\text{kV} \tag{2.52}$$

where

KE_0 = initial voltage of the gun pulse = 150 keV.

Solving for $\omega t_s = \theta_s$

$$\theta_s = \arcsin\left[\frac{22.9}{45.2}\right] = 30.5° \quad . \tag{2.53}$$

Iterating between Eqs. (2.40) and (2.50), we find suitable values of E and θ_s to satisfy both conditions,

$$\theta_s = -28.3° \qquad E = 48.2\,\text{kV} \quad . \tag{2.54}$$

The kinetic energy desired for perfect bunching, $KE_1(t)$, and the kinetic energy produced by the electric field $KE_2(t)$, are shown in Fig. 2.24. We now have a complete system design which bunches a 1 ns low current gun pulse for capture into a 1% energy spectrum in the accelerator. This design is summarized in Table 2.4.

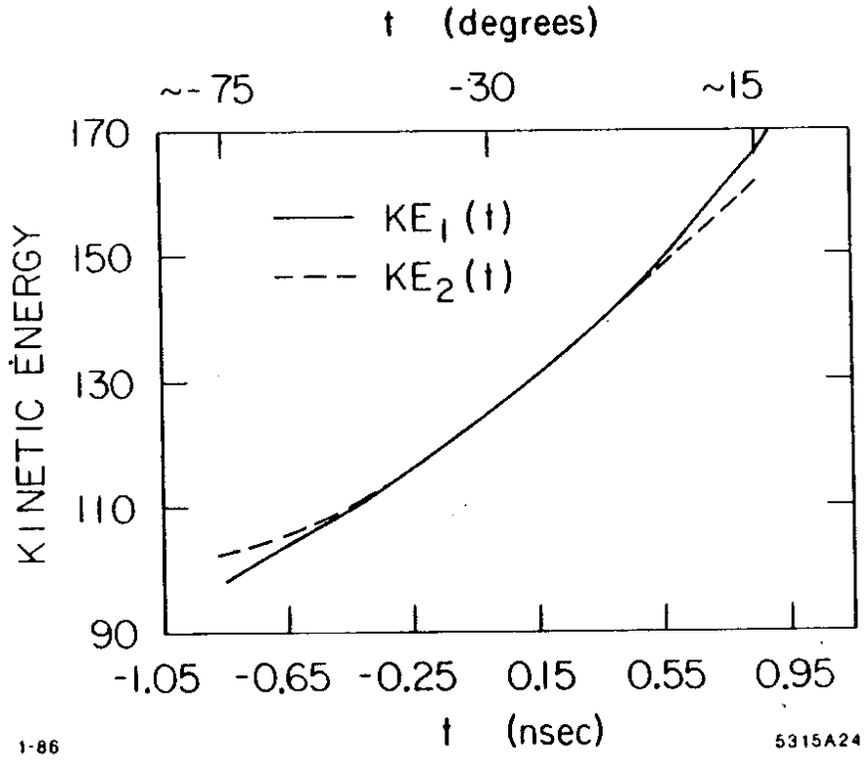

Fig. 2.24. Kinetic energy, $KE_1(t)$, versus time needed to achieve perfect bunching compared to energy, $KE_2(t)$, versus time achieved by 20th subharmonic sine wave.

Table 2.4. Injector specifications in the low current, large signal limit. $\Delta\theta$ and Δp are given at end of element.

Element	kV/cm	Length (cm)	β_w	$\Delta\theta\,(\pm 2\sigma)$	Δp	$\Delta E/E$
Gun	—	—	.63	1700°	0	
20^{th} Subharmonic prebuncher	13	3.8 gap 176 drift	—	45°	.19	
Buncher	11	10.5	.75	60°	.10	

Equations (2.4a) and (2.4b) were numerically integrated to determine the electron phase space orbits in the bunching system. The theoretical performance of the "Table 2.4" injector is summarized in the phase space plots of Fig. 2.25.

Figure 2.25 shows the phase space at the end of the prebuncher drift space. The original gun pulse, some 1700 S-band degrees long, has been compressed into $\sim 40°$ of phase. This bunching is good enough that, in the absence of space charge, we could omit the $\beta_w < 1$ traveling-wave structure and still capture almost all of the charge in the gun pulse into a 1% spectrum. After a quarter-wave transformation, we plot the beam emittance at the output of the buncher. The transformation in the buncher is reasonably linear as the shape of the beam in phase space is well preserved. Note that the phase spread at the output of the buncher is larger than the phase spread at the input, although the outgoing emittance is still within the capture region acceptance. The final buncher phase spread is dominated by the large momentum spread at the entrance to the buncher. Clearly we have not optimized the long gun pulse, low current design, but that is not our intent. The "Table 2.4" injector is intended only as a jumping-off point for the high current design.

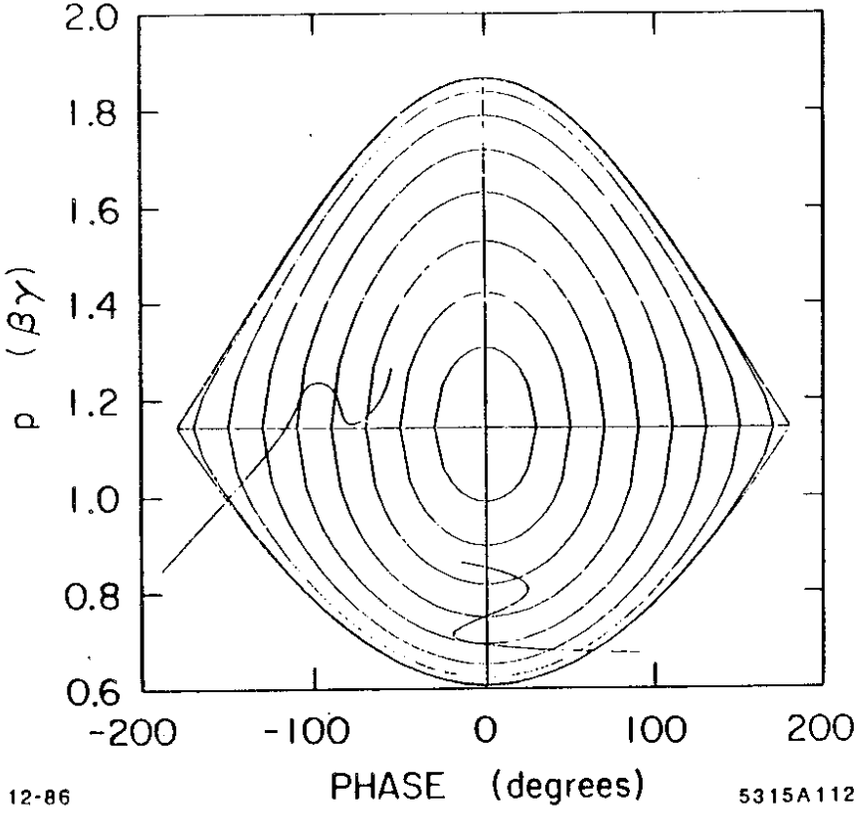

Fig. 2.25. Beam emittance at the entrance to and exit of the $\beta_w = .75$ buncher for the "Table 2.4" design.

2.2.2 *"Gedanken"* High-Current, Large Signal Injector Design

Having completed a low-current design, we now consider the effects of space charge on the bunching process. In the crudest approximation, we can think of space charge as adding a spring-like quality to the beam pulse. For example let us consider the gap-and-drift prebuncher. The bunch crosses the gap where the sinusoidal electric field imparts a momentum kick to the electrons. In the drift space, the electrons begin to converge on the center particle. The space charge forces grow greater as the bunch compresses, impeding further bunching. Eventually, the initial momentum kick imparted to the beam at the gap is offset, then overcome by the space charge forces and the beam begins to debunch.

Rather than attempting to develop a simple analytic model of bunching in the presence of space charge forces, we have used a computer simulation to understand the longitudinal dynamics. For the sake of continuity, the details of the computer model are described in the next section. At this point, a brief qualitative description of the model will suffice. We model the beam as a finite number of infinitely thin disks and rings of charge in an infinitely long conducting cylinder (see Fig. 2.26). The annuli are free to move longitudinally, but their radii and charge densities are fixed throughout a given bunching element. The space charge forces between annuli are found by solving for the average static forces between annuli surrounded by the grounded conducting cylinder. The change in the energy of each annulus due to all other annuli is computed. Equation (2.4) becomes

$$\frac{d\gamma}{d\xi} = -\alpha \sin\theta + \text{energy change due to presence of other annuli.} \qquad (2.55)$$

The longitudinal dynamics of the electron pulse are calculated by numerical integration of Eqs. (2.55) and (2.5).

The gap-and-drift prebuncher of the "Table 2.4" injector is modeled using 31 disks ('annuli' of inner radius 0) of radius .93 cm and 31 annuli of inner

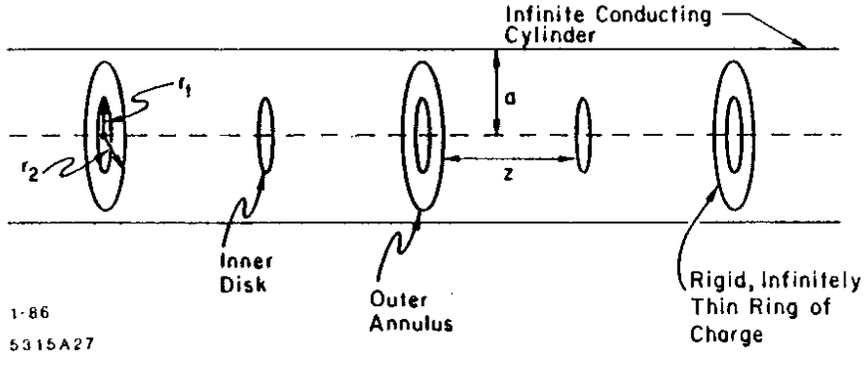

Fig. 2.26. Schematic diagram of model used to calculate longitudinal beam dynamics in the presence of space charge forces.

radius .93 cm and outer radius 1.75 cm. The annuli are initially spaced evenly over the length of the gun pulse; the charge on each annulus is weighted to reflect the Gaussian distribution of the gun pulse. The phase and momentum of each annulus are calculated as functions of the z position in the gap-and-drift prebuncher.

Figure 2.27(a) is a plot of phase (with respect to the center of the pulse) versus z position of every third of the 31 inner disks traveling though the gap and drift prebuncher. The gap is at the far left, at $z = 0$ to $z = 3.8$ cm. The initial 1700° bunch compresses to approximately 40° of S-band phase at the waist at $z = 176$ cm. Figures 2.27(b-e) represent the same initial bunch traversing the same structure in the presence of increasing space charge forces. The plots represent peak gun currents of 3, 6, 9, and 12 amps, respectively. (A gun current of 12 amps is required to produce 7.5×10^{10} electrons in a 1 ns FWHM pulse.) As the gun current increases, the phase spread at the waist increases but the waist is located at the same z position.

The corresponding θ versus z plots for the outer annuli are plotted in Figs. 2.28(a-e). Note that the space charge forces are considerably weaker for the outer annuli. The reasons for this are discussed in the next section.

Figures 2.29(a-e) are plots of the longitudinal phase space at the waists ($z =$ 176 cm) of Figs. 2.27(a-e) and 2.28(a-e). In the absence of space charge, the disks move past each other in a smooth manner [i.e., Figs. 2.27-2.29(a)]. In the presence of space charge, the disks are sometimes "scattered" by other disks causing "hernias" in the phase space diagrams. This may be an artifact of the model, and we shall address this point again in the next section. Notice that in the presence of appreciable current ($\geq$3 amps), the momentum spread of the inner disks is quite narrow. As the current increases the minimum phase spread increases. For a gun current of 12 amps, the phase spread is $\sim$ 400° of S-band (see Fig. 2.30e), too large to be captured into the buncher phase acceptance.

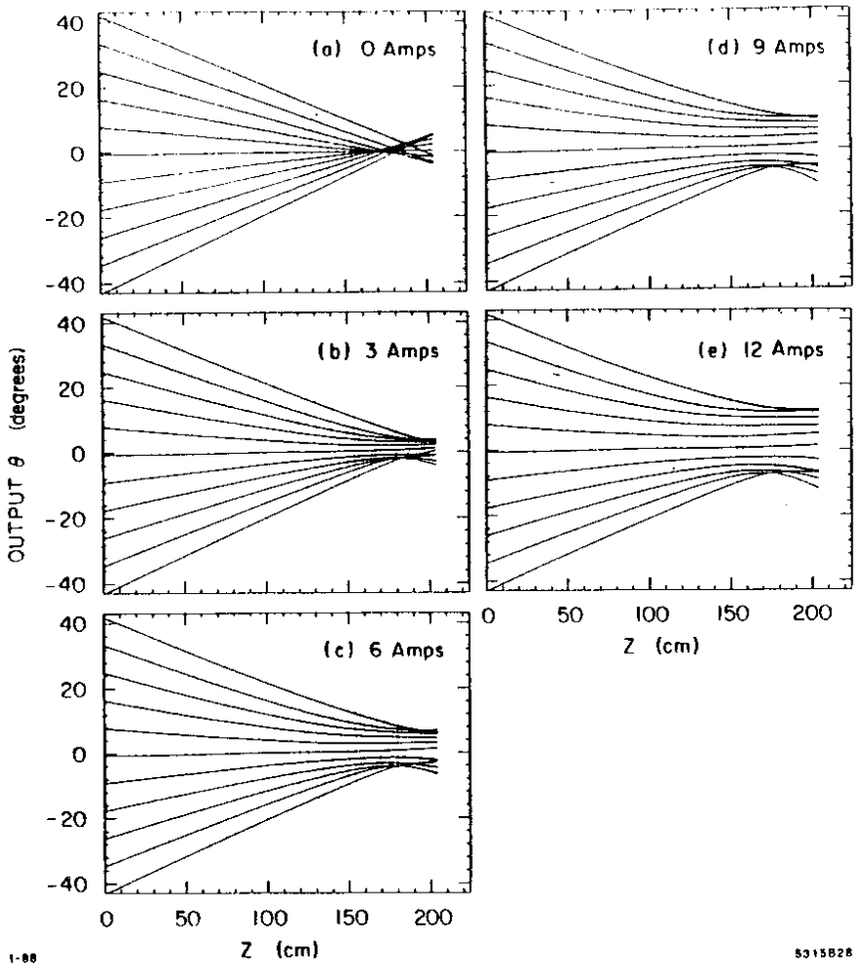

Fig. 2.27. θ versus z for every third of the 31 inner disks of charge traversing the gap-and-drift prebuncher specified in Table 2.4 as the current increases from 0 to 12 amps. θ is given in degrees at the 20th subharmonic of S-band.

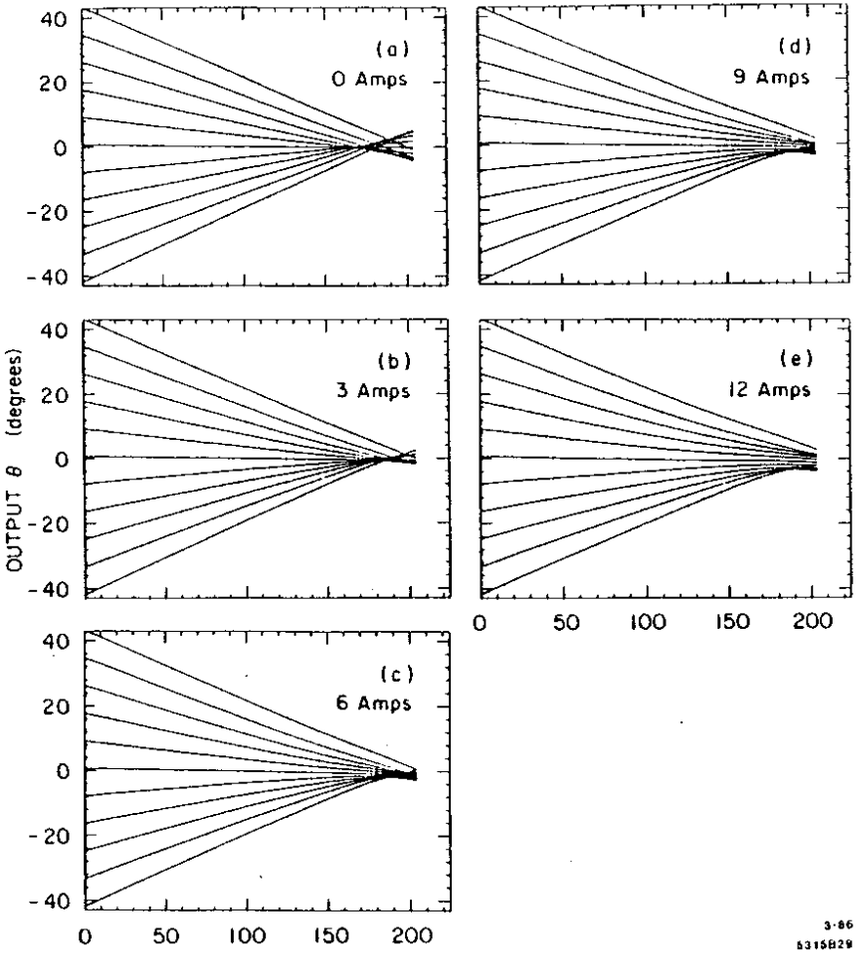

Fig. 2.28. θ versus z for every third of the 31 outer annuli of charge traversing the gap-and-drift prebuncher specified in Table 2.4 as the current increases from 0 to 12 amps. θ is given in degrees at the 20th subharmonic of S-band.

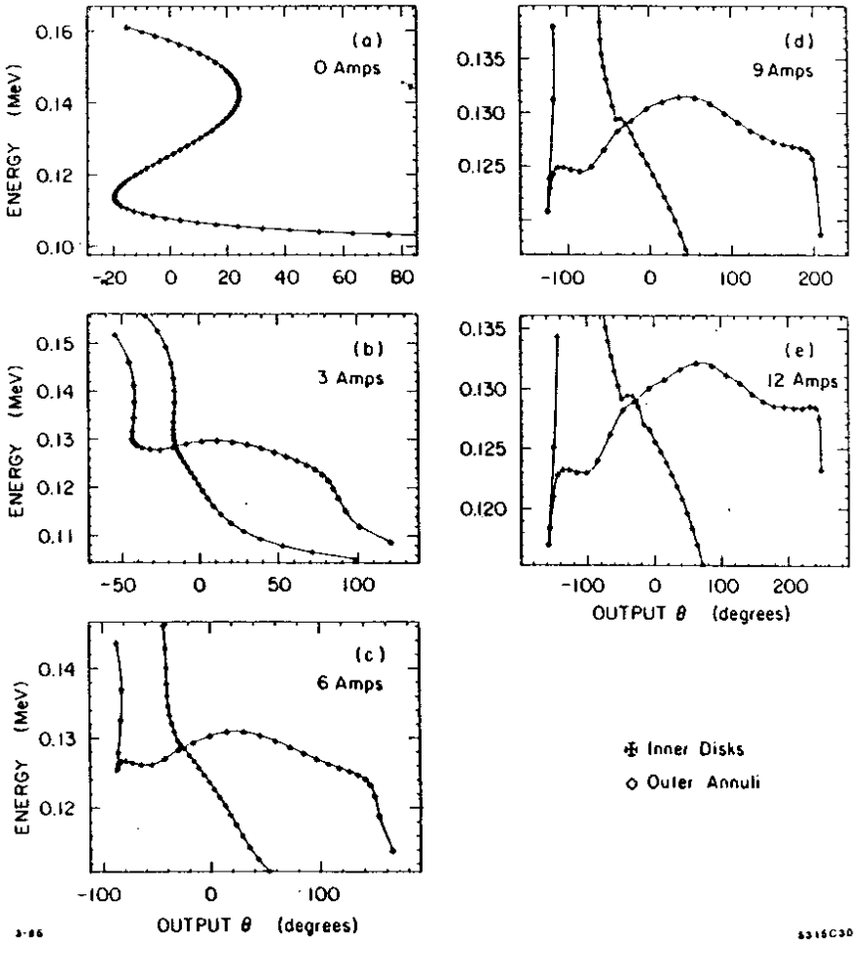

Fig. 2.29. Longitudinal emittance at the end of the gap-and-drift prebuncher specified in Table 2.4 as the current increases from 0 to 12 amps. θ is given in degrees at S-band.

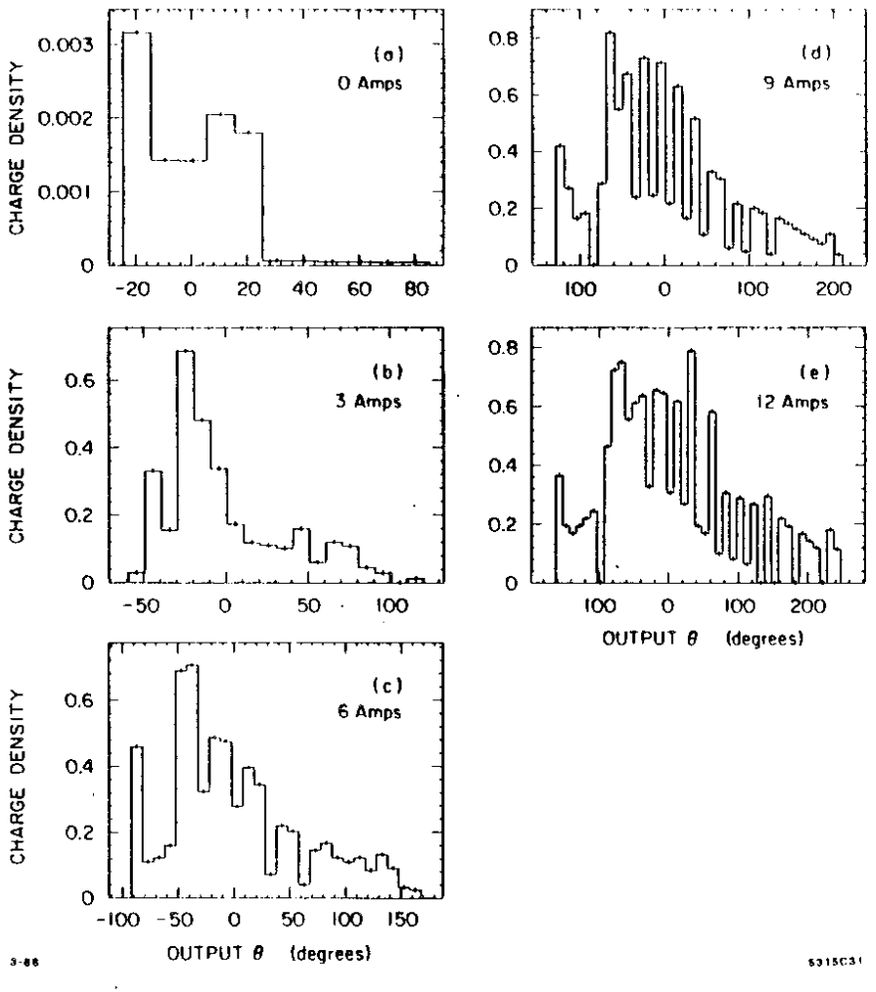

Fig. 2.30. Bunch length at the end of the gap-and-drift prebuncher specified in Table 2.4 as the current increases from 0 to 12 amps. θ is given in degrees at S-band. Charge density units are relative.

At this point there are several options for decreasing the phase extent of the bunch entering the $\beta_w = .75$ buncher. One option is to increase the strength of the electric field in the prebuncher gap. Three considerations suggest that this may not be the best approach:

1. In doing this we abandon our matching of the amplitude and phase of the field in the gap to offset the inherent asymmetry in bunching relativistic electrons with appreciable field strengths.
2. Increasing the gap field strength increases the disparity between the phase spaces of the inner disks and outer annuli, and this in turn increases the total phase space occupied by the bunch.
3. We find that as the gap field strength increases, the "hernias" grow, and this increases the effective emittance of the bunch.

Another approach is to put a second gap-and-drift prebuncher at the phase waist. Since the outer annuli are bunched appreciably better than the inner disks, we should concentrate on bunching the disks as we choose the parameters of the second gap-and-drift buncher. Note that, with the exception of the "hernia" at the far left, the energy spread of the disks in Fig. 29(e) is reasonably small and clustered about the energy of the center particle after passing the first gap. Hence it seems sensible to use the same approach to design the second gap-and-drift prebuncher as we used for the first.

The bunch now spans 400 ps, and Eq. (2.49) yields $f = 625$ MHz, which falls between the fourth and fifth subharmonics of SLAC's S-band frequency. Choosing the highest reasonable frequency has a slight advantage in that less phase shift is needed to exploit the asymmetry of the sine wave, and the beam centroid is decelerated less. We choose 714 MHz, the fourth subharmonic of S-band. Because the bunch is much more affected by space charge forces in the second gap and drift prebuncher, the gap field strength and drift length are found using the computer model.

In optimizing the gap field strength, we must strike a compromise between the very different dynamics of the inner and outer annuli. Figures 2.31(c) and 2.32(c) show 11 of the 31 disks (annuli) traversing a second gap at the fourth subharmonic and a 24 cm drift space. The outer annuli see much less space charge and are bunched more rapidly. As the gap field strength increases the disparity between the optimum drift for the disks and annuli grows. On the other hand, as the gap field decreases (and the drift increases) we reach a point where the inner annuli are not bunched at all. The solution shown in Figs. 2.31 and 2.32 where $E = 64$ kV, $L = 24$ cm is a compromise between these competing factors.

The longitudinal beam emittance and bunch length at the end of the 24 cm drift are shown in Figs. 2.33(c) and 2.34(c), respectively. From Fig. 2.33(c) it is clear that the phase spaces occupied by the inner disks and outer annuli are quite different, the disks having a larger phase extent but smaller momentum extent. The calculation giving rise to Fig. 2.34(c) predicts that 90% or so of the charge is contained within 200° of S-band which can reasonably be captured by the $\beta_w = .75$ S-band buncher.

In Fig. 2.35 the emittance of Fig. 2.33(c) is superimposed on the low current buncher phase space orbits. These orbits were calculated in the absence of space charge. The electrons in the high current bunch are subject to space charge forces and their trajectories in phase space will not, in general, follow these orbits. We include them principally as reference trajectories. As anticipated, the bunch has a large phase spread and relatively narrow momentum spread. The modeling predicts that a buncher field strength of $\alpha_2 = .56$ (about 2.5 times that calculated for the Table 2.3 buncher) results in the best bunching. The resulting emittance and bunch length are shown in Figs. 2.33(d) and 2.34(d) respectively. Most of the charge is now contained within 50°. Note that the dynamics in the buncher resemble those of the capture region in that the bunch "folds over" about the centroid. The "fold over" increases the bunching of the inner disks which enter the buncher with a large phase extent. Note also that because of the larger α_2, the centroid of the bunch exits the buncher with $p = 1.28 > p_w$.

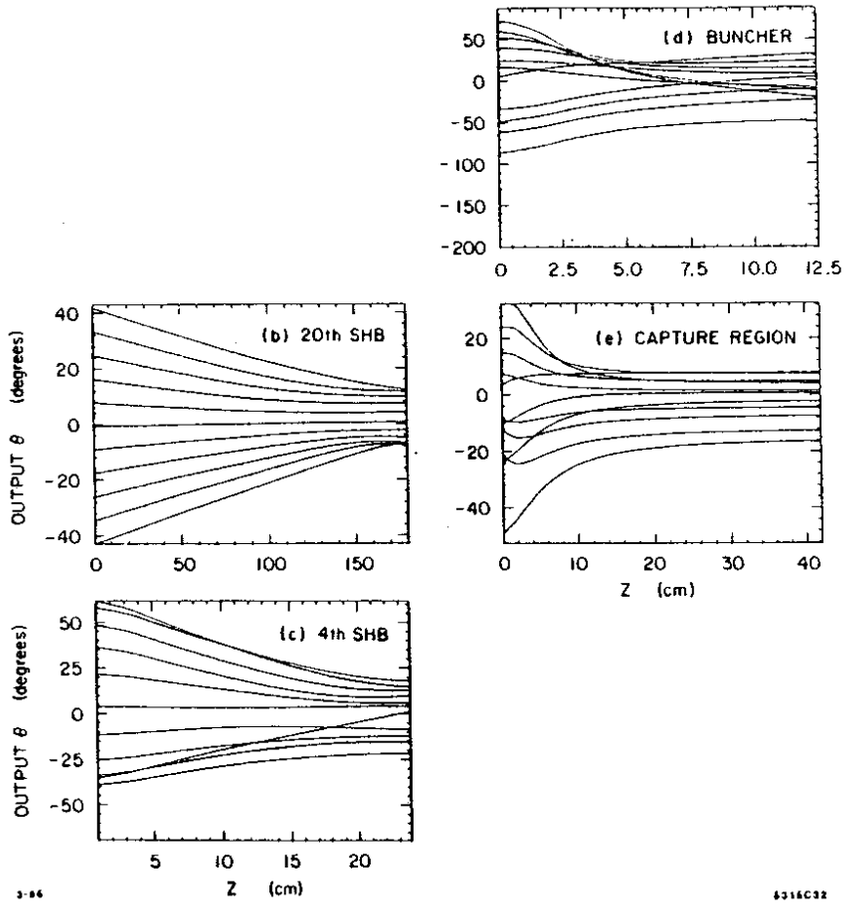

Fig. 2.31. θ versus z for every third of the 31 inner disks of charge traversing the injector specified in Table 2.4. (b) 20th subharmonic gap and 176 cm drift (θ given in degrees at 20th subharmonic). (c) 4th subharmonic gap and 20 cm drift (θ given in degrees at 4th subharmonic). (d) 10.5 cm S-band buncher and 2 cm drift (θ given in degrees at S-band). (e) First 40 cm of velocity-of-light accelerator section (θ given in degrees at S-band).

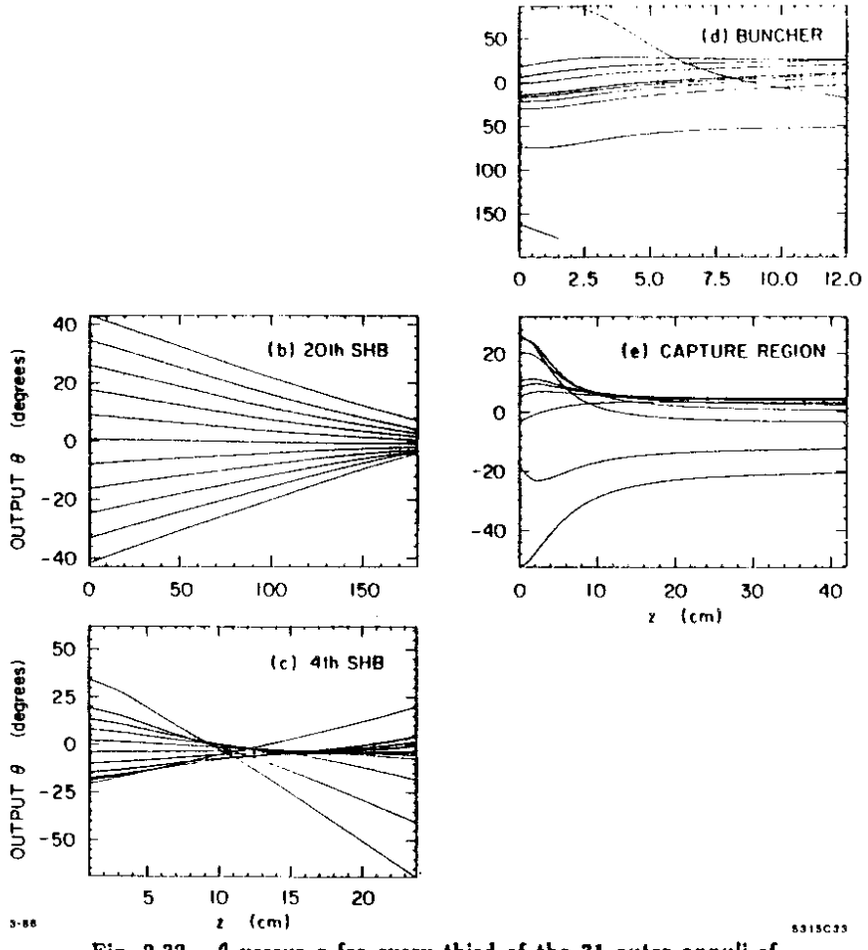

Fig. 2.32. θ versus z for every third of the 31 outer annuli of charge traversing the injector specified in Table 2.4. (b) 20th subharmonic gap and 176 cm drift (θ given in degrees at 20th subharmonic). (c) 4th subharmonic gap and 20 cm drift (θ given in degrees at 4th subharmonic). (d) 10.5 cm S-band buncher and 2 cm drift (θ given in degrees at S-band). (e) First 40 cm of velocity-of-light accelerator section (θ given in degrees at S-band).

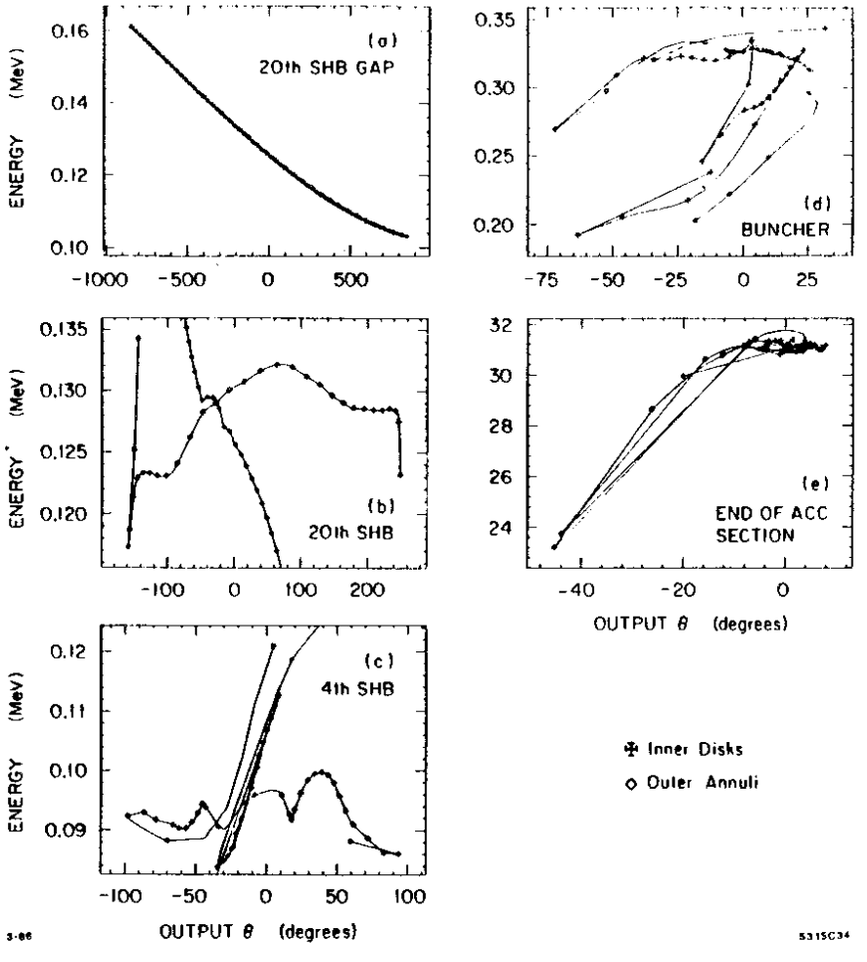

Fig. 2.33. Longitudinal emittance at five locations in the injector specified in Table 2.4. (a) Just downstream of the 20th subharmonic gap. (b) End of 176 cm drift. (c) End of 20 cm drift following 4th subharmonic gap. (d) End of S-band buncher. (e) End of three-meter meter accelerator section. In all figures, θ is measured in degrees at S-band.

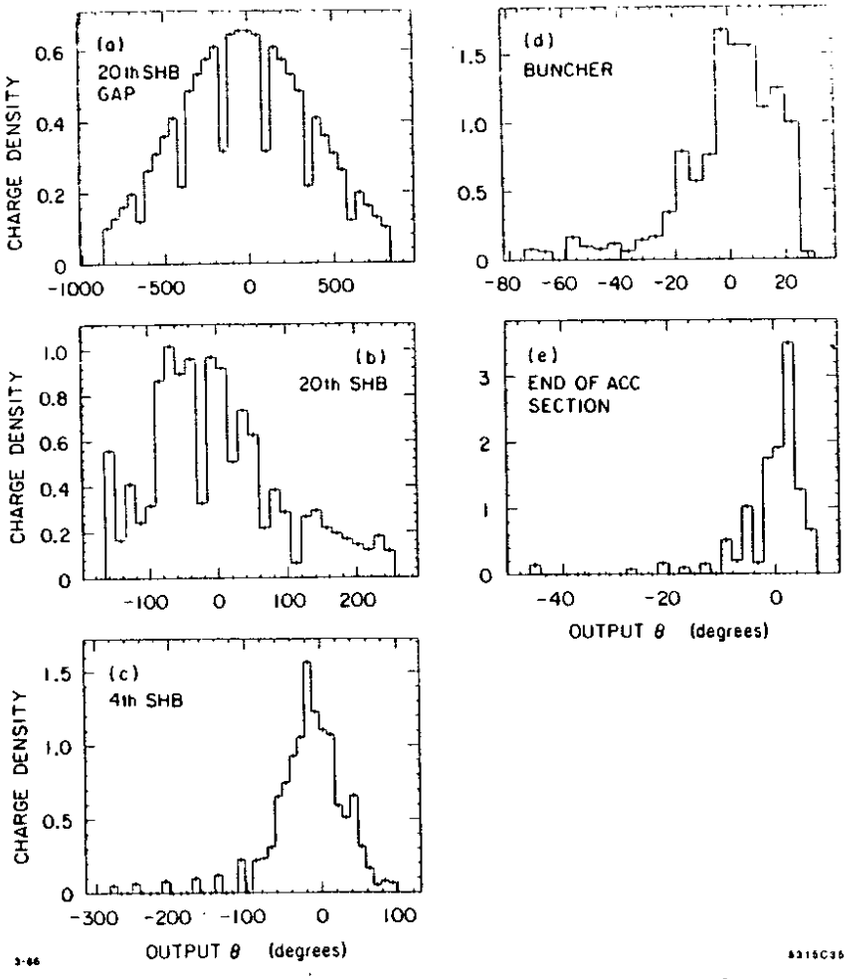

Fig. 2.34. Bunch length at five locations in the injector specified in Table 2.4. (a) Output of the 20th subharmonic gap. (b) End of 176 cm drift. (c) End of 20 cm drift following 4th subharmonic gap. (d) End of S-band buncher. (e) End of three-meter accelerator section. In all figures, θ is given in degrees at S-band. Charge density units are relative.

We use Eq. (2.30) to calculate the optimum value of the field strength in the capture region for $p_w = 1.28$. We find $\alpha_3 = 2.16$. In Fig. 2.36 the emittance at the end of the buncher is superimposed onto the low current phase space trajectories of a capture region with $\alpha_3 = 2.16$. The calculations which give rise to Fig. 2.36 predict that after 42 cm most of the charge falls within 10° near −90°. From Figs. 2.31(e) and 2.32(e) we see that the bunch length remains constant after the first 20 cm or so of the capture region. As the beam energy increases, space charge forces fall off as $1/\gamma^2$. In the absence of other effects, the final emittance and bunch length at the end of the three-meter accelerator section are shown in Fig. 2.33(e) and 2.34(e). Approximately 6.8×10^{10} electrons are captured into 18° or a 1.2% spectrum. The parameters of this high current design are summarized in Table 2.5.

Table 2.5. A high current, large signal injector design.
($\Delta\theta$ calculated at output of each bunching element.)

Element	kV/cm	Length (cm)	β_w	$\Delta\theta$	Δp	$\Delta E/E$
Gun	—	—	.6	1700°	0	
20th subharmonic prebuncher	12 (×4 cm)	176	—	400°	.059	
4th subharmonic prebuncher	16 (×4 cm)	20	—	200°	.06	
S-Band buncher	27	10.5(+2)	.75	50°	.25	
Capture region (no wake)	105	42	1.0	18°		
End of accelerator section (no wake)	105	258	1.0	18°		1.2%
Capture region (with wake)	180	42	1.0	14°		
End of accelelerator section (with wake)	180	258	1.0	14°		2%

As the electrons enter the disk-loaded waveguide (i.e., the buncher and accelerator sections), they excite longitudinal and transverse fields known as wake fields. The wake fields generated by electrons at the front of the bunch affect the energy and transverse position and momentum of trailing electrons. The longitudinal wake field generated by a point charge moving at the speed of light in a SLAC accelerator structure has been calculated by Wilson and Bane.[10] These

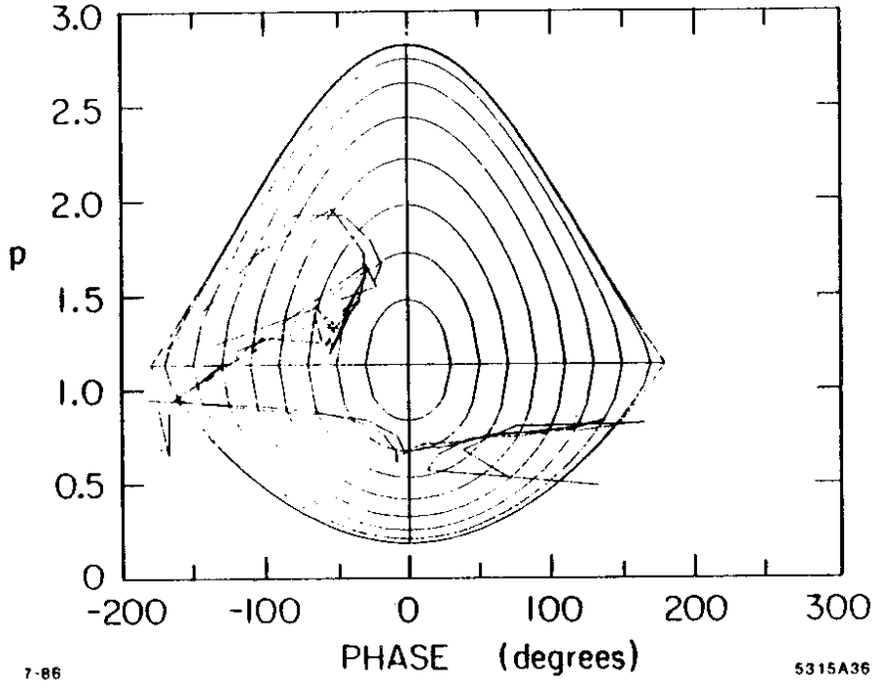

Fig. 2.35. Beam emittance at the entrance to and exit from the S-band buncher superimposed on the buncher low-current phase space orbits, $p_w = 1.134$, $\alpha_2 = .56$.

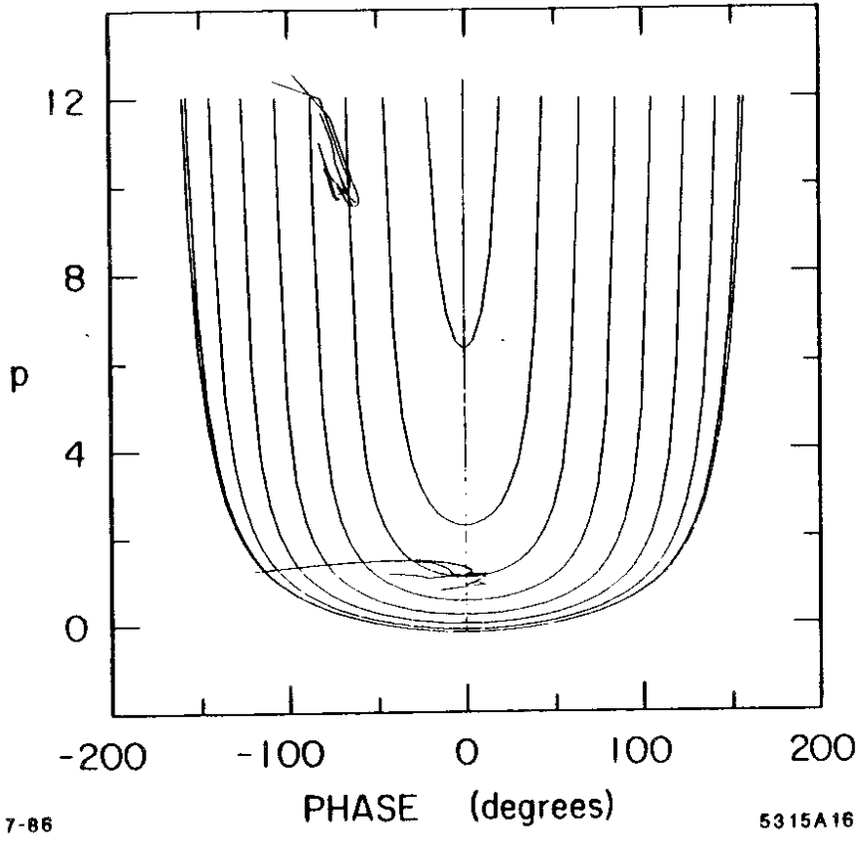

Fig. 2.36. Beam emittance at entrance to capture region and 31.5 cm downstream superimposed on the capture region low-current phase space orbits, $p_w = 1.28$, $\alpha_3 = 2.16$.

fields have been added to the ring-and-disk model program in the velocity of light section. The wake fields are calculated as if all particles were moving at speed c in the capture region and accelerator. This assumption probably overestimates their effect in the capture region, although the total error is small compared to the overall wake field effect. No attempt has been made to model wake field effects in the buncher. More powerful programs such as MASK[11] are required to attack this problem accurately.

Assuming that wake fields primarily affect the energy spectrum of the beam rather than its bunch length, we can learn something from the present model. Figures 2.37-2.39(a) show the final emittance, spectrum and bunch length of the "Table 2.5" injector calculated without longitudinal wake fields. Figures 2.37-2.39(b) show the emittance, spectrum, and bunch length in the presence of wake fields. Note that the spectrum has greatly deteriorated while the bunch length is slightly broadened. The deterioration of the spectrum can be offset by capturing the electron bunch forward of the RF crest, where the slope of the RF is opposite to that of the wake fields. In particular we choose θ_∞ such that

$$\theta_\infty = \arccos \frac{\Delta E/radian}{E_{max}} \quad . \tag{2.56}$$

To choose $\Delta E/E$, we examined Fig. 2.37(b) and found that in the region of highest charge density [1° to 5° as seen in Fig. 2.39(b)] the change in energy per degree $\Delta E/\text{degree} = 3.9$ MeV/degree. Converting to radians and substituting in Eq. 2.56 yields $\theta_\infty = -65°$. Thus we wish to capture the bunch 25° ahead of the RF crest. Equation 2.11 gives

$$\alpha_3(new) = \frac{\alpha_3(old)}{1 - \cos\theta_\infty} = 3.7 \quad . \tag{2.57}$$

Figures 2.37(c), 2.38(c), and 2.39(c), respectively, show the emittance, spectrum and bunch length of the "Table 2.4" injector assuming an accelerator section field strength of $K = 180$ kV/cm. Although the beam is captured 25° ahead of

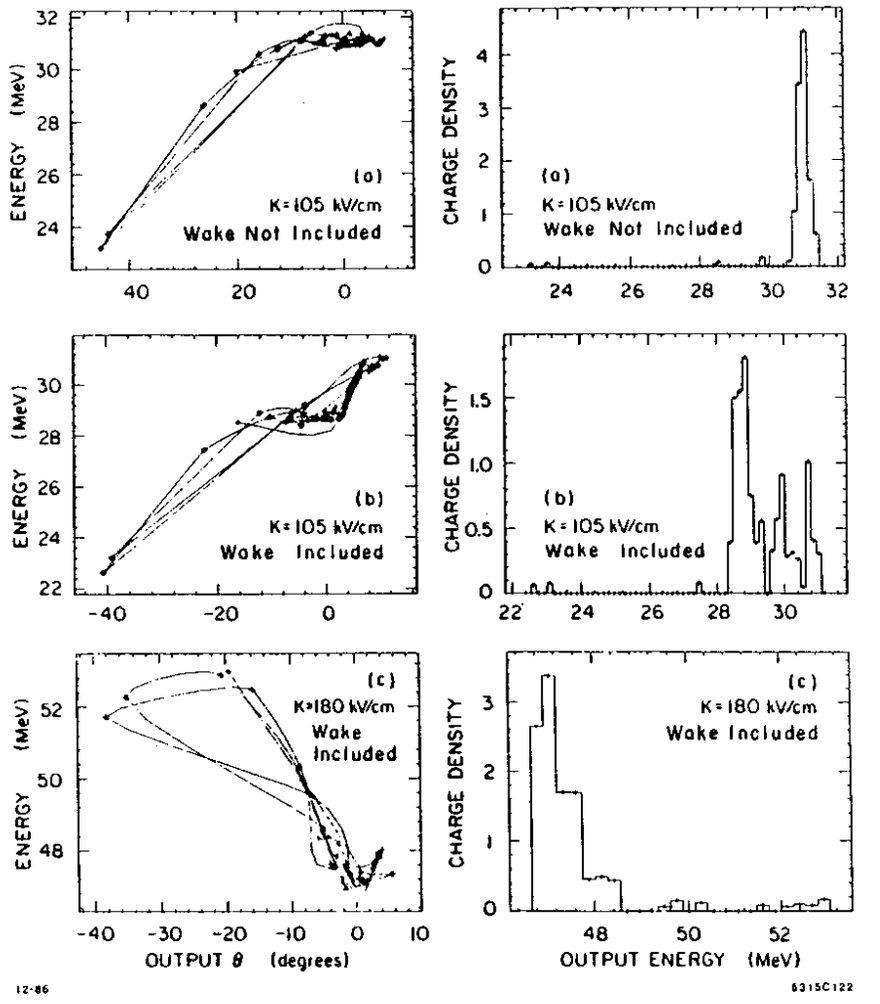

Fig. 2.37. Longitudinal emittance at the end of a three-meter accelerator section with (a) $K = 105$ kV without wakefields calculated, (b) $K = 105$ kV with wakefields calculated, and (c) $K = 180$ kV/cm with wakefields calculated.

Fig. 2.38. Energy spectrum at the end of a three-meter accelerator section with (a) $K = 105$ kV without wakefields calculated, (b) $K = 105$ kV with wakefields calculated, and (c) $K = 180$ kV/cm with wakefields calculated.

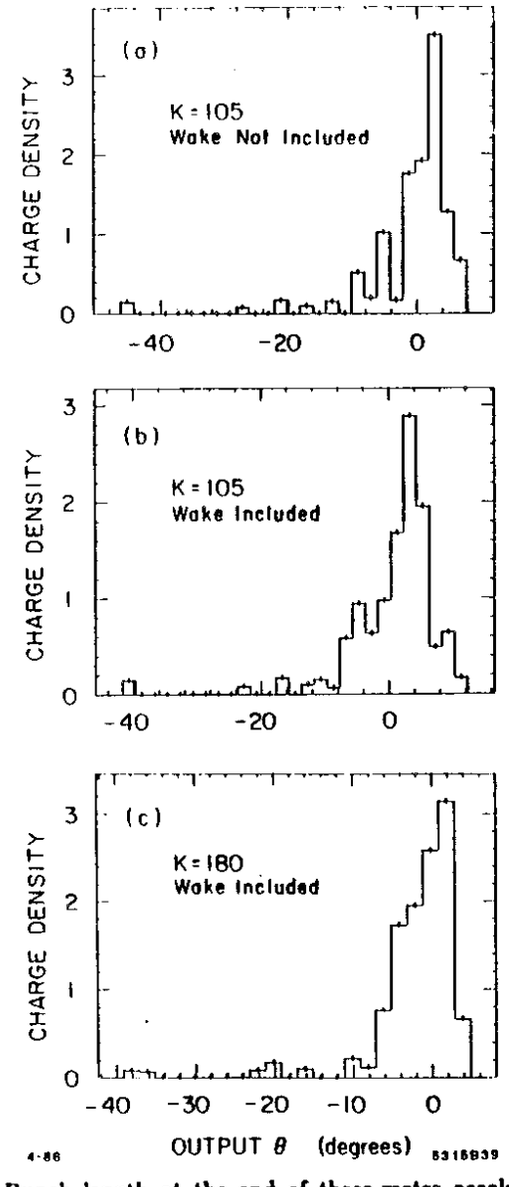

Fig. 2.39. Bunch length at the end of three-meter accelerator section with (a) $K = 105$ kV/cm without wakefields calculated, (b) $K = 105$ kV/cm with wakefields calculated, and (c) $K = 180$ kV/cm with wakefields calculated.

the RF crest, the final energy of the beam is 15 MeV greater than in the $\alpha_3 = 2.16$ case because of the higher accelerating gradient. The spectrum, while not as good as it would be in the absence of wake fields [Fig. 2.38(a)] is greatly improved over the case in which the bunch is captured on the crest in the presence of wake fields.

The computer simulations which include wake field calculations predict that approximately 80% of the charge in the gun pulse is contained within a $\pm 1\%$ spectrum at the end of the three-meter accelerator section. The bunch is slightly better [Fig. 2.39(c)] than in the case where wake fields are not calculated as 7×10^{10} electrons are captured into 14° of S-band phase.

2.2.3 Original Collider Injector Design

As stated earlier, the actual CID design was undertaken without the benefit of hindsight, and therefore does not reflect all the insights discussed in the last two sections. The original design also differs from the current running condition of the CID injector. However, for completeness and continuity we review the actual CID design here. The original CID design differs from the "Table 2.5" injector in one important respect: in the "Table 2.5" injector design, we studied and accommodated the effects due to bunching with the large signals used in the gap-and-drift prebunchers. In the original CID design, we began with the less valid (but simpler) assumption that the voltages in the prebunchers would produce relatively small changes in the kinetic energy of the particles when, in fact, it is changed by as much as 50%. In the small signal approximation, velocity varies linearly with energy

$$\Delta\beta \propto \Delta\gamma \quad . \tag{2.58}$$

With this assumption, perfect bunching is obtained when the gap voltage varies linearly in time.

In the original CID design,[12] we assumed that the gun produces a 15 amp, 1 ns FWHM Gaussian pulse. The frequency of the subharmonic bunchers is not

critical as long as the frequency is low enough that the gun pulse falls in the linear region of one cycle. Choosing a cavity with the highest frequency which meets this condition has an advantage in that less power is required to achieve a given field gradient across the gap. We chose 178.5 MHz, the 16th subharmonic of S-band as the frequency of the first subharmonic buncher gap. The 1.7 ns ($\pm 2\sigma$) gun pulse subtends 110° of phase. At 178.5 MHz the change in the energy of each particle as it crosses the gap is a reasonably linear function of phase (or time) as shown in Fig. 2.42(a).

When bunching with a linear signal, if we try to use a high field gradient and appropriate drift space to match the beam from the first gap-and-drift prebuncher directly into the $\beta_w = .75$ buncher, several problems arise:

1. Asymmetries due to relativistic effects increase,
2. Space charge forces act asymetrically within a set of annuli. ("Hernias" develop.)
3. The disparity between the phase spaces of the inner and outer annuli grows.

All three effects increase the effective emittance. Thus we chose to use two gap-and-drift prebunchers. In the first subharmonic buncher we chose $\alpha = .39$ and $L = 108$ cm which leads to the 600° bunch shown in Fig. 2.43(b). Note [Figs. 2.40(b) and 2.41(b)] that the lower energy particles (positive phases) are converging on center faster than the higher energy (negative phases) due to the relativistic asymmetry. A second subharmonic buncher is needed to match the beam to the buncher acceptance. The frequency of the second gap could easily be as high as the sixth subharmonic of S-band (although the eighth subharmonic should be chosen as it is a harmonic of the 16th), but any frequency below the sixth will suffice.

Computer modeling shows that the field gradients needed in the second gap are not high so that a low power-to-field gradient ratio is not an important criterion. To minimize time and costs in designing and machining the sub-

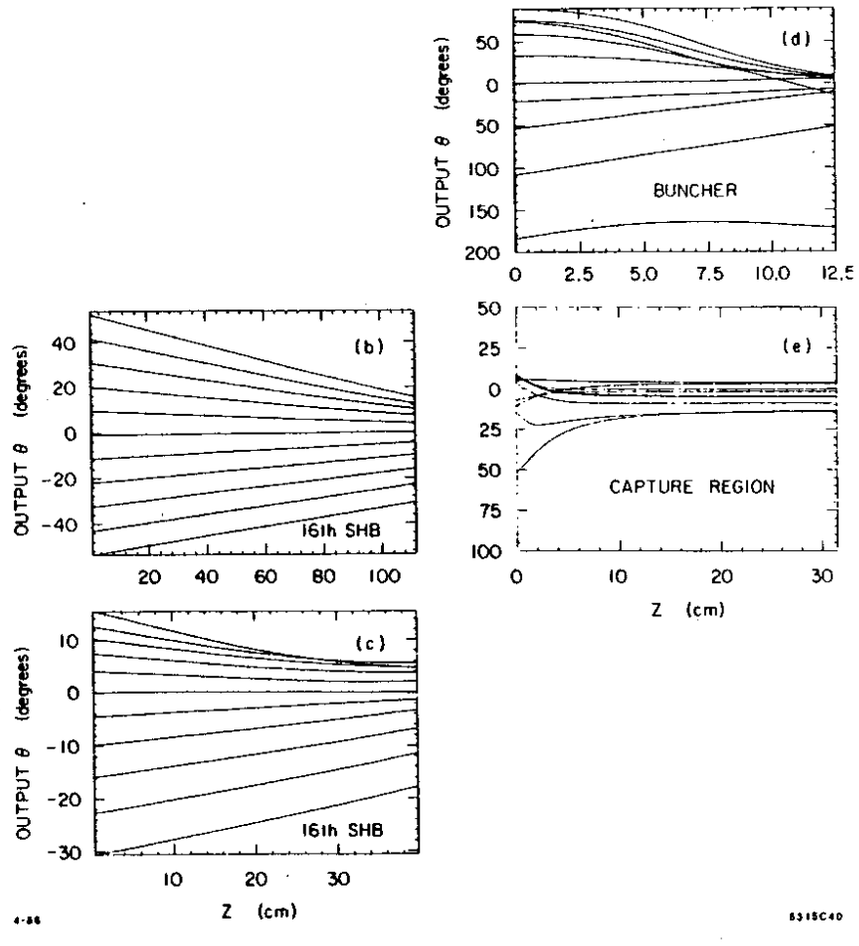

Fig. 2.40. θ versus z for every third of the 31 inner disks of charge traversing the original CID injector design. (b) First 16th subharmonic gap and 108 cm drift, θ given in degrees at the 16th subharmonic of S-band. (c) Second 16th subharmonic gap and 36 cm drift, θ given in degrees at the 16th subharmonic of S-band. (d) 10.5 cm S-band buncher and 2 cm drift, θ given in degrees at S-band. (e) First 30 cm of velocity-of-light accelerator section, θ given in degrees at S-band.

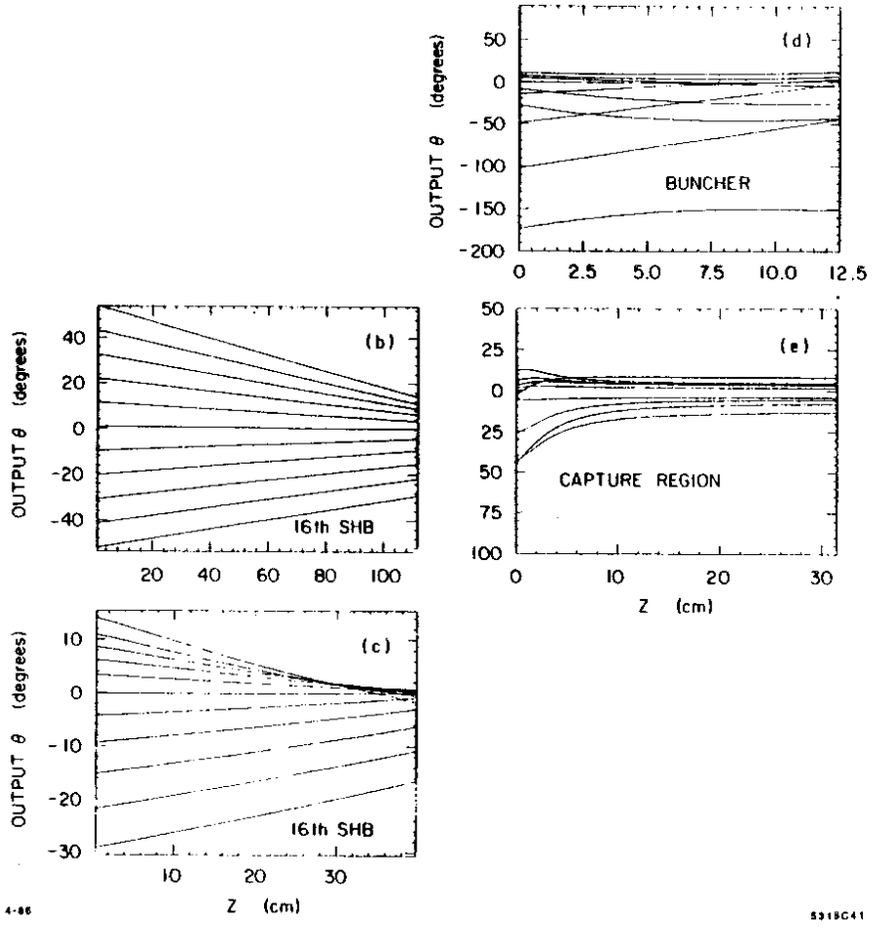

Fig. 2.41. θ versus z for every third of the 31 outer annuli of charge traversing the original CID injector design. (b) First 16th subharmonic gap and 108 cm drift, θ given in degrees at the 16th subharmonic of S-band. (c) Second 16th subharmonic gap and 36 cm drift, θ given in degrees at the 16th subharmonic of S-band. (d) 10.5 cm S-band buncher and 2 cm drift, θ given in degrees at S-band. (e) First 30 cm of velocity-of-light accelerator section, θ given in degrees at S-band.

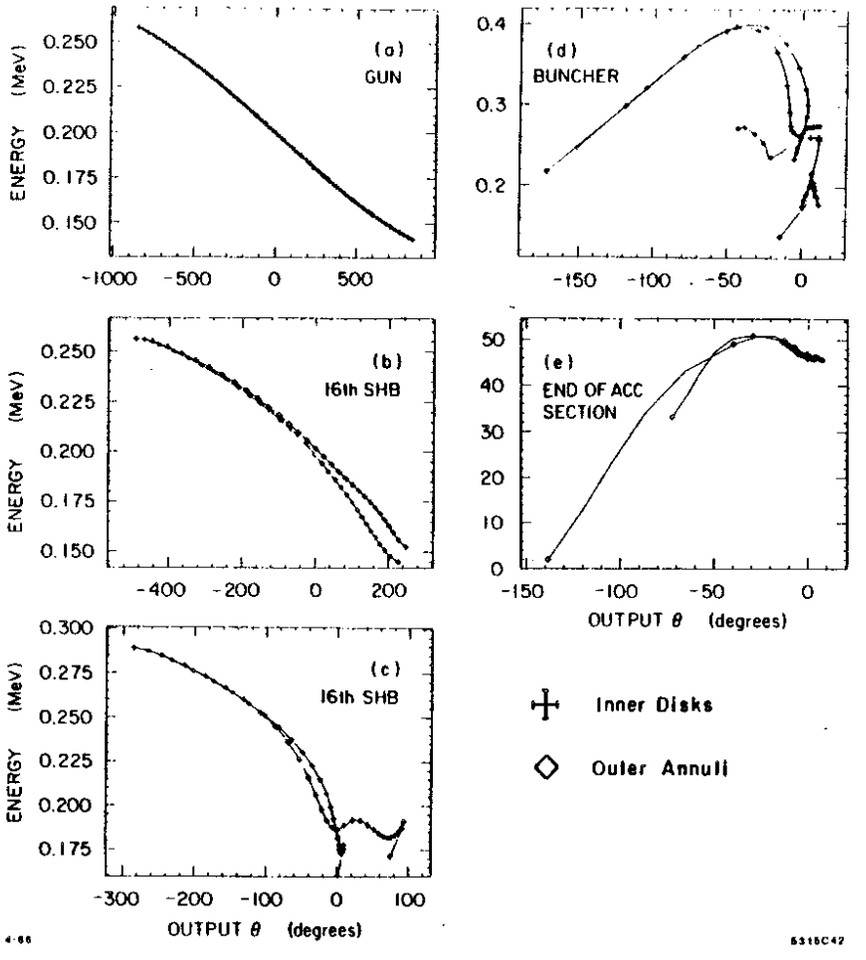

Fig. 2.42. Longitudinal emittance at five locations along the original CID design. (a) Just downstream of first 16th subharmonic gap. (b) End of 108 cm drift. (c) End of 36 cm drift following second 16th subharmonic gap. (d) End of S-band buncher. (e) End of three-meter accelerator section. θ in all figures given in degrees of S-band.

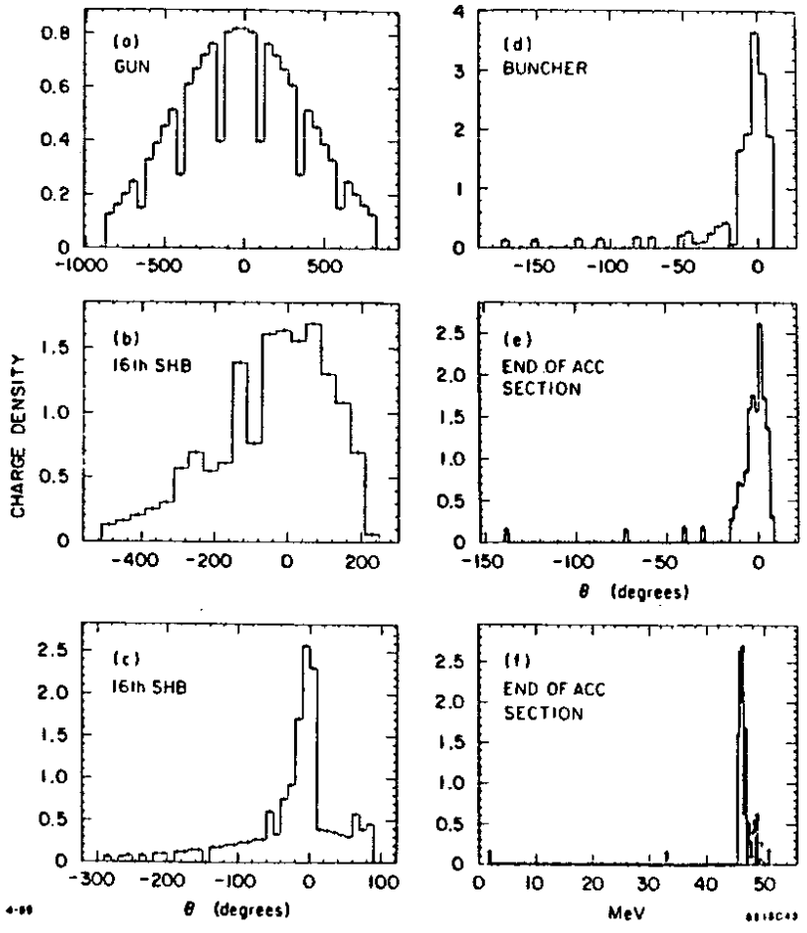

Fig. 2.43. Bunch length at five locations along the original CID design. (a) Just downstream of first 16th subharmonic gap. (b) End of 108 cm drift. (c) End of 36 cm drift following second 16th subharmonic gap. (d) End of S-band buncher. (e) End of three-meter accelerator section. All charge densities are relative. θ in (a)-(e) are given in degrees at S-band. (f) Spectrum at end of three-meter accelerator section.

harmonic bunchers, we chose to build the two cavities at the same frequency. In the second subharmonic buncher we chose $\alpha = .37$ and $L = 36$ cm. Again note [Figs. 2.40(c) and 2.41(c)] that the bunch converges asymmetrically. As we see from Figs. 2.42(c) and 2.43(c) we did not find a good compromise between good bunching of the inner disks and outer annuli. This solution favors the outer annuli which bunch into a 50° peak while the inner disks are spread over some 300°. Clearly the charge in the tail with phases of less than $-100°$ will not be captured by the buncher. In Fig. 2.44 the emittance of the beam [Fig. 2.42(c)] is superimposed on the low current phase space orbits of the buncher.

The beam enters the buncher with a mean momentum equal to the gun pulse momentum since there is no phase shift of the centroid with respect to the RF in the prebuncher. This is a higher momentum than the "Table 2.5" injector. A smaller α_2 is sufficient to transport the beam through a quarter of a cycle in phase space. The beam emittance [Fig. 2.42(c)] has a significant "Lazy L"-like shape. Bunching in the buncher is improved if we shift the centroid of the beam to $-15°$ so that the particles in the "Lazy L" fall between the phase space orbits with asymptotic phases $\theta_m = -50°$ and $\theta_m = -70°$ (see Fig. 2.44). The buncher does a good job as 7.6×10^{10} electrons initially spread over 200° are collected into 25° of S-band phase [see Fig. 2.43(d)]. Another 1×10^{10} electrons are contained in a tail that extends some 30°.

In the velocity-of-light section we chose a high field gradient, $\alpha_3 = 3.7$. The bunch reaches an asymptotic phase of $-70°$, which helps to offset the broadening of the spectrum due to wake fields, although this was not a principal concern at the time of the design. In Fig. 2.45 the emittance of the bunch at the entrance to the accelerator section is plotted on the low current phase space orbits of the capture region. We see that the charge contained in the 30° tail of Fig. 2.43(d) is folded into the core of the bunch during capture; thus 8.5×10^{10} electrons are ultimately captured into a 24° ($\sigma \approx 7°$) bunch [see Fig. 2.43(e)]. This design meets the original specifications as described in Chapter 1.

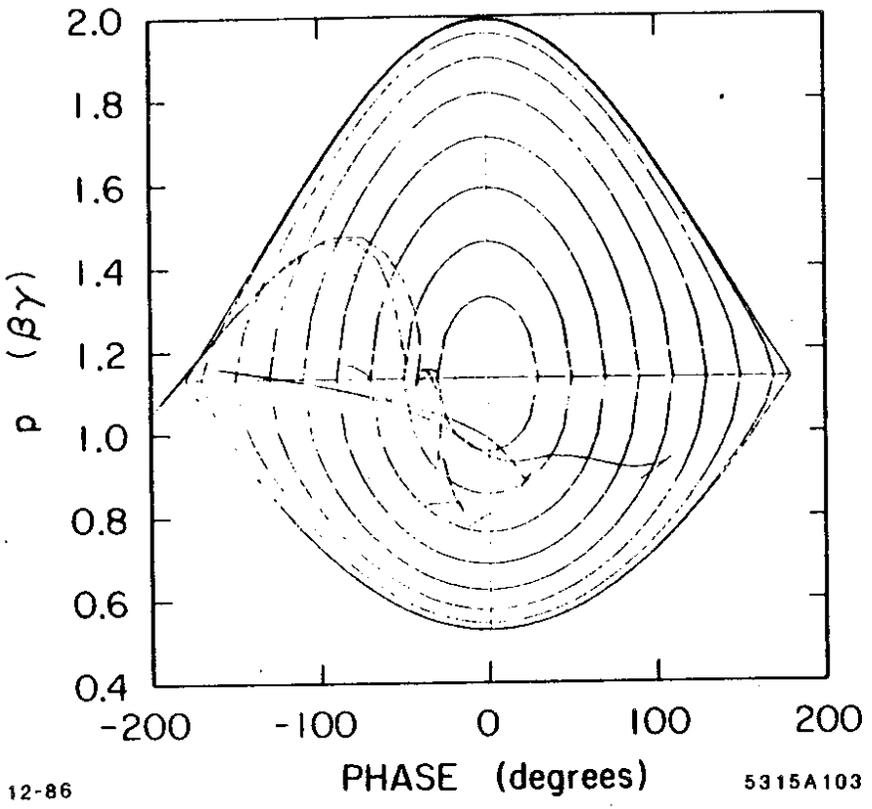

Fig. 2.44. Beam emittance at the entrance to and exit from the S-band buncher superimposed on the low-current buncher phase space orbits of the original CID design.

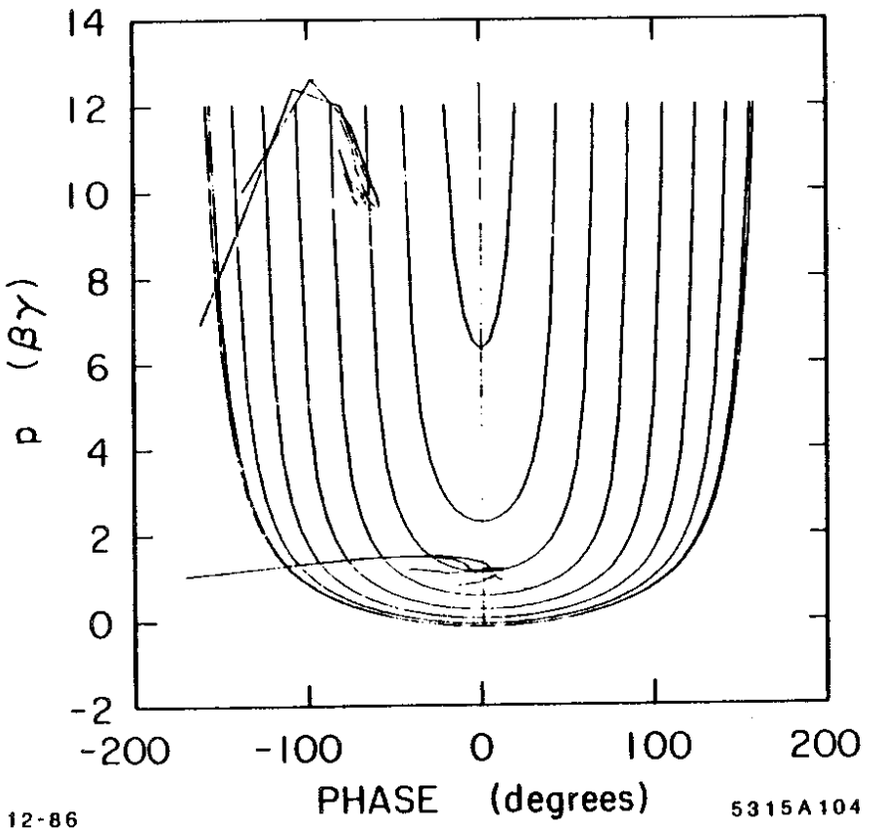

Fig. 2.45. Beam emittance at the entrance of the capture region and 30 cm downstream superimposed on the capture region low current phase space orbits of the original CID design.

2.3. Description of the Ring and Disk Model Computer Code

2.3.1. Description

In order to calculate space charge effects during the bunching process, we model the beam as a finite number of infinitely thin disks and rings of charge in an infinitely long conducting cylinder (see Fig. 2.27).[13,14] The space charge forces between the annuli are found by solving for the average static force between annuli in the presence of the grounded conducting cylinder.

The potential of an infinitesimal surface charge located at $r = b$, $\Theta = \phi$, and $z = 0$ in an infinite conducting cylinder of radius a is[15]

$$\psi_{pt}(r, \Theta, z) = \frac{\rho ds}{\pi \epsilon_0 a} \sum_{m=0}^{\infty} \sum_{n=1}^{\infty} \left\{ \frac{1}{1+\delta_{m0}} \left[\frac{J_m[(j_{mn}/a)b] J_n[(j_{mn}/a)r]}{[j_{mn} J_{m+1}(j_{mn})]^2} \right] \times \exp\left(-j_{mn} \frac{|z|}{a} \right) \cos(\Theta - \phi) \right\} \tag{2.59}$$

where

J_m = the m^{th} Bessel function
j_{mn} = n^{th} zero of m^{th} Bessel function
ρds = charge density on infinitesimal surface element $ds = b\,db\,d\phi$
r = magnitude of the radial component in cylindrical coordinates
Θ = magnitude of the azimuthal component in cylindrical coordinates
z = longitudinal position
ϵ_0 = dielectric constant in MKS units
δ_{m0} = 1 for $m = 0$, = 0 for $m \neq 0$

The potential of an annulus of charge with inner radius b_1 and outer radius b_2 is

$$\psi(r, \Theta, z) = \int_{b_1}^{b_2} \int_{0}^{2\pi} \psi_{pt}(r, \Theta, z; b, \phi) b\,db\,d\phi \tag{2.60}$$

The longitudinal electric field is found by differentiating the potential

$$E_z(r, \Theta, z) = -\frac{\partial \psi(r, \Theta, z)}{\partial z} = -\frac{\partial}{\partial z} \int_{b_1}^{b_2} \int_{0}^{2\pi} \psi_{pt}(r, \Theta, z; b, \phi) b\,db\,d\phi \quad . \tag{2.61}$$

Given a second annulus of charge located at z, with inner radius r_1 and outer radius r_2, the average longitudinal field on the second annulus due to the first is

$$\overline{E}_{21} = \frac{\int_{r_1}^{r_2} \int_0^{2\pi} E_z(r, \Theta, z) r\,dr\,d\Theta}{\int_{r_1}^{r_2} \int_0^{2\pi} r\,dr\,d\Theta} = \frac{\int_{r_1}^{r_2} \int_0^{2\pi} \int_{b_1}^{b_2} \int_0^{2\pi} \left\{ -\frac{\partial}{\partial z} \psi_{pt}(r, \Theta, z; b, \phi) \right\} b\,db\,d\phi\,r\,dr\,d\Theta}{\pi \left[(r_2)^2 - (r_1)^2 \right]} \quad . \tag{2.62}$$

The change in the energy of the second disk or annulus due to this average field is

$$\frac{d\gamma_2}{dz} = \frac{e}{m_0 c^2} \overline{E}_{21} \quad . \tag{2.63}$$

The variable z in the exponent of Eq. (2.59) represents the distance between the two annuli. If we measure the position of each disk by its phase relative to the RF accelerating wave with $\lambda f = c$, the approximate distance between the annuli in the lab frame is

$$z \cong v_1 \frac{\lambda}{c} \frac{\theta_2 - \theta_1}{2\pi} = \beta_1 \lambda \frac{\theta_2 - \theta_1}{2\pi} \tag{2.64}$$

where

θ_1 = phase of annulus 1 with respect to the RF wave
θ_2 = phase of annulus 2 with respect to the RF wave
β_1 = normalized velocity of annulus 1 in the laboratory frame.

Since we are calculating the force on the second annulus, we must write this distance in its reference frame

$$z = \gamma_2\beta_1\frac{\theta_2 - \theta_1}{2\pi}\lambda \quad . \tag{2.65}$$

Performing the integration in Eq. (2.62) and summing over all other annuli, we find that the change in energy of the m^{th} annulus due to all other annuli is

$$\begin{aligned}\frac{d\gamma_m}{dz} = &\frac{2e}{\epsilon_0 m_0 c^2}\,\frac{1}{\pi(r_{m2}^2 - r_{m1}^2)}\sum_{n=1}^{\infty}\sum_{\substack{j=1\\ j\neq m}}^{NA} Q_j \\ &\left\{\frac{r_{m2}J_1[j_{0n}(r_{m2}/a)] - r_{m1}J_1[j_{0n}(r_{m1}/a)]}{(r_{j2}^2 - r_{j1}^2)}\right. \\ &\times\frac{r_{j2}J_1[j_{0n}(r_{j2}/a)] - r_{j1}J_1[j_{0n}(r_{j1}/a)]}{[j_{0n}J_1(j_{0n})]^2} \\ &\left.\times\exp\left(-\left|\frac{j_{0n}}{a}\gamma_m\beta_j\left(\frac{\theta_m - \theta_j}{2\pi}\right)\lambda\right|\right)\right\}\end{aligned} \tag{2.66}$$

where

n	=	index for sum over zeros of J_0
j	=	index for sum over all other annuli
Q_j	=	total charge on the j^{th} annuli
NA	=	total number of disks and annuli
r_{j1}	=	inner radius of j^{th} annulus
r_{j2}	=	outer radius of j^{th} annulus.

For an initially Gaussian charge distribution, the charge on each annulus is given by

$$Q_j = Q_0\exp-\left(\frac{t_j^2}{2\sigma^2}\right) \quad .$$

where

Q_0	=	total charge on the annulus which leaves the gun at the center of the Gaussian pulse
t_j	=	the time at which the j^{th} annuli leaves the gun with respect to the center particle
σ	=	sigma of the Gaussian distribution.

The longitudinal equations of motion for the m^{th} annulus (Eqs. 2.4 and 2.5) in the presence of space charge are

$$\begin{aligned}\frac{d\gamma_m}{d\xi} = &-\alpha\sin\theta + \frac{2\lambda e}{\epsilon_0 m_0 c}\,\frac{Q_0}{\pi(r_{m2}^2 - r_{m1}^2)}\sum_{\substack{j=1\\ j\neq m}}^{NA}\exp-\left(\frac{t_j^2}{2\sigma^2}\right)\sum_{n=1}^{\infty} \\ &\times\left\{\frac{r_{m2}J_1[j_{0n}(r_{m2}/2)] - r_{m1}J_1[j_{0n}(r_{m1}/a)]}{r_{j2}^2 - r_{j1}^2}\right. \\ &\times\frac{r_{j2}J_1[j_{0n}(r_{j2}/a)] - r_{j1}J_1[j_{on}(r_{j1}/a)]}{[j_{0n}J_1(j_{0n})]^2} \\ &\left.\times\exp\left[-\left|\frac{j_{0n}}{a}\gamma_m\beta_j\left(\frac{\theta_m - \theta_j}{2\pi}\right)\lambda\right|\right]\right\}\end{aligned} \tag{2.67}$$

and

$$\frac{d\theta_m}{d\xi} = 2\pi\left(\frac{1}{\beta_w} - \frac{1}{\beta_m}\right) \tag{2.68}$$

2.3.2 Use of the RINGMODEL Computer Program

The program RINGMODEL integrates Eq. (2.67) and (2.68) as the bunch moves from the gun through the subharmonic bunchers, the S-band buncher, and the three-meter accelerator section. While this approach to modeling space charge effects in bunching systems is very useful, it has a number of limitations

which users must keep in mind. The program calculates the **static** forces between infinitely thin disks of charge in a **smooth** conducting cylinder. Each of the boldface adjectives presents limitations:

1. The program calculates static forces between particles. This is a good approximation of the forces between particles as long as the energy spread within the bunch is a small fraction of the total energy. In this case it is reasonable to speak of the "rest frame" of the electron bunch. If $\Delta E/E$ is large (as it is in the subharmonic and S-band buncher buncher regions), there is no reasonable rest frame of the bunch. Note that in Fig. 3.10 (Sec. 3.2) at the output of the S-band buncher, the momentum of particles in the bunch ranges from .7 to 1.9 m_0c. In such a case an electrostatic calculation cannot provide a good model of the intrabunch forces, and a fully electromagnetic calculation is required. An example of an effect that depends on the magnetic fields is the back EMF produced as the beam current is "turned on" at the front of the bunch and "turned off" at the rear of the bunch (see Fig. 2.46). The back EMF opposes the spreading due to space charge. This effect is clearly important in Herrmannsfeldt's lasertron simulation.[16]

2. The program calculates the average Coulomb forces between a relatively small number of infinitely thin disks and annuli. Very near the surface of the disk [i.e., as z approaches zero in Eq. (2.59)], the fields due to the disk approach those of an infinite sheet of charge,

$$E_z \underset{z\to 0}{=} \frac{\rho}{2\epsilon_0} \quad . \tag{2.70}$$

If the charge were represented by thousands of particles (as in the MASK program), we would expect that the field due to a thin "slice" of charge would go to zero at the center of the slice. Thus the infinitely thin disk approximation may overestimate space charge forces as disks pass each other. In Figs. 2.29(e) and 2.33(b) we see that large momentum changes

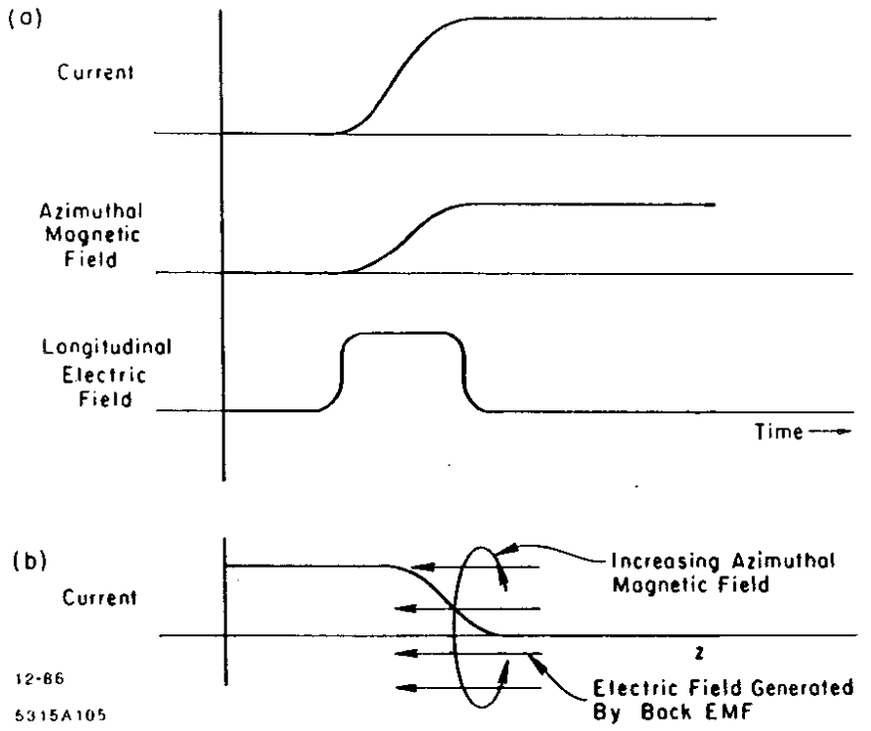

Fig. 2.46. Fields as a "trapezoid" of charge passes a given point z. (a) As the current increases a growing azimuthal magnetic field produces increasing flux lines in the $\hat{z}$ direction. These growing flux lines are opposed by a back EMF which results in an electric field in the $-\hat{z}$ direction. (b) Fields induced at the front of the bunch oppose space charge spreading (note that the absyssal axis is z).

occur as the disks interact at close distances. These "hernias" in phase space may be an artifact of this model, due in part to our calculation of E_z near a disk.

3. The model calculates space charge forces in a smooth conducting cylinder. This is an adequate model in the subharmonic buncher region where single short accelerating gaps are followed by long drift spaces. Clearly a smooth conducting cylinder is a great oversimplification of the boundaries in the disk-loaded waveguide which makes up the buncher and accelerator sections. We choose to model the system as though a smooth conducting cylinder were located at the inner radius of the waveguide, and the space charge forces are calculated accordingly. Wakefield effects at the subharmonic buncher gaps and in the buncher have been neglected. Since momentum spread early in the system is important in determining the final bunch length, these effects may be important. Further modeling with MASK is needed to clarify this issue. In the velocity-of-light section the wakefields are calculated as though all particles were moving at speed c. As shown in Figs. 2.39(a) and (b), the wake fields cause a 10 to 15% change in bunch length.

4. The most important limitation of this model is that it is a one-dimensional model; no attempt is made to model radial motion, which is clearly coupled to longitudinal motion. In RINGMODEL we assume that the radii of the disks and annuli remain constant throughout a given bunching element. The radii of the annuli are calculated by assuming that radial Coulomb repulsion is offset by focusing due to the self-magnetic field of the beam and external solenoidal focusing. This calculation is described in detail in the next section.

The advantages of RINGMODEL are threefold: it is easy to use, it is fast to run, and most importantly it was written and usable when CID was designed. A designer can make many runs in a day, varying field strengths, phase shifts,

drift lengths, and other parameters. A program of this kind is certainly useful for getting an injector design underway, i.e., getting a "feel" for the problem at hand. In the future a program like RINGMODEL is best used in conjunction with a more powerful (but more cumbersome) program like MASK. RINGMODEL could be used to get a handle on the problem, while MASK is used for final confirmation of a reasonable design.

2.4. RADIAL DYNAMICS

As mentioned in Section 2.3, the longitudinal dynamics of the beam have been modeled assuming that the beam radius is constant throughout a given bunching region. Clearly, longitudinal space charge forces are minimized if we choose as large a beam radius as can be transported through the beam pipe. In the subharmonic buncher drift spaces we choose large diameter beam pipe (3.5 cm I.D.) and allow the beam to fill the pipe to minimize space charge effects. In the higher power traveling wave structures a large beam radius leads to large radial emittance growth as discussed in detail below. Therefore, beam radius in the buncher and capture region must be chosen to allow longitudinal bunching while keeping the radial emittance within specifications.

2.4.1. Radial Emittance Growth

Figure 2.47(a) is a schematic diagram of the electric and magnetic fields of the TM fundamental mode in a smooth conducting cylinder. Arrows within the structure indicate the direction of lines of force on an electron. Electrons near point A experience forces due to three components of the field:

1. The longitudinal electric field, E_z, focuses the electrons toward point A. This point is stable longitudinally.
2. The radial electric field, E_r exerts a defocusing force on the electrons.
3. The azimuthal magnetic field, B_ϕ, exerts a radially focusing force on the electrons.

As we shall show directly, this force is weaker than the radial defocusing when β or β_p is less than unity. Hence point A is radially unstable. In the case of $\beta = \beta_p = 1$ the two radial forces cancel. In analogous fashion we find that point B is unstable longitudinally and stable radially.

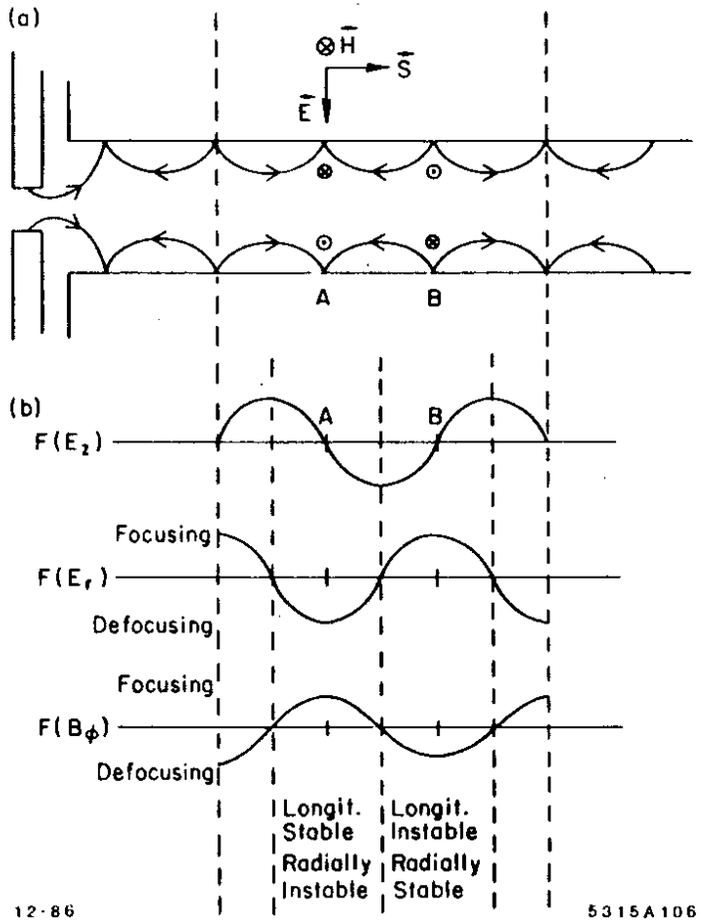

Fig. 2.47. (a) Lines of force on electron in smooth conducting cylinder excited in the TM mode. (b) Forces on electron due to E_z, E_r and B_ϕ.

Figure 2.47(b) is a schematic representation of the effect of the three force components on the electrons. Note that in Region A, the region of greatest longitudinal bunching, the radial defocusing fields are at their maximum values. The gradient of the amplitude of the radial fields is a slowly varying function in this region and thus all electrons in the linear region of the longitudinal field see essentially equal radial forces.

Radial emittance growth is not caused primarily by the difference in the amplitude of radial fields seen by particles, but by the fact that particles initially at positive longitudinal phases feel the radial forces for a longer time. Consider particles 1 and 2 in Fig. 2.48. Both particles have the same phase at the end of the structure (i.e., both particles move to point 3). But particle 2 spends more time in the structure and thus receives a larger radial momentum kick.

We now discuss a quantitative estimate of radial emittance growth in the CID injector.

As discussed in Ref. 17, the longitudinal electric field in the TM mode in a cylindrical conductor is given by the real part of

$$E_z = iE_0(z)\,J_0(k_r r)\exp[i(\omega t - k_z z)] \tag{2.71}$$

where

$$k_r^2 + k_z^2 = k^2 = \left(\frac{2\pi}{\lambda}\right)^2 \tag{2.72}$$

and λ is the free space wavelength of the wave. From Gauss' theorem we find

$$E_r = -\frac{1}{k_r}\left(k_z E_0 + i\frac{\partial E_0}{\partial z}\right) J_1(k_r r)\exp[i(\omega t - k_z z)] \quad . \tag{2.73}$$

From $\vec{\nabla} \times \vec{B} = 1/c\,\partial\vec{E}/\partial t$ (c.g.s. units)we find

$$B_\phi = -\frac{1}{k_r}\frac{\omega}{c} E_0 J_1(k_r r)\exp[i(\omega t - k_z z)] \quad . \tag{2.74}$$

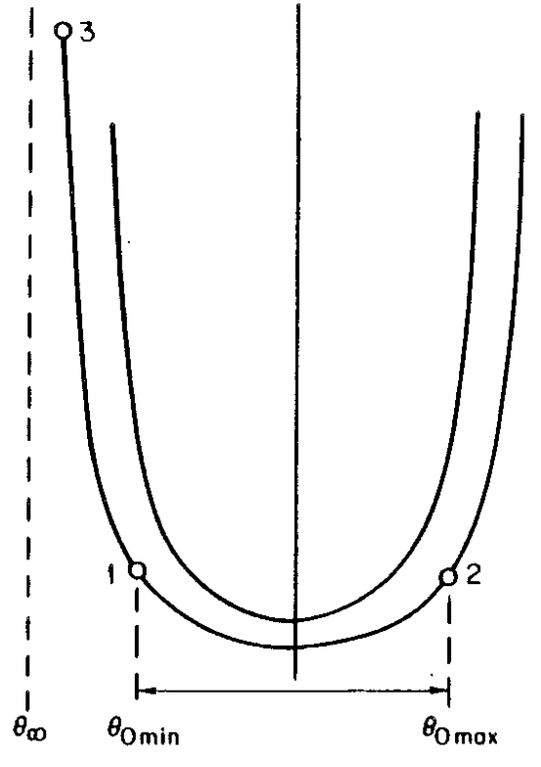

Fig. 2.48. Particles with the same θ_∞ but with different Δp_r at the end of capture region.

For small values of r, we can approximate

$$J_0(k_r r) \approx 1 \qquad \text{and} \qquad J_1(k_r r) \approx \frac{1}{2} k_r r \quad . \tag{2.75}$$

Thus

$$E_z \cong i E_0(z) \exp[i(\omega t - k_z z)] \quad , \tag{2.76}$$

$$E_r \cong -\left(k_z E_0 + i \frac{\partial E_0}{\partial z}\right) \frac{r}{2} \exp[i(\omega t - k_z z)] \tag{2.77}$$

and

$$B_\phi \cong -\frac{\omega}{c} E_0 \frac{r}{2} \exp[i(\omega t - k_z z)] \quad . \tag{2.78}$$

In regions where $\frac{\partial E_0}{\partial z} \cong 0$ (i.e., away from the fringing fields at the beginning and end of the structure)

$$\frac{\partial E_z}{\partial z} \cong k_z E_0 \exp[i(\omega t - k_z z)]$$

and

$$E_r \cong -k_z E_0 \frac{r}{2} \exp[i(\omega t - k_z z)] \quad .$$

Thus

$$E_r \cong -\frac{r}{2} \frac{\partial E_z}{\partial z} \quad . \tag{2.79}$$

We see that the radial fields are largest (and defocusing) when the longitudinal fields have the most gradient, i.e., at the phase stable longitudinal field null.

To calculate the emittance growth due to the radial fields, we must find the change in radial momentum due to the radial force on a particle in the electric

and magnetic field. The Lorentz force law gives

$$F = \frac{d\vec{p}}{dt} = e\left(\vec{E} + \frac{1}{c}\vec{v} \times \vec{B}\right) \quad . \tag{2.80}$$

The radial component of the normalized force is

$$\frac{dp_r}{dt} = \frac{e}{m_0 c}\left(E_r + \beta_\phi B_z - \beta_z B_\phi\right) \tag{2.81}$$

where p_r is the normalized radial momentum $= \gamma\beta_r$. In the TM_{01} mode under consideration, $B_z = 0$ and the change in the radial momentum as a function of z is given by

$$\frac{dp_r}{dz} = \frac{e}{\beta m_0 c^2}\left(E_r + \beta B_\phi\right) \qquad \text{where} \qquad \beta = \beta_z$$

Setting $\theta = \omega t - k_z z$ and taking the real parts of Eqs. (2.73) and (2.74) we obtain

$$\frac{dp_r}{dz} = \frac{eE_0 J_1(k_r r)}{k_r m_0 c^2}\left\{k\left(\frac{1}{\beta\beta_w} - 1\right)\cos\theta + \frac{1}{\beta}\frac{1}{E_0}\frac{\partial E_0}{\partial z}\sin\theta\right\} \quad ,$$

where $\beta_w = (k/k_z)$. For small r

$$\frac{dp_r}{dz} \cong \frac{eE_0 r}{2m_0 c^2}\left\{k\left(\frac{1}{\beta\beta_w} - 1\right)\cos\theta + \frac{1}{\beta}\frac{1}{E_0}\frac{\partial E_0}{\partial z}\sin\theta\right\} \quad . \tag{2.82}$$

The first term of Eq. (2.82) is due to radial electric fields inside the structure, the second term is due to azimuthal magnetic fields and the final term is due to fringe fields at the ends of the structure. From Eq. (2.82) we see that radial momentum growth is a function both of radius and phase. It is the functional dependence on phase that gives rise to radial emittance growth. If Eq. (2.82) were independent of θ, we could offset the linear radial force with solenoidal focusing.

In the general case, Eq. (2.82) is not integrable by simple analytic techniques. A detailed analysis of radial emittance growth requires computer modeling. We thus set ourselves the more modest goal of studying Eq. (2.82) in a special case

which leads to an integrable form. This special case at least allows us to know the order of magnitude of radial emittance growth and subsequent limitations on longitudinal bunching. In the case where the phase velocity of the structure, β_p, is equal to unity, the $\cos\theta$ term of Eq. (2.82) becomes

$$k\left(\frac{1}{\beta}-1\right)\cos\theta = -\frac{d\theta}{dz}\cos\theta \tag{2.83}$$

as given in Eq. (2.5), and Eq. (2.82) becomes

$$\frac{dp_r}{dz} = \frac{eE_0 r}{2m_0c^2}\left[-\frac{d\theta}{dz}\cos\theta + \frac{1}{\beta E_0}\frac{\partial E_0}{\partial z}\sin\theta\right] \quad . \tag{2.84}$$

The first term of Eq. (2.84) becomes negligible as $\theta \rightarrow -90°$; that is, the first term contributes to transverse emittance growth only in the capture region. The second term contributes only in regions of appreciable fringing fields.

Assuming $r \approx r_0$ and integrating to arbitrary z beyond the capture region

$$\int_0^z \frac{dp_r}{dz}dz = \frac{er_0}{2m_0c^2}\left\{-\int_0^z E_0\frac{d\sin\theta}{dz}dz + \int_0^z \frac{1}{\beta}\frac{\partial E_0}{dz}\sin\theta dz\right\} \quad .$$

Assuming that $E_0(z)$ is slowly varying over most of the capture region and that $\sin\theta \approx \sin\theta_0$ and $\beta \approx \beta_{in}$ in the region where $\partial E_0/\partial z$ is non-negligible, we have

$$\int_0^z \frac{dp_r}{dz}dz = \frac{er_0}{2mc^2}\left\{-E_0\int_0^z \frac{d\sin\theta}{dz}dz + \frac{1}{\beta_{in}}\sin\theta_0\int_0^z \frac{\partial E_0}{\partial z}dz\right\} \tag{2.85}$$

integrating we have

$$\Delta p_r \cong \frac{er_0}{2m_0c^2}\left\{E_0(\sin\theta_0 - \sin\theta_\infty) + \frac{1}{\beta_{in}}\sin\theta_0 E_0\right\}$$

or rearranging terms

$$\Delta p_r \cong \frac{er_0E_0}{2m_0c^2}\left[\left(1+\frac{1}{\beta_{in}}\right)\sin\theta_0 - \sin\theta_\infty\right] \tag{2.86}$$

where β_{in} = normalized velocity of the particles as they enter the capture region.

Radial emittance growth results from a difference in the total radial momentum kick for particles which enter at different phases. We are concerned with the variation of Δp_r as initial longitudinal phase, θ_0, changes:

$$\frac{d\Delta p_r}{d\theta_0} = \frac{eE_0r_0}{2m_0c^2}\left\{\left(1+\frac{1}{\beta_{in}}\right)\cos\theta_0 - \frac{\sin\theta_0}{\sin\theta_\infty}\cos\theta_\infty\right\} \quad . \tag{2.87}$$

From Eq. (2.87) we see that radial emittance growth in the capture region is minimized if

1. We choose to make the beam radius, r_0, as small as possible.
2. We choose a low field strength, E_0, in the capture region.
3. If we capture the bunch on the RF crest, $\cos\theta_\infty \cong 0$ and the second term in Eq. (2.87) is neglibible. To minimize the first term, we should choose θ_0 away from the longitudinal field null, which results in a smaller value of $\cos\theta_0$.

Conditions 1, 2, and 3 all lead to poorer longitudinal bunching.

Thus our bunching technique allows for greater longitudinal bunching only at the expense of radial emittance growth. We can estimate the amount of radial emittance growth in the CID accelerator capture region. From Fig. 3.9(d) (in Sec. 3.2), we estimate that the CID bunch subtends some 60° at the entrance to the accelerator structure. If one assumes capture in the vicinity of the crest, the second term in Eq. (2.87) is quite small. Assuming $\beta_0 = \beta_{in} = .75$, $eE = 170$ KV/cm, and $r_0 = .25$ cm (see Sections 2.4.2 and 3.2), the spread in radial momentum is

$$\begin{aligned}\delta\Delta p_r &= \int_{\theta_0 min}^{\theta_0 max} \frac{d\Delta p_r(\theta_0)}{d\theta_0}d\theta_0 \\ &= \frac{eE_0r_0}{2m_0c^2}\left(1+\frac{1}{\beta_{in}}\right)[\sin 30° - \sin(-30°)] = .40 \quad .\end{aligned} \tag{2.88}$$

The radial emittance ϵ_r is given by $r\delta\Delta p_r$;

$$\epsilon_r(\text{estimate}) = 2.5 \times 10^{-4} \text{ radian meter} \quad . \tag{2.89}$$

As discussed later in Section 3.3, the CID emittance has been measured. For 5×10^{10} electrons captured, the measured emittance is

$$\epsilon_r(\text{measured}) = 1.5 \times 10^{-4} \text{ radian meter (invariant)} \quad . \tag{2.90}$$

We see that our estimated emittance is pessimistic, but is of the correct order of magnitude.

The assumptions necessary to get an analytic solution to Eq. (2.82) are not unreasonable in the capture region, but do not really apply to the buncher region (where $\beta_w = .75$). However, the phase space orbits of the particles in the buncher are quanlitatively quite similar to their orbits in the capture region, and we can look to Eq. (2.87) to suggest trends in the buncher. The fields in the buncher are lower by a factor of 4 to 8, but the initial bunch length is larger by a factor of three, which means that $[\sin\theta_0 - \sin(-\theta_0)]$ is larger by a factor of two, and we would expect the buncher contribution to radial emittance growth to be smaller than that of the capture region by a factor of two or more; at lower field strengths it may even be negligible as compared to the capture region.

One more point is worth noting. We estimate that the radial emittance at the CID gun is approximately

$$\epsilon_{GUN} = 3 \times 10^{-5} \text{ radian meters} \quad .$$

One sometimes reads that the radial emittance grows "by a factor of x" due to RF fields in bunching and capture regions. This is misleading in the sense that the RF fields would cause the same amount of radial emittance growth even if the radial emittance at the gun were negligible. Saying that the emittance "grows by a factor of x" might lead one to think that emittance growth due to RF can be lessened by a lower gun emittance, which is not the case.

2.4.2 Radial Focusing

Radial acceleration in the presence of a solenoidal magnetic field is given by

$$\gamma m_0 \ddot{r} = \gamma m_0 r \dot{\phi}^2 + \frac{e}{c} r \dot{\phi} B_z + \frac{2e\rho_\ell}{r} - e\frac{2I}{rc}\beta \tag{2.91}$$

where

ρ_ℓ = charge/unit length = $I/\beta c$

I = beam current.

The first term in Eq. (2.91) is due to the accelerating coordinate system. The second term is the focusing force due to the external longitudinal magnetic field, the third is the defocusing force due to space charge and the last is the focusing force of the self-magnetic field of the beam. The azimuthal velocity of the beam $\dot{\phi}$ can be obtained by considering the rate of change of angular momentum as electrons pass from the cathode to the interior of the solenoidal magnetic field.[17] The rate of change of angular momentum is given by

$$\begin{aligned} \frac{d}{dt}(\gamma m_0 r^2 \dot{\phi}) = r F_\phi &= r\left(\frac{e}{c}\vec{v} \times \vec{B}\right)_\phi \\ &= r\frac{e}{c}[-r B_z + \dot{z} B_r] \quad . \end{aligned} \tag{2.92}$$

Multiplying by $2\pi dt$ we have

$$2\pi d(\gamma m_0 r^2 \dot{\phi}) = -\frac{e}{c}[2\pi r(B_z dr - B_r dz)] \quad . \tag{2.93}$$

Upon examining Fig. 2.49 we see that the magnetic flux through the beam boundary is given by

$$d\psi = \vec{B} \cdot d\vec{a} = \vec{B} \cdot \left(\frac{dz}{ds}\hat{r} + \frac{dr}{ds}\hat{z}\right) ds r d\phi \tag{2.94}$$

where ds is an infinitesimal perpendicular to $d\phi$ along the beam envelope.

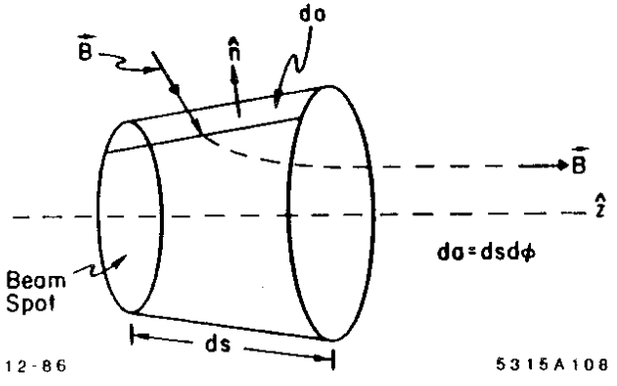

Fig. 2.49. Magnetic flux through the beam boundary.

The flux through a small band of the boundary is found by integrating over $d\phi$

$$d\psi = 2\pi r(B_z dr - B_r dz) \quad . \tag{2.95}$$

Equating (2.93) and (2.95) and integrating we have

$$\int d(\gamma m_0 r^2 \dot{\phi}) = -\frac{e}{2\pi c}\int d\psi \quad . \tag{2.96}$$

We define ψ_c as the magnetic flux through the beam spot at the cathode and assume that the electrons have no azimuthal velocity leaving the cathode.

Equation (2.96) yields

$$\dot{\phi} = -\frac{e}{2\pi\gamma m_0 c r^2}(\psi - \psi_c) \tag{2.97}$$

Thus the azimuthal velocity of the beam is proportional to the total change in flux across the beam surface. Inside the solenoid where the field is uniform in the $\hat{z}$ direction, $\psi = \pi r^2 B_z$. With a little manipulation Eq. (2.91) becomes

$$\ddot{r} = -r\left(\frac{eB_z}{2\gamma m_0 c}\right)^2\left[1 - \left(\frac{\psi_c}{\psi}\right)^2\right] + \frac{2eI}{\gamma m_0 c r}\left[\frac{1}{\beta} - \beta\right] \quad . \tag{2.98}$$

From Eq. (2.98) we see that the flux at the cathode must be less than the flux inside the solenoid for any net focusing to occur. For the common case of the cathode shielded from the solenoidal magnetic field, Eq. (2.98) reduces to

$$\ddot{r} = -r\left(\frac{eB_z}{2\gamma m_0 c}\right)^2 + \frac{2eI}{\gamma m_0 c r}\left[\frac{1}{\beta} - \beta\right] \quad . \tag{2.99}$$

If the beam is focused to a waist ($\dot{r} = 0$) at a given radius r_0, the condition for a beam of constant radius (Brillouin flow) thereafter is

$$\dot{r}(r_0) = 0 \quad . \tag{2.100}$$

To meet this condition the field inside the solenoid must be

$$B_z = \sqrt{\frac{.8}{300}\frac{1}{\beta\gamma}\left(\frac{m_0c^2}{e}\right)\frac{I}{r_0^2}} \quad , \tag{2.101}$$

where m_0c^2/e is measured in volts, I in amps, r_0 in centimeters, and B in Gauss. The original CID design called for a beam radius of $\sigma = .8$ cm in the subharmonic bunchers and the drift spaces following them. The design called for a beam radius of $\sigma = .5$ cm in the S-band buncher and capture regions. For an initial current of 15 amps and initial energy of 200 kV, the field needed to maintain a beam radius of .8 cm is

$$B_z = 182 \text{ Gauss} \quad .$$

The field must become stronger as bunching proceeds and the current increases.

During much of the CID development effort we operated with the parameters outlined in Table 3.5 (see Sec. 3.2). The focusing solenoids were run at currents which produced the field profile shown in Fig. 2.50. Estimating the peak currents from Fig. 2.50 as the beam is bunched, we can calculate the beam radius. Our calculations yield average beam radii of about half of the design radius, or $r \simeq$ 2.5 mm. As discussed in the last section, smaller beam radii in the buncher and capture regions sacrifice optimal longitudinal bunching for a decrease in radial emittance growth. This operating mode came about in the days when transverse beam breakup severely limited transmission through Sector 1 to the damping ring. Thus trading longitudinal bunching for less emittance growth may have increased overall transmission to the damping ring. Since a stronger focusing lattice has been installed in Sector 1, radial emittance growth is not likely to be the limiting factor in total charge transmitted to the damping ring.

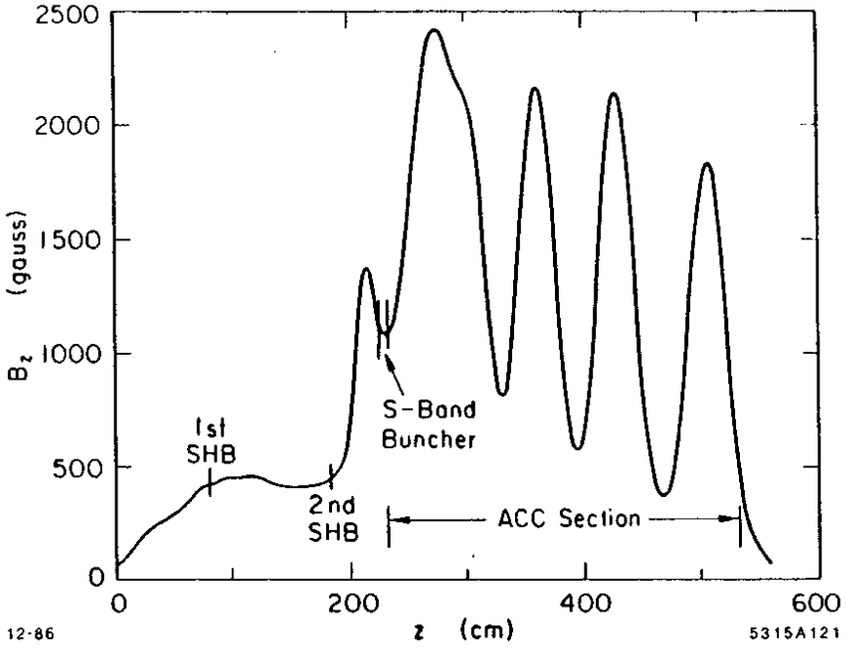

Fig. 2.50. Longitudinal magnetic field profile in the CID subharmonic prebunchers, S-band buncher and capture region.

CHAPTER 3.
PERFORMANCE OF CID

The collider injector discussed in Section 2.2.3 was assembled and commissioned in the spring of 1981.[12] From 1981 to 1984 the injector was used extensively to study the dynamics of high current single bunch beams in accelerator structures and to provide single bunch beams for damping ring studies.[18] CID was also available intermittently for studies to understand and improve injector performance.[19,20] Since the fall of 1984, CID has been used continuously to provide high current electron bunches to the SLC. From the spring of 1981 until spring of 1984, by far the most serious and time-consuming problem of the injector/Sector 1 development project was our inability to transmit high current single bunch beams from CID through Sector 1 to the damping ring. We were unable to transmit more than 2×10^{10} electrons in a single bunch through Sector 1 because of misalignment between CID and the old main injector and transverse emittance growth due to wake fields.[21] Due to this impass most of the measurements discussed in this chapter were made on bunches containing approximately 5×10^{10} electrons at the end of the CID accelerator section, the lower limit of the SLC specification.

In the next section we describe the hardware that makes up the CID injector; we then describe a "typical" operating mode which produces single bunches containing 5×10^{10} electrons. We compare this "typical" mode of operation to our initial design and to an updated RINGMODEL calculation. Finally, we discuss transverse emittance measurements.

3.1 Hardware Description of the CID Injector

As discussed in Section 2.2.3 the collider injector consists of a thermionic electron gun, two gap-and-drift prebunchers at the 16th subharmonic of the SLAC S-band accelerator frequency, a 10.5 cm long traveling-wave buncher and a three-meter long S-band traveling-wave accelerator section, of which roughly the first 20 cm act as the capture region (see Fig. 3.1). Each component of the system is discussed in detail below.

3.1.1 Electron Gun

Electron pulses for CID are provided by a high current, thermionic gun (see Fig. 3.2). The gun consists of a dispenser cathode, a biased grid, focus electrode, anode and an avalanche-type pulser designed by R. F. Koontz.[22,23] Until the summer of 1984 the pulser, cathode and grid were mounted inside a high voltage tank filled with one atmosphere of SF_6. This tank dependably stood off -150 kV, but was less reliable at higher voltages; thus the gun was regularly run at -150 kV. In the summer of 1984 the SF_6 tank was replaced by a smooth-surfaced high voltage deck that reliably stands off -200 kV in air. Because most of the measurements reported here took place before summer 1984, all computer simulations and measurements in this report were made at cathode voltages of -150 kV.

The grid bias voltage can easily be varied between 60 V and 290 V. As the bias voltage is reduced, the peak current of the gun pulse increases from 0 to a maximum of 10 amps. Unfortunately, the width of the gun pulse is a strong function of peak current (see Fig. 3.3). The pulser produces a roughly Gaussian-shaped pulse of fixed FWHM. As the bias is applied, the pulse is "clipped" from the bottom, leaving a "smaller" Gaussian.

At a bias of 60 V the thermionic gun can easily produce up to 2.5×10^{11} electrons (10 amps, 4 ns FWHM) in one pulse. This pulse is much too wide to

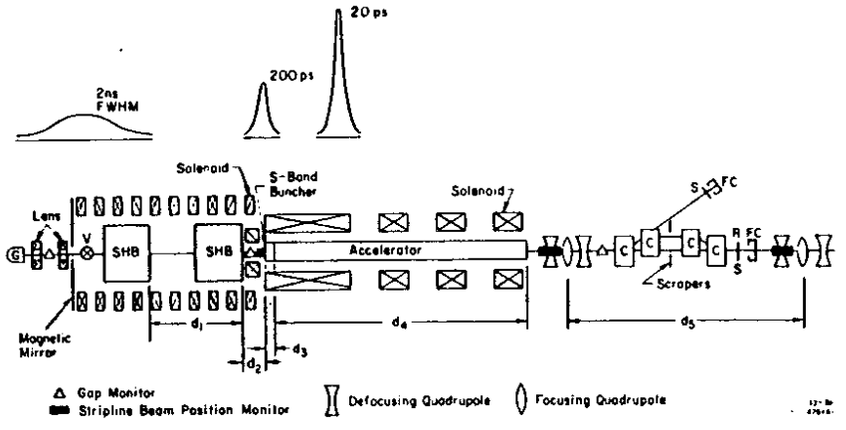

Fig. 3.1 Schematic of collider injector in spring 1984.

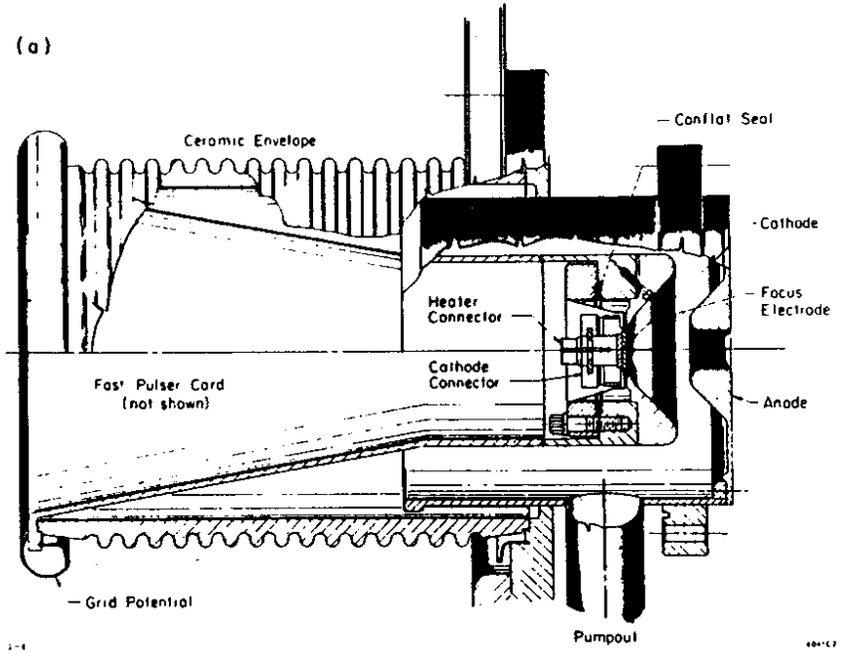

Fig. 3.2.(a). Cut-away view of the CID thermionic gun assembly.

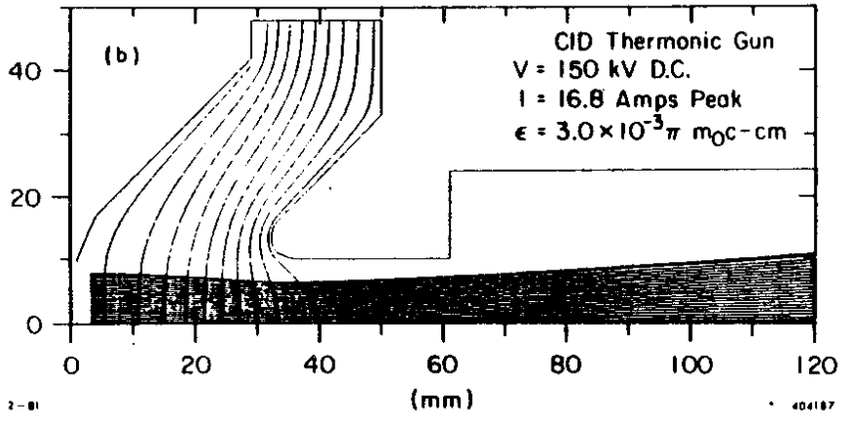

Fig. 3.2(b). Computer simulated beam optics for the CID thermionic gun.

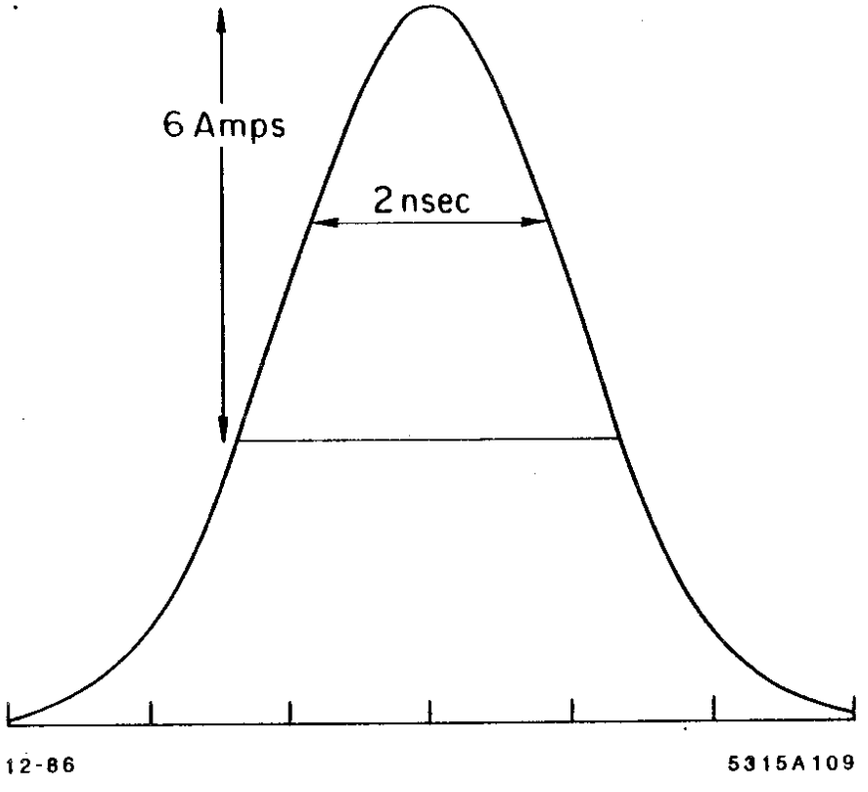

Fig. 3.3. Sketch of a space charge limited Gaussian gun pulse which produces a 6 A, 2 ns FWHM pulse at a bias of 150 V.

be captured into a single S-band bunch. Even at 7.5×10^{10} electrons per pulse, the CID gun produces a pulse twice as wide as anticipated in the original design. Rather than a 12 amp and 1 ns FWHM pulse, the CID gun produces a 6 amp, 2 ns FWHM pulse. This affects the bunching process.

Table 3.1. Peak current and FWHM versus bias voltage on the CID gun.

Bias Voltage	Peak Current	FWHM	Total Charge
65 V	8.5	4.2	22×10^{10}
150 V	6.0	2.0	7.5×10^{10}
290 V	5.0	1.1	3.4×10^{10}

3.1.2. Subharmonic Bunchers

The gap-and-drift prebunchers each consist of a standing wave buncher at the 16th subharmonic of S-band followed by an appropriate drift space. The subharmonic bunchers (SHB) are one-quarter wavelength, coaxial cavities, with a 4 cm gap in the inner conductor at one end of each cavity (see Fig. 3.4). The cavities are driven at 178.5 MHz in the TEM mode. As shown in Fig. 3.4, the gap in the inner conductor distorts the transverse electric field, producing a longitudinal electric field across the gap.

The cavities have unloaded Q's of approximately 12,000. The gap voltage, V as a function of time is given by

$$V(t) \propto \left(1 - e^{-(\omega/2Q_L)t}\right) \tag{3.1}$$

where Q_L is the loaded Q of the cavities.

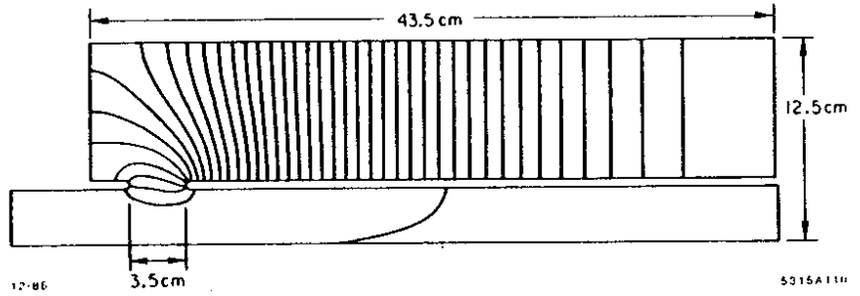

Fig. 3.4. Cross section of a quarter-wave length coaxial subharmonic buncher cavity showing electric field lines.

At the time of CID's construction, the earliest available trigger came 25 μs before beam time. For a Q_L of 12,000, the cavities reach 95% of their steady-state fields after 25 μs. By overcoupling the cavities we reduced the loaded Q to approximately 4000, which decreased the filling time by a factor of three, so that the cavities were less than .1% below their steady state value after 25 μs. As SLC calls for two electron pulses spaced 59 ns apart, we need to know the difference in gap voltage for the two pulses. Let ΔV be the difference in the gap voltage between the pulses and Δt the time between pulses:

$$\frac{\Delta V}{V} = \frac{(dV/dt)\Delta t}{V} = \frac{\omega}{2Q_L}\frac{e^{-(\omega/2Q_L)t}}{1-e^{-(\omega/2Q)t}}\Delta t \quad . \tag{3.2}$$

For our cavities we find

$$Q_L = 12000 \qquad \frac{\Delta V}{V} = 3.6 \times 10^{-2} \quad , \tag{3.3a}$$

$$Q_L = 4000 \qquad \frac{\Delta V}{V} = 2.7 \times 10^{-4} \quad . \tag{3.3b}$$

In either case, the change in gap voltage between bunches is negligible. Given the resonant frequency and Q_0, the shunt impedance of the cavities has been calculated by SUPERFISH, a computer code which solves Maxwell's equations in the presence of cylindrically symmetrical boundary conditions.[24] The cavity shunt impedances are approximately $2.2 \times 10^6 \Omega$.

The steady state gap voltage in each cavity is proportional to

$$V_{gap} \propto \sqrt{R_s P} \quad . \tag{3.4}$$

Typical operating voltages for the cavities are $V_{gap} = 42$ kV for the first gap and 65 kV for the second gap.

As discussed extensively in Chapter 2, optimum bunching by the subharmonic bunchers is accomplished when we exploit the curvature of the sinusoidal RF by

shifting the phase of the null of the sine wave with respect to the center of the electron pulse.

The phases of the SHB cavities relative to the phases of the S-band buncher and accelerator have not been measured directly. We were able to measure the difference in time of flight of the electrons from the gun to just downstream of the accelerator section with the SHB gap voltages on and off. Figure 3.5(a) shows a gap monitor signal from just downstream of the accelerator section with the SHB power off. The 2 ns FWHM Gaussian shaped gun pulse is captured onto approximately ten adjacent S-band crests. The signal on the left of Fig. 3.5(b) is the same 2 ns gun pulse with the SHB power on with no phase adjustment. The signal on the right is the 2 ns gun pulse with the SHB phases adjusted to achieve the most electrons on a single S-band crest. Note that the electrons now arrive at the gap monitor ~700 ns later; this is due to the phase shift in the subharmonic bunchers. As discussed in Section 2.2.1, the subharmonic bunchers are more effective if the phase of the RF is shifted by 30° or so, decelerating the center of the electron gun pulse. The center of the bunch arrives at some downstream point (i.e., the gap monitor) at a later time than it would have had the SHB's been off. The difference in arrival time at the gap monitor between the phase shifted and non-phase shifted bunches is

$$\Delta t = t_{SH} - t_{NSH} = \frac{d_1}{\beta_1 c} + \frac{d_2}{\beta_2 c} - \frac{(d_1+d_2)}{\beta_0 c} \tag{3.5}$$

where

$t_{SH}(t_{NSH})$ = time of flight of the center of the bunch with the phase of the SHB's shifted (not shifted)

$\beta_1(\beta_2)$ = velocity of the center of the bunch after the first (second) SHB

β_0 = velocity of the center of the bunch with the SHB's off

$d_1(d_2)$ = drift distance following the first (second) SHB's (see Fig. 3.1, d_1 = 108 cm, d_2 = 36 cm).

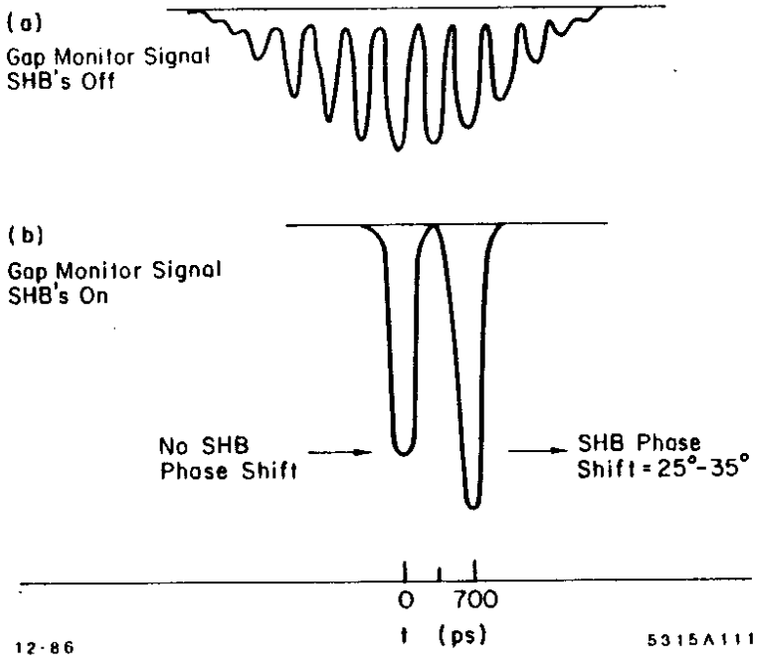

Fig. 3.5. Beam current versus time as measured by a gap monitor located just downstream of CID's three-meter accelerator section. (a) Gap monitor signal with subharmonic bunchers off. (b) Gap monitor signal with subharmonic bunchers on. No phase shift results in the signal on the left [the compressed bunch arrives at the gap monitor at the same time as the peak of the uncompressed bunch of Fig. 3.5(a)]. A phase shift of 25°-35° results in the signal on the right. The shift has resulted in lower velocities, thus the later arrival time at the gap monitor. More electrons have been captured into a single S-band bunch producing a higher peak signal.

β_1 and β_2 are given by

$$\beta_1 = \sqrt{1 - \frac{1}{\gamma_1^2}} = \sqrt{1 - \frac{1}{\left(\frac{E_0 - E_1 \sin\theta}{m_0 c^2}\right)^2}} \tag{3.6}$$

and

$$\beta_2 = \sqrt{1 - \frac{1}{\gamma_2^2}} = \sqrt{1 - \frac{1}{\left(\frac{E_0 - (E_1 + E_2)\sin\theta}{m_0 c^2}\right)^2}} \quad . \tag{3.7}$$

Actual CID operating parameters are given in Table 3.5.

Table 3.2 shows the time of flight as a function of phase-shift in the SHB's where we have assumed that both bunchers are shifted by the same amount of phase.

Table 3.2. Time-of-flight as a function of SHB phase.

Phase Shift (degrees at 178.5 MHz)	Time-of-flight (psec)
35	840
30	690
25	560
20	430
15	310

From Table 3.2 we see that a 15 to 20° phase shift should result in the center of the bunch being captured one S-band bucket later than it would be captured with no phase shift; 25 to 35° phase shift results in the bunch being captured two S-band buckets later. In tuning CID one usually finds that the most charge is captured two buckets later, implying a shift of $\sim 30°$ as expected.

The SHB's can compress ~ 2.5 ns of the gun pulse into one cycle of S-band. Electrons at greater distances from the center of the bunch are lost or captured into earlier or later S-band buckets.

3.1.3. The Traveling-Wave Buncher

The buncher is a traveling wave disk-loaded structure with phase velocity $\beta_p = .75$. The buncher consists of four cavities. RF power from the CID klystron is coupled into the first cavity, flows through the middle cavities and is extracted from the fourth cavity. The buncher operates in the $2\pi/3$ mode (i.e., three cavities per guide wavelength, $\lambda_g = \beta_w c/f$, where f is the S-band frequency). Thus the four cavities are one free space wavelength long. The main features of the buncher are summarized in Table 3.3.

Table 3.3 Buncher parameters.

Frequency	$F = 2856$ MHz
Disk aperture diameter	$2a = 2.26$ cm
Shunt impedance	$r/Q = 36.9$ ohms/cm
Cavity inside diameter	$2b = 8.33$ cm
Group velocity	$v_g/c = 0.0118$
Disk thickness	$t = .584$ cm
Peak power	5.4 MW*
Periodic length	$d = 2.628$ cm
Peak field	110 kV/cm*

*Maximum available.

The buncher is coupled to the CID accelerator section by means of a 1.9 cm-thick copper spacer with a .95 cm inner radius. Power for the buncher is provided by the CID klystron by way of a 7.25 dB coupler located in the CID vault. Approximately 5.6 MW of klystron power is coupled to the buncher. A phase shifter and attenuator downstream of the 7 dB coupler allow for independent control of buncher phase and power.

3.1.4 Accelerator Section

The CID accelerator section is a standard SLAC three-meter accelerator section which is described in great detail in Ref. 25. Briefly, the section is made up of 86 cavities whose disk aperture diameters and inside cavity diameters vary such that the field gradient across each cavity is constant along the section. The accelerator section has a phase velocity $\beta_w = 1$ and operates in the $2\pi/3$ mode. Features of the accelerator section are summarized in Table 3.4.

Table 3.4 Accelerator Parameters

Frequency	$f = 2856$ MHz
Structure type	Constant gradient
Shunt impedance	r = 57 MΩ/meter
Disk aperture diameter	$2a = 2.62 - 1.92$ cm
Group velocity	$v_g/c = 0.0204 - 0.0065$
Cavity inside diameter	$2b = 8.35 - 8.8$ cm
Peak power	25 MW
Disk thickness	$t = .584$ cm
Peak field	178 KV/cm
Periodic length	$d = 3.5$ cm

Power to the CID section is provided by the CID klystron, which has a peak power of 37.1 MW. After waveguide attenuation and coupling to the S-band buncher, 25.3 MW of power reaches the three-meter accelerator section. Given the Ref. 17 r/Q of 42 Ω/cm, this yields a peak field gradient of 178 kV/cm.

3.2. Comparison of a Typical Performance to Calculated Performance of CID

As discussed in the introduction to this chapter, most of the development work on CID concerned captured bunches containing approximately 5×10^{10} electrons. In this section we present the performance data for a typical operating setup and compare it to results predicted by the computer simulation program, RINGMODEL. The operating parameters are summarized in Table 3.5 and described in detail below.

The parameters of Table 3.5 were used as input to the RINGMODEL computer program. Figures 3.6-3.11 illustrate the predictions of the model for bunching and capture of a 6 amp, 2 ns FWHM, Gaussian gun pulse. The results of the simulation are described below. Finally the bunch produced by the CID injector is compared to the results of the simulation.

As stated earlier, CID was originally designed to bunch a 12 amp, 1 ns FWHM gun pulse. The actual gun pulse containing the same charge ($\sim 7.5 \times 10^{10}$ electrons) is closer to 6 amps, 2 ns FWHM and is illustrated in Fig. 3.9(a). The $\pm 2\sigma$ extent of the pulse is some 3.4 ns. Figure 3.8(a) shows the longitudinal emittance of the bunch immediately downstream of the first subharmonic buncher gap. It is clear that the 3.4 ns pulse extends far beyond the linear region of the 178.5 MHz sine wave, over some 215° of subharmonic phase. As discussed in Section 2.2.1, better bunching in the subharmonic buncher region is obtained if the bunch is shifted 30° forward on the RF, as shown. The bunch drifts for 108 cm producing the bunch shown in Fig. 3.9(b). The bunch has been compressed by about a factor of two. Note that it is reasonably symmetrical.

Upon entering the second SHB, the phase of the bunch with respect to the RF is again shifted by 30°. Figure 3.8(c) represents the emittance at the end of the 36 cm drift following the second SHB. As shown in Fig. 3.9(c), some 80% of the original gun pulse has been bunched into 200° of S-band phase. The bunch has been compressed by a factor of five.

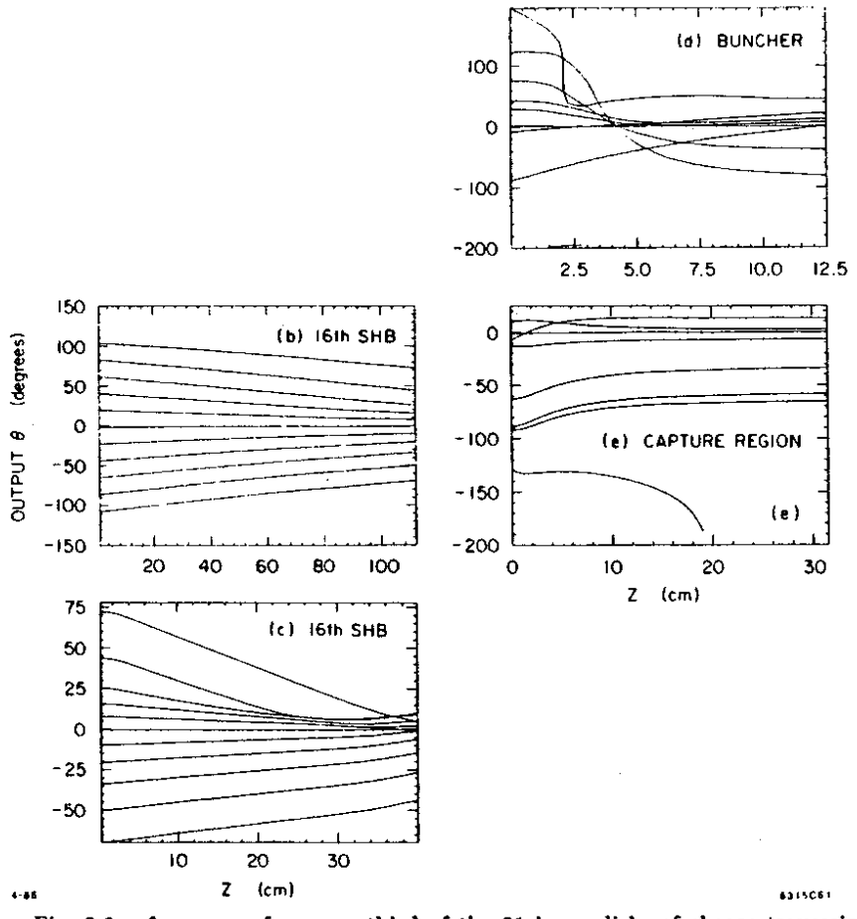

Fig. 3.6. θ versus z for every third of the 31 inner disks of charge traversing the injector as specified in Table 3.5. (b) First 16th subharmonic buncher gap and 108 cm drift. θ is measured in degrees at 178.5 MHz. (c) Second 16th subharmonic buncher gap and 36 cm drift. θ is measured in degrees at 178.5 MHz. (d) S-band buncher and 2 cm drift. θ is measured in degrees at S-band. (e) First 30 cm of the three-meter accelerator section. θ is measured in degrees at S-band.

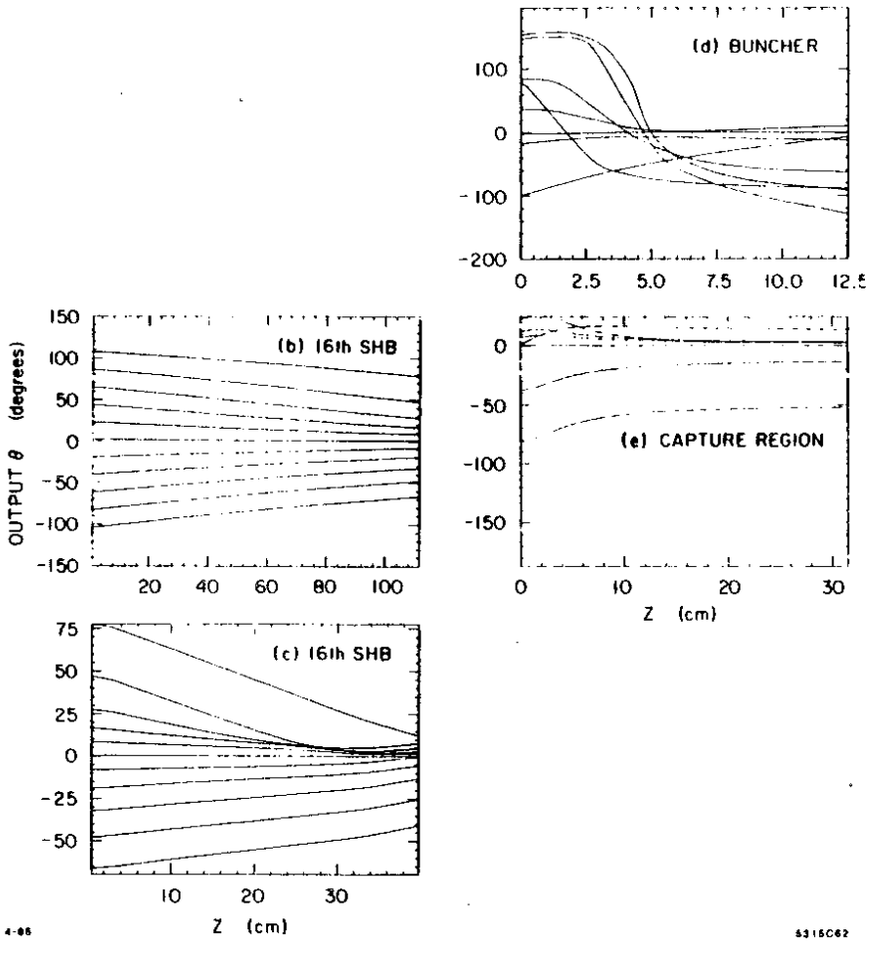

Fig. 3.7. θ versus z for every third of the 31 outer annuli of charge traversing the injector as specified in Table 3.5. (b) First 16th subharmonic buncher gap and 108 cm drift. θ is measured in degrees at 178.5 MHz. (c) Second 16th subharmonic buncher gap and 36 cm drift. θ is measured in degrees at 178.5 MHz. (d) S-band buncher and 2 cm drift. θ is measured in degrees at S-band. (e) First 30 cm of the three-meter accelerator section. θ is measured in degrees at S-band.

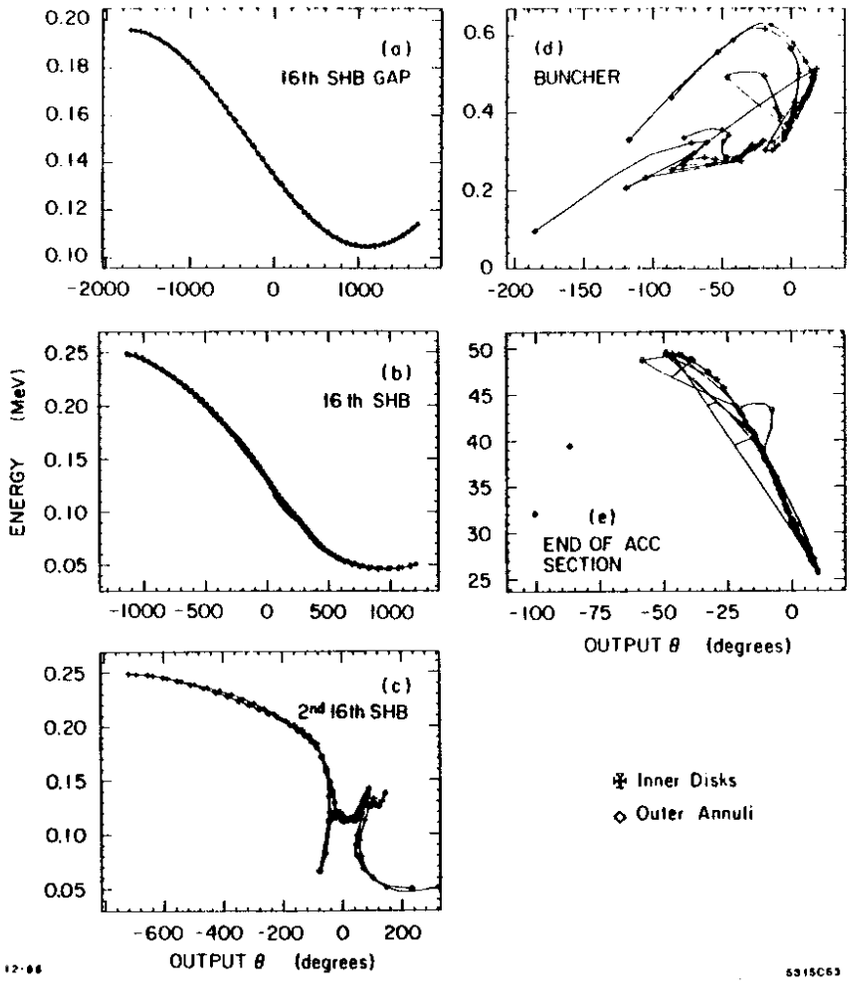

Fig. 3.8. Longitudinal emittance at five locations in the injector as specified in Table 3.5. θ in all figures is measured in degrees at S-band. (a) At output of the first 16th subharmonic buncher gap. (b) End of 108 cm drift. (c) End of 36 cm drift following second 16th subharmonic buncher gap. (d) End of 2 cm drift following S-band buncher. (e) End of three-meter accelerator section.

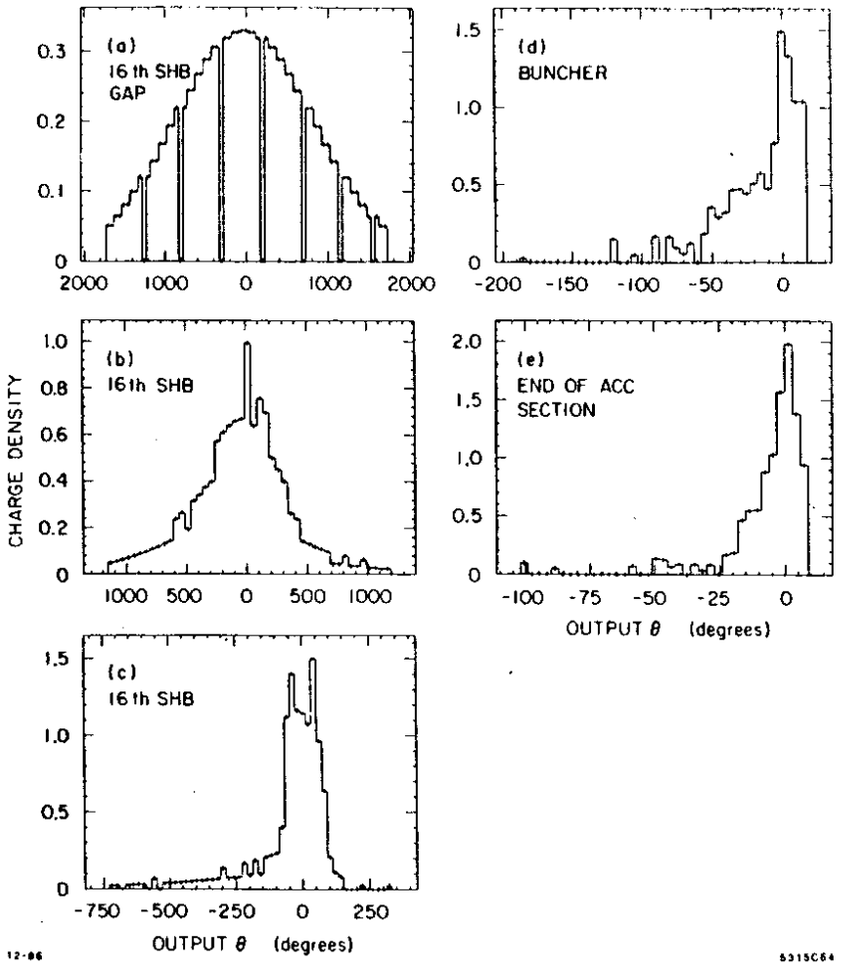

Fig. 3.9. Bunch length at five locations in the injector as specified in Table 3.5. θ in all figures is measured in degrees at S-band. (a) At output of the first 16th subharmonic buncher gap. (b) End of 108 cm drift. (c) End of 36 cm drift following second 16th subharmonic buncher gap. (d) End of 2 cm drift following S-band buncher. (e) End of three-meter accelerator section.

Table 3.5. Bunch length and current at five locations in the CID injector for a typical operating configuration.

Element	Peak Current	FWHM S-band Degrees	Base ($\sim \pm 2\sigma$) S-band Degrees	Total Charge	Field Strength
Gun (experimental)	6 amps	2000°	3400°	$7.5 \times 10^{10} e^-$	150 kV
End of first 178.5 MHz SHB	14 amps	850°	2400°	$7.5 \times 10^{10} e^-$	12 kV/cm (×3.8 cm)
End of second 178.5 MHz SHB	83 amps	80°	400°	$6.8 \times 10^{10} e^-$	18 kV/cm (×3.8 cm)
S-band buncher	240 amps	35°	100°	6.3×10^{10}	44 kV/cm
Accelerator section (calc.)	875 amps	10°	48°	6.2×10^{10}	175 kV/cm
(Experimental)	430 amps	18°	44°	5.5×10^{10}	

The beam emittance entering the buncher is shown in Fig. 3.8(c). In Fig. 3.10 this emittance is shown superimposed on the low current phase space orbits of the S-band wave buncher. As the bunch travels through the S-band buncher, it "folds over" in phase space producing the emittance shown in Fig. 3.8(d). Note that the field is a factor of three higher than the design field. Higher fields are necessary because the beam enters the buncher at a lower momentum due to the phase shifts in the subharmonic bunchers and exits the buncher at a higher momentum than p_w. As shown in Fig. 3.9(d), all of the charge within $\pm 100°$ at the entrance to the buncher is now within 75°, with another $.5 \times 10^{10} e^-$ in a tail extending out some 100°.

Phase space orbits in the capture region are plotted in Fig. 3.11. At the end of the accelerator section 80% of the gun pulse or $6.2 \times 10^{10} e^-$ has been captured into 40° with a 10° FWHM. The longitudinal bunch shape, spectrum, transverse emittance and total charge have been measured with diagnostic devices located downstream of the CID three-meter accelerator section.

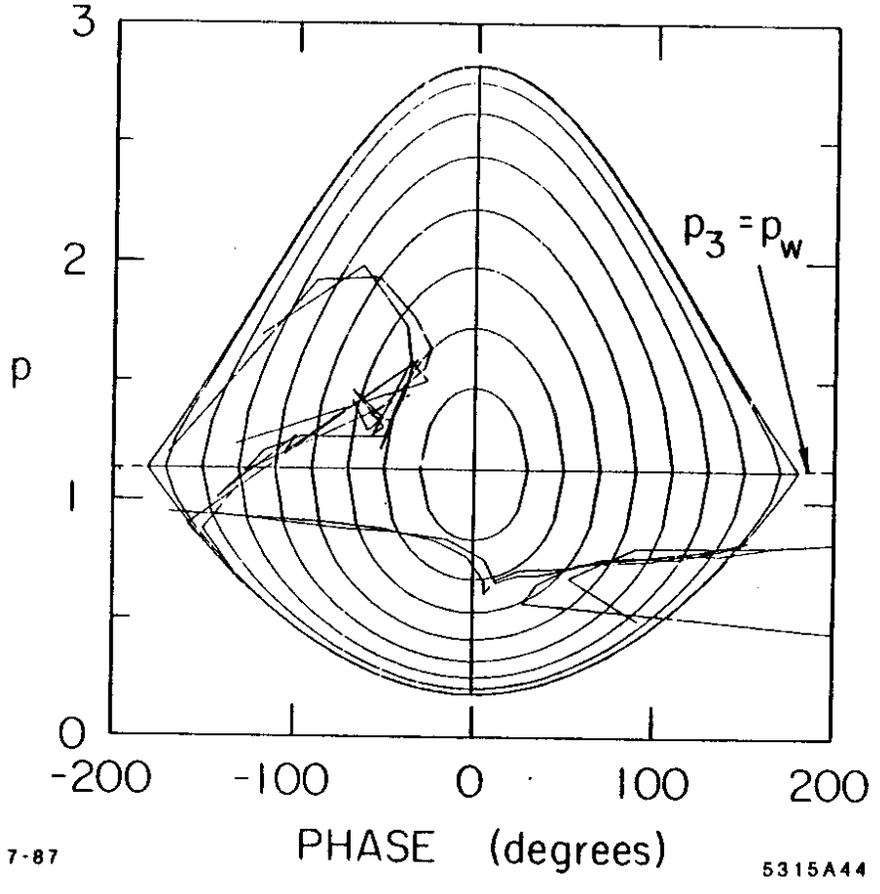

Fig. 3.10. Beam emittance at the entrance to and exit from the S-band buncher superimposed on the low-current buncher phase space orbits for the parameters specified in Table 3.5.

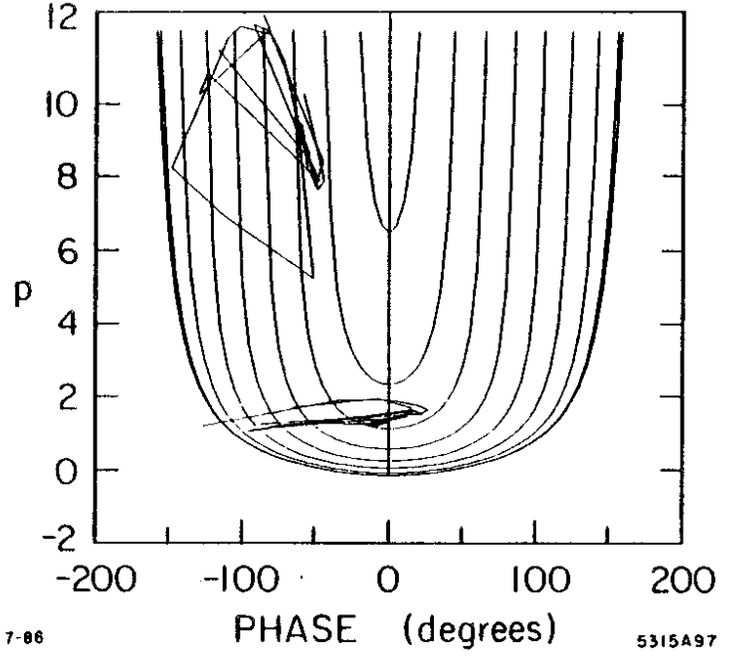

Fig. 3.11. Beam emittance at the entrance to the capture region and 30 cm downstream superimposed on the capture region low-current phase space orbits for the parameters specified in Table 3.5.

The longitudinal bunch shape is measured using a streak camera via the optical system described in Appendix A. Degradation in resolution from a number of sources causes broadening of the streak camera image. The effect of this degradation on the streak camera image is estimated in Appendix A and shown graphically in Fig. 3.12(b). A delta function charge density would produce a signal with a FWHM of 4 ps duration with a baseline of 32 ps duration. Before comparing the calculated bunch shape [Fig. 3.9(e)] to the experimental bunch shape, we must convolve the calculated bunch shape with the (estimated) resolution degraded delta function. Figure 3.12(a) is the calculated bunch of Fig. 3.9(e). Figure 3.12(c) is the calculated bunch shape as seen by the streak camera [i.e., after Fig. 3.12(a) is convolved with Fig. 3.12(b)]. In Fig. 3.13, we compare the resolution-broadened calculated bunch shape with the bunch shape measured by the streak camera. The calculated base width and total charge are in good agreement with experiment. On the other hand the measured FWHM is somewhat wider and the rise time is about twice as long as expected. These discrepancies are not explained by the calculated image degradation due to the imaging system and streak camera.

As discussed in Appendix A, we suspect that other factors contribute to the image degradation, which prevent us from seeing the faster rise time we expect and that the actual beam shape is in closer agreement with calculation than is demonstrated here.

To meet collider specifications, the experimental bunch shape of Fig. 3.13 must have $\Delta E/E < \pm 1\%$ at the entrance to the damping ring. By a proper choice of phase shift, we can use the wake fields to partially offset the variation in energy due to the sinusoidal RF. Loew and Wang[26] have pointed out that by judicious choice of bunch shape and phase shift, one can use the wake fields to offset the variation in energy due to the RF to achieve excellent spectra.

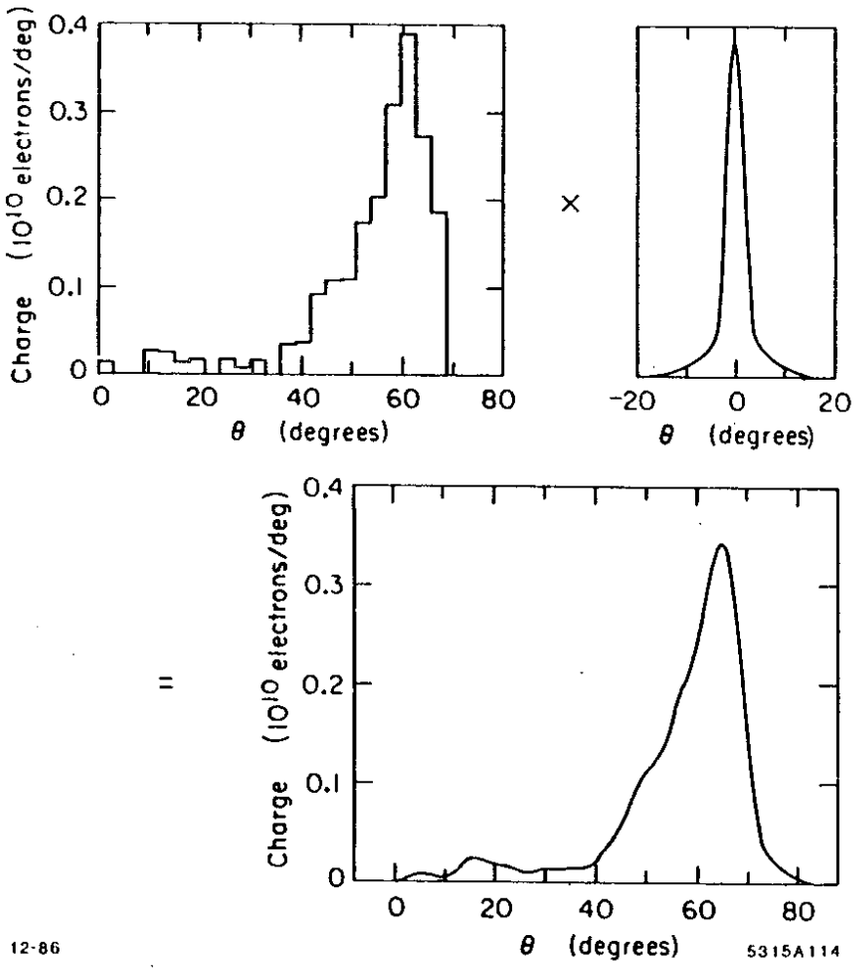

Fig. 3.12. (a) The calculated bunch shape at the end of CID for the parameters given in Table 3.5. (b) The streak camera signal from a δ-function pulse given the resolution limitations described in Appendix A. (c) The calculated bunch shape convolved with the estimated resolution error.

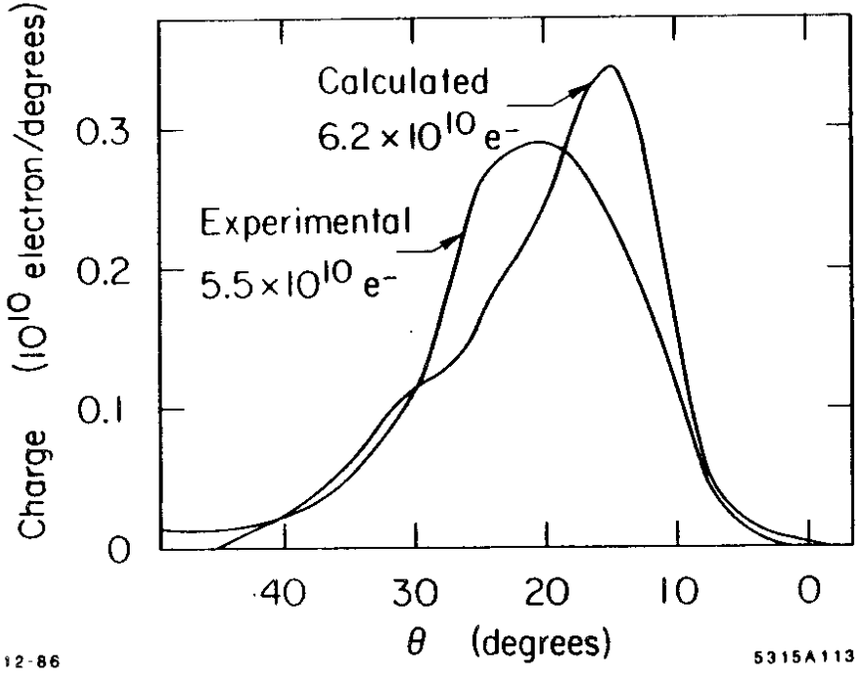

Fig. 3.13. Calculated and measured bunch shape at the end of CID for the operating conditions outlined in Table 3.5.

Figure 3.14(a) is the experimental bunch shape of Fig. 3.13. The head of the bunch is on the far right at 0°; the tail of the bunch is at 44°. For a low current beam, the energy of each particle at the entrance to the damping ring is a function only of its phase with respect to the accelerator RF fields. In Fig. 3.14(b), the dashed curve shows particle energy as a function of RF phase for a low current beam. The head of the bunch (0°) has been shifted 12° forward of the RF crest. The solid line shows particle energy as a function of phase for our actual beam current. Again, the head of the bunch has been shifted 12° forward of the RF crest, and the energy of the particles near the crest is reduced by the wake fields. Figure 3.15 is the calculated spectrum at the entrance to the damping ring given the 12° phase shift of Fig. 3.14(b). The 5×10^{10} electrons are contained within ±1% with another 0.5×10^{10} electrons failing to fall within the damping ring acceptance. As predicted, 5×10^{10} electrons have been successfully injected into the damping ring.

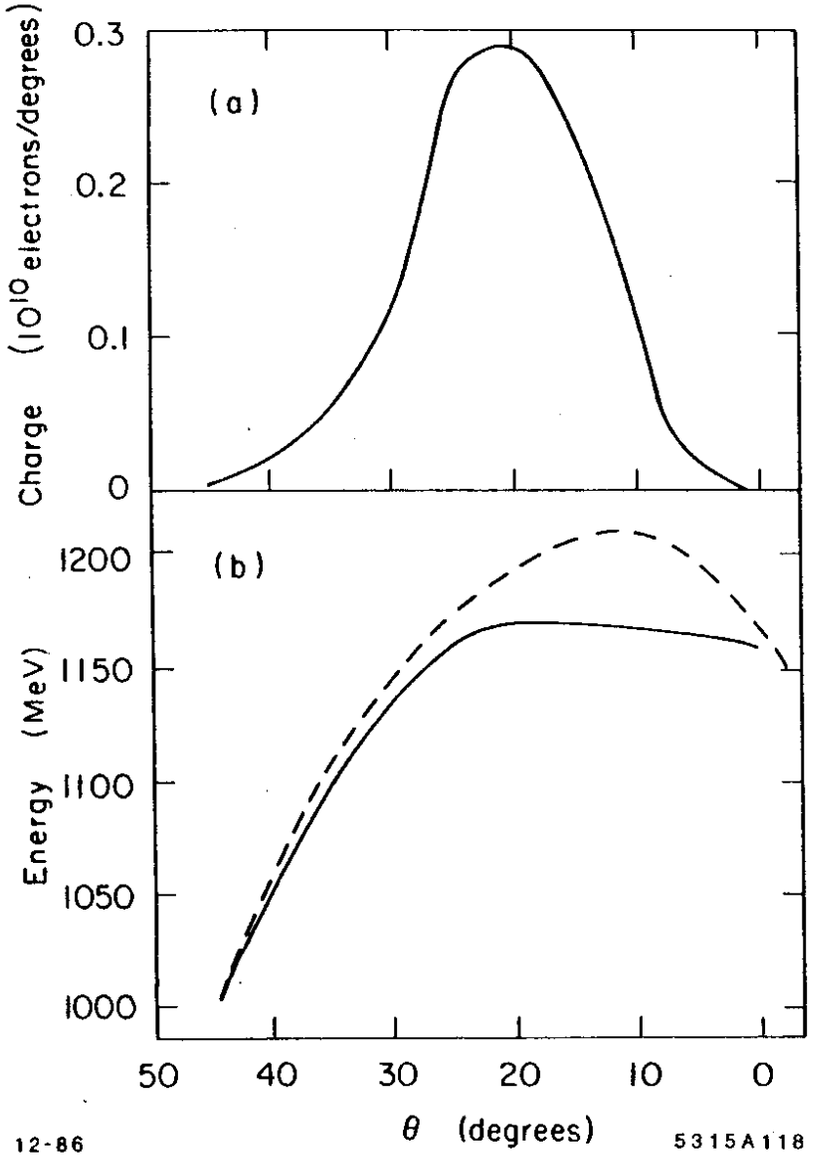

Fig. 3.14. (a) Measured bunch shape at the end of CID. The head of the bunch is at the far right at 0°. The tail of the bunch is at 44°. (b) The dashed curve shows the energy of the particles at the entrance to the damping ring as a function of phase in the low current limit. The head of the bunch, 0°, is shifted 12° ahead of the RF crest. The tail of the bunch is 32° behind the RF crest. The solid curve shows energy as a function of phase for the actual CID current.

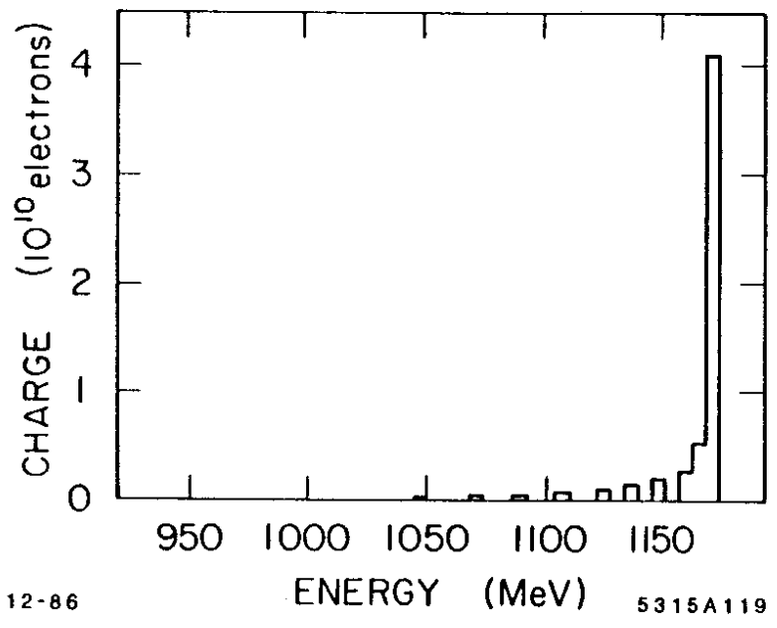

Fig. 3.15. The calculated spectrum at the entrance to the damping ring for the measured bunch of Fig. 3.14(a).

3.3 TRANSVERSE EMITTANCE MEASUREMENT

In this section we discuss the measurement of the transverse emittance of the CID beam as a function of current. We begin with a qualitative discussion of the measurement technique which is described in detail in Ref. 27.

The transverse emittance of the CID beam is measured by varying the strength of a quadrupole triplet located just downstream of the CID accelerator section. The beam then drifts to a screen located 1.2 meters downstream of the triplet where the transverse spot size is read by a "reticon" array. If we plot one dimension of the beam spot size as a function of the inverse focal length of the triplet, it can be shown that the resulting function is a hyperbola (see Fig. 3.19). The minimum of the hyperbola and the slope of the positive asymptote tell us the emittance of the beam at the triplet. To obtain a qualitative understanding of this technique, it is helpful to restrict the following discussion to an emittance measurement in the x, x' plane, where x' is β_x, the normalized transverse particle velocity in the x direction. The emittance in the y, y' plane is measured in identical fashion.

Let us assume that the arbitrary ellipse 1 of Fig. 3.16(a) represents the x, x' phase space just upstream of the quadrupole triplet. It is instructive to circumscribe the ellipse by a parallelogram which is tangent to the ellipse at its position extrema and at its intersection with the ordinate axis.

Conceptually, it is simplest to think of the quad triplet as performing two independent tasks and that these tasks are performed by two independent lenses. The first lens rotates ellipse 1 to the supine ellipse 2 [see Fig. 3.16(a)]. For ellipse 2 the maximum values of x_1 and x_1' give us the emittance. The second lens is varied to yield the functional dependence of spot size on focal length, from which we can calculate the maximum values of x_1 and x_1' of Fig. 3.16(a).

To find x_1' we choose the focal strength of the second lens to achieve a minimum spot size on the screen a distance L downstream of the lens. The lens sheers ellipse 2 of Fig. 3.16(b) to ellipse 3. Note that this sheering due to focusing does

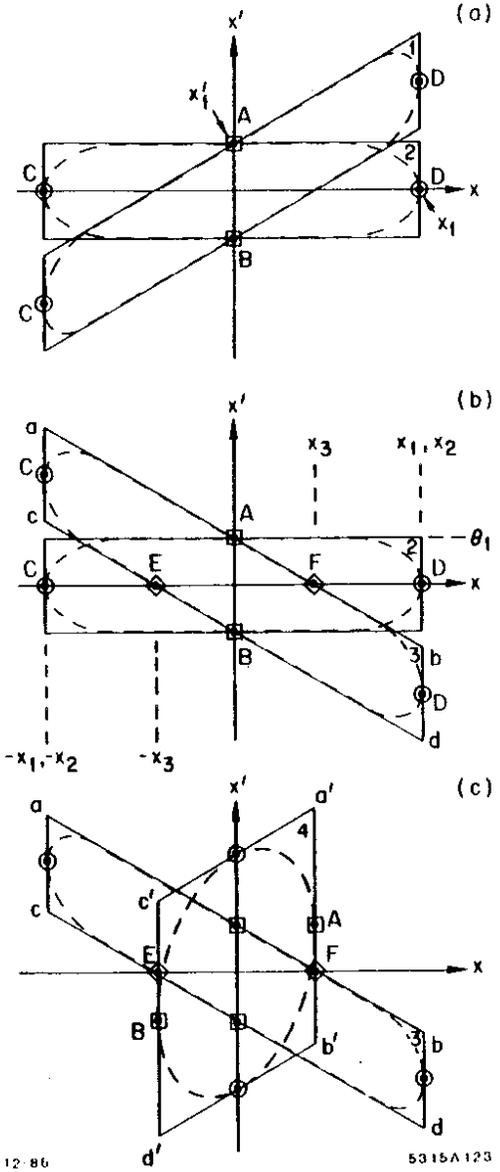

Fig. 3.16. (a) The arbitrary ellipse 1 represents the horizontal beam emittance at the upstream edge of the lens. The "first lens" is used to rotate the ellipse to the supine position. (b) The supine ellipse 2 is sheered by the "second lens" to achieve the smallest spot at the reticon array. (c) Ellipse 3 is sheered by drifting to achieve the smallest spot, ellipse 4.

not affect points A and B. We have chosen the lens strength such that after a drift of length L, ellipse 3 is sheered to ellipse 4 of Fig. 3.16(c). Since sheering due to drifting does not affect points E and F, the minimum spot size is obtained when line segment $\overline{ab}$ sheers to the vertical line segment $\overline{a'b'}$. Note that the focusing and drifting represented in Figs. 3.16(b) and (c) has transformed point A from the angular extremum to the position extremum. Figure 3.17(a) represents the ray corresponding to point A of Figs. 3.16(a), (b) and(c). At z_1 (before the lens) the ray is on the z-axis and is diverging from the axis at an angle x_1'. As this ray is not focused by the lens, its position at z_3 is given by

$$x_{3\,min} = x_1' L$$

where $x_{3\,min}$ is the minimum spot size at the screen. Rearranging, we have

$$x_1' = \frac{x_{3\,min}}{L} \quad . \tag{3.8}$$

Thus we know the momentum extent of the supine ellipse of Fig. 3.16(a) in terms of the measurable quantities $x_{3\,min}$ and L.

To find the position extent, x_1, of the supine ellipse of Fig. 3.16(a) we choose to make the focal length of the lens very short (see Fig. 3.18, ellipse 5). The beam then drifts for a length L, resulting in ellipse 6 of Fig. 3.18. The focusing and drifting of Fig. 3.18 has transformed point D from the positive position extremum to very close to the negative position extremum. Figure 3.17(b) represents the ray corresponding to point D of ellipse 1, 5 and 6. At z_1 (before the lens) the ray is displaced a distance x_1 from the z-axis and is parallel to the axis ($x_1' = 0$). At z_2 (just after the lens) the ray has been deflected through an angle of $-x_2'$. The displacement of the ray at the screen is given by

$$-x_3 = x_1 - x_2' L$$

or

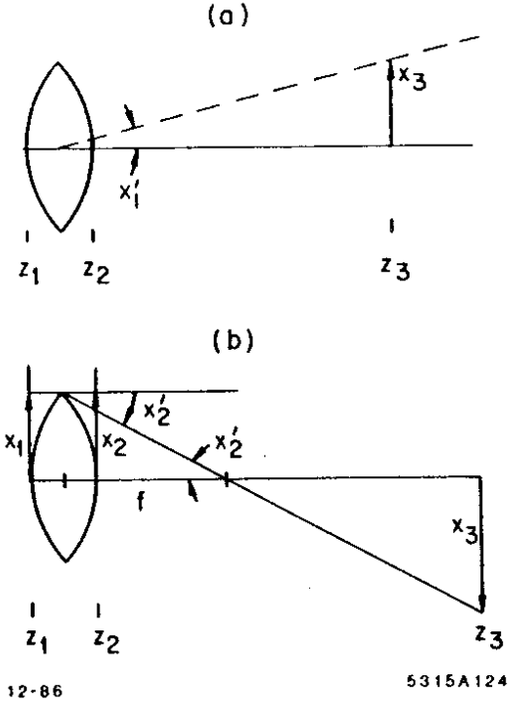

Fig. 3.17. Ray optics of (a) point A of Fig. 3.16, (b) point D of Fig. 3.18.

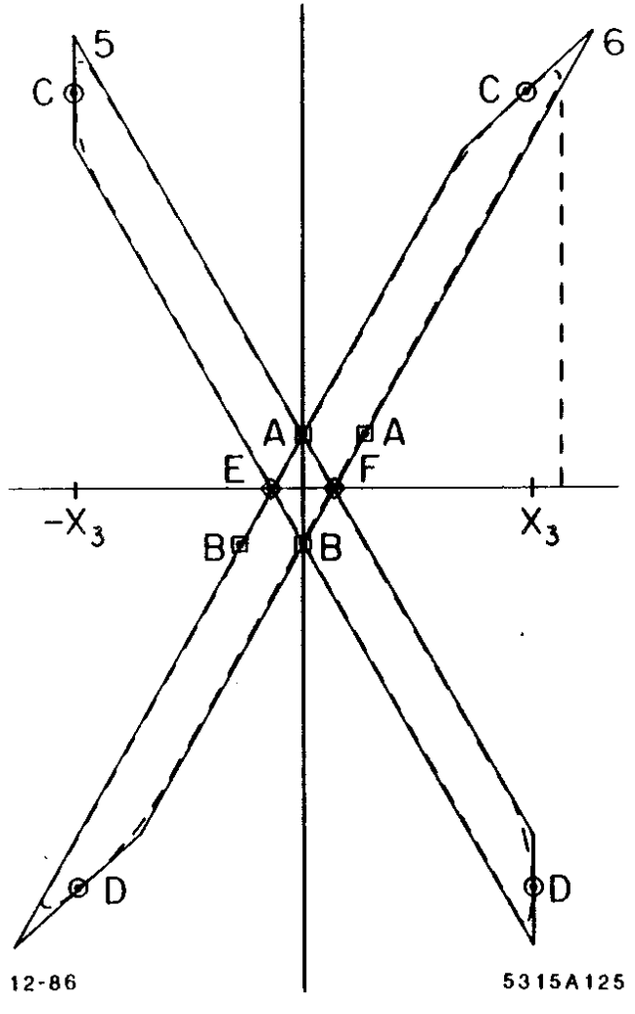

Fig. 3.18. Ellipse 2 of Fig. 3.16(b) is sheered by strong focusing to produce ellipse 5. The beam drifts to produce ellipse 6 at the screen.

$$x_3 = -x_1 + \frac{x_1}{f} L \quad . \tag{3.9}$$

Taking the derivative of x_3 as a function of $1/f$ we have

$$\frac{dx_3}{d(1/f)} = x_1 L$$

or

$$x_1 = \frac{1}{L} \frac{dx_3}{d(1/f)} \quad . \tag{3.10}$$

Thus we know the position extent of the supine ellipse 1 of Fig. 3.16(a) in terms of the measurable quantities $dx_3/d(1/f)$ and L provided $dx_3/d(1/f)$ is not varying appreciably (i.e., near the asymptote).

Figure 3.19 is a sketch of the beam spot size as a function of inverse focal length. As indicated by Eq. (3.8), the minimum of the hyperbola gives the angular extent at the focusing lens; from Eq. 3.10 we see that the slope of the asymptote gives the transverse displacement. Tracing out the entire curve gives a complete emittance measurement. The preceding discussion is intended to convey the principle of the emittance measurement. For a detailed discussion of the actual mathematical tools and experimental procedure see Ref. 27.

In Fig. 3.20 we plot emittance in both the vertical and horizontal planes as a function of beam current for several currents between 0.5 and 5.5×10^{10} electrons per bunch. Error bars are at $\pm\sigma$. Where no error bars are shown there were insufficient data to determine σ. At 5×10^{10} electrons per bunch, the invariant emittance along both the horizontal and vertical axes is approximately $1.5 \times 10^{-4}\, m_0 c$ meters (invariant), which is a factor of two below the value specified for the SLC.

The measured emittance as a function of beam intensity is reasonably fitted to a parabola given by $\epsilon = 7 \times 10^{-5} \sqrt{I}$ meter radian (invariant), where I is the current in $10^{10}\, e^-$/pulse. The form $\epsilon = kI^{1/2}$ is appropriate when the density in phase space remains constant as the current is varied.

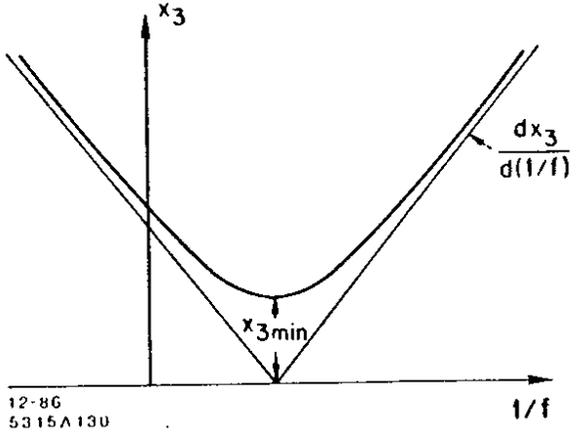

Fig. 3.19. Characteristic plot of beam spot size as a function of inverse focal length.

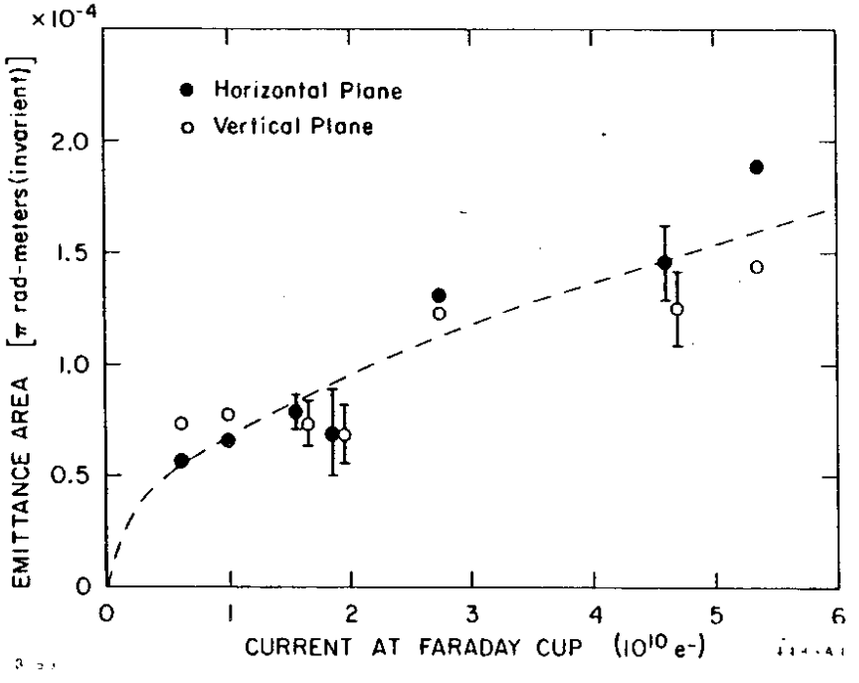

Fig. 3.20. Invariant transverse emittance as a function of current for the CID beam measured at beam energy of approximately 45 MeV.

CHAPTER 4.
CONCLUSION

This thesis has described the design and performance of the high intensity electron injector (CID) for the SLAC Linear Collider (SLC). This injector successfully captures 5.5×10^{10} electrons into a single S-band RF crest. The gun pulses twice, 59 ns apart, producing two 6 amp, 2 ns FWHM pulses. These pulses are compressed by a factor of 100 through a series of bunching elements comprised of two gap-and-drift prebunchers at the 16th subharmonic of S-band, a traveling wave buncher with phase velocity $\beta_w = .75$, and a velocity-of-light capture region. By judicious choice of RF phases, we can capture 90% of the charge into a $\pm 1\%$ energy spread at the entrance to the damping ring. This bunching and capture of 5.5×10^{10} electrons into the damping ring longitudinal admittance is accomplished without causing unacceptable transverse emittance growth. The invariant transverse emittance at the end of CID is 1.5×10^{-4} radian-meters in both the horizontal and vertical planes, a factor of two below the design limit. The collider injector meets all of the specifications outlined in the introduction.

The computer code RINGMODEL was used to simulate the longitudinal beam dynamics in each of the four bunching elements. The simulation predicts the calculated bunch shape of Fig. 3.13 for the operating conditions specified in Table 3.5. While the calculated base width and total charge are in good agreement with experiment, the calculated FWHM and rise times are about half the measured values. We suspect that the streak camera signal has suffered significant resolution degradation, masking a fast (~4-5 ps) rise time seen at an earlier time with another streak camera.[19]

The general approach to injector design presented in this text, a thermionic gun followed by a series of bunching elements at increasing subharmonic frequencies of the accelerator RF, was completely adequate to meet the SLC specifications and required no development of unproven technologies. It was, therefore, a sound choice. Using one or two more bunching elements might lead to another factor of ten in peak current, but currents beyond this will require new approaches, such as laser-induced photoemission of high current, picosecond bunches directly from a solid state cathode or stacking bunches in a small storage ring, or other novel solutions.

APPENDIX A
STREAK CAMERA OPTICS AND RESOLUTION

The length of the CID electron bunch is measured by letting it pass through a quartz radiator just downstream of the compressor magnets (see Fig. 3.1).[28] The beam gives off Cherenkov light, which is transported through an optical system to a streak camera. The quartz radiator is 1.5 meters downstream of the last quadrupole and it is thus impossible to form a small (~1 mm) spot at its location. Both the intensity and resolution of the signal at the streak camera are affected by the relatively large spot size (~1 cm) at the quartz. The light transport optics system is described below and resolution limits are discussed. As shown in Fig. A.1 the electron bunch passes through a 1 mm-thick quartz radiator and gives off Cherenkov radiation. The intensity of the Cherenkov radiation is proportional to the current in the bunch. The direction of propagation of the Cherenkov light relative to the beam velocity vector is given by the Cherenkov angle

$$\theta_c = \arccos \frac{1}{\beta n} = 45^\circ \qquad (A.1)$$

where

β = velocity of the electron bunch

n = 1.41 = index of refraction of visible light in quartz.

The optics of the light transport system is simplified if the quartz is oriented so that the direction of propagation of the Cherenkov light is normal to the quartz/vacuum interface. In this case the angle of incidence and the angle of refraction across the interface are both zero. Thus we chose to tilt the quartz through an angle $90 - \theta_c$ with respect to the beam line (see Fig. A.2).

After leaving the quartz, the light passes through an optical system with a 90° focusing lattice. This lattice consists of four 4 cm diameter lenses with two meter focal lengths, spaced approximately four meters apart. The 90° lattice is followed by a 22 cm drift space, a lens with a focal length of 4.6 cm and a 5.8 cm

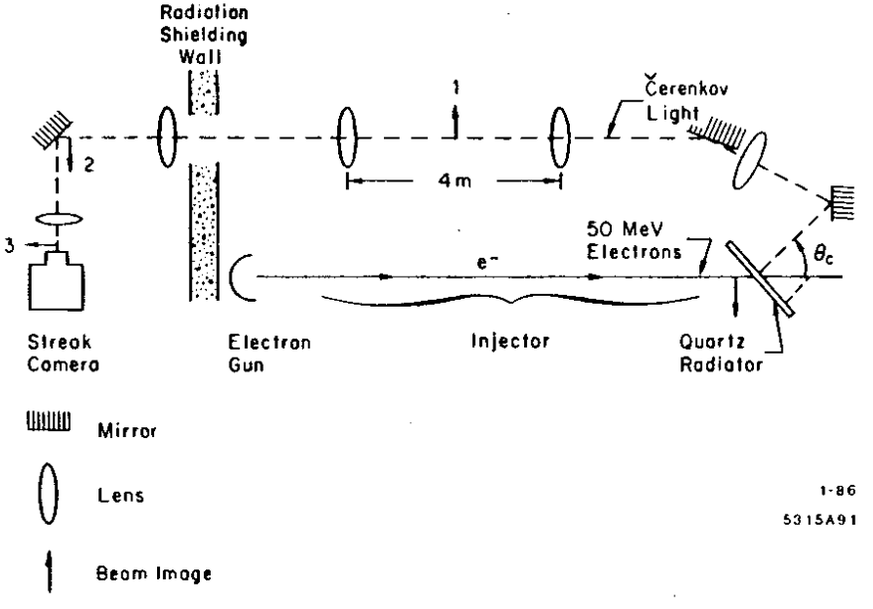

Fig. A.1 Optical system used to measure CID bunch length.

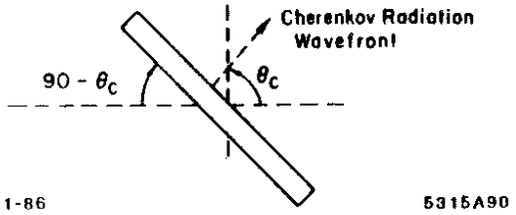

Fig. A.2 Direction of Cherenkov wave front.

drift designed to produce a demagnified ($M = 0.3$) image of the Cherenkov light at the slit of the streak camera. Resolution of the bunch length as measured by the streak camera is limited by four effects:

1. Broadening due to the finite width of the quartz,
2. Broadening due to the finite width of the camera slit,
3. Broadening due to error in the location of the beam image at the camera slit, and
4. Resolution limitations internal to the streak camera.

Because of the large beam spot size at the quartz radiator and the finite thickness of the quartz slab, the Cherenkov light generated by electrons with the same longitudinal position in the bunch reaches the camera over a finite time ΔT_1. We can quantify ΔT_1 by careful examination of Fig. A.3. Assume that the width of the bunch is substantially greater than the width of the quartz. In addition, assume that the streak camera is a perfect pinhole camera (the resolution degradation due to finite slit width is discussed below). Two electrons at points (a) and (b) reach the same axial position in the beam pipe ($z = 0$) at the same time ($t = 0$). We are interested in the time at which photons radiated by these two electrons reach point (d), since only these electrons are detected by a pinhole camera at (e). The electron at point (a) at $t = 0$ arrives at (d) at $t_1 = (h/c\cos\theta_c)$ where h is the thickness of the quartz. Meanwhile, the electron at point (b) at $t = 0$ travels to (c) in time $t_2 = h\sin\theta_c\tan\theta_c/c$. At point (c) it radiates Cherenkov light which travels to (d) in time $t_3 = (nh/c) = (h/c\cos\theta_c)$. Although the two electrons are at $z = 0$ at $t = 0$, the Cherenkov signals reach the camera slit ΔT_1 seconds apart where ΔT_1 is given by

$$\Delta T_1 = (t_2 + t_3) - t_1 = \frac{h}{c}\sin\theta_c\tan\theta_c \quad . \tag{A.2}$$

For $h = 1$ mm and $\theta_c = 45°$, $\Delta T_1 = 2.4$ ps.

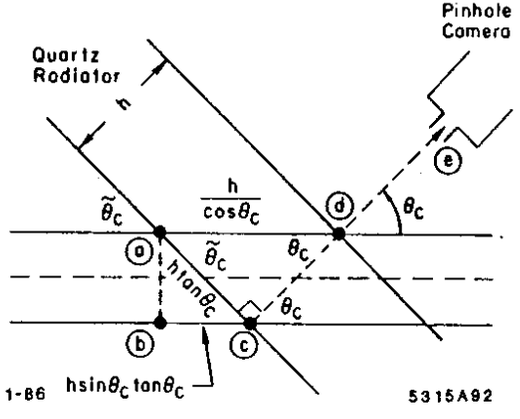

Fig. A.3. Image broadening due to finite width of quartz radiator. Photons radiated at points c and d enter the pinhole camera at point e, $h\sin\theta_c\tan\theta_c/c$ seconds apart.

The camera slit width causes resolution degradation which is proportional to the slit width and inversely proportional to the magnification of the light transport optics. For this calculation, assume the quartz radiator to be infinitely thin. As shown in Fig. A.4, electrons at (a) and (b) are at $z = 0$ at time $t = 0$. The electron at (a) crosses the quartz radiator at $t = 0$ and emits Cherenkov light. The electron from (b) arrives at (c) at a time Δt_2 later and crosses the quartz, radiating Cherenkov light. From Fig. A.4 we see

$$\Delta t_2 = \frac{w_s \sin\theta_c}{Mc} \tag{A.3}$$

where

w_s = camera slit width, and

M = image magnification in the optics system.

For $w_s = .01$ cm and $M = 0.3$, $\Delta t_2 = 1.1$ ps.

The resolution of the system worsens if the final image of the Cherenkov light is slightly in front of or behind the camera slit. To calculate this effect, we assume that all images are small compared to the diameter of the transport system lenses. From Fig. A.5(a) we see that rays which diverge from the axis at angles greater than $\theta = \theta_0$ do not remain in the light transport system. θ_0 is given by

$$\theta_0 = \frac{d}{L} \tag{A.4}$$

where

d = diameter of lenses 1-4 in Fig. A.5(a) = 3.8 cm

L = distance between lenses 1, 2, 3, and 4 in Fig. A.5(a) = 4 meters

From Fig. A.5(b) we see that rays which diverge from image 2 at an angle of θ_0 diverge from image 3 at an angle θ_1 given by

$$\theta_1 = \frac{\theta_0}{M} \doteq \frac{d}{LM} \tag{A.5}$$

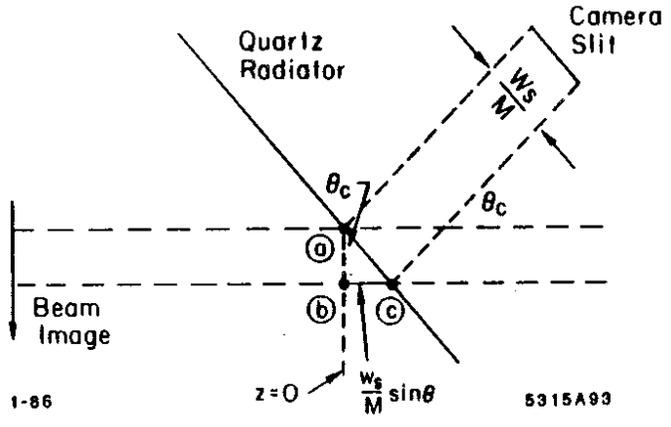

Fig. A.4. Image broadening due to finite width of camera slit.

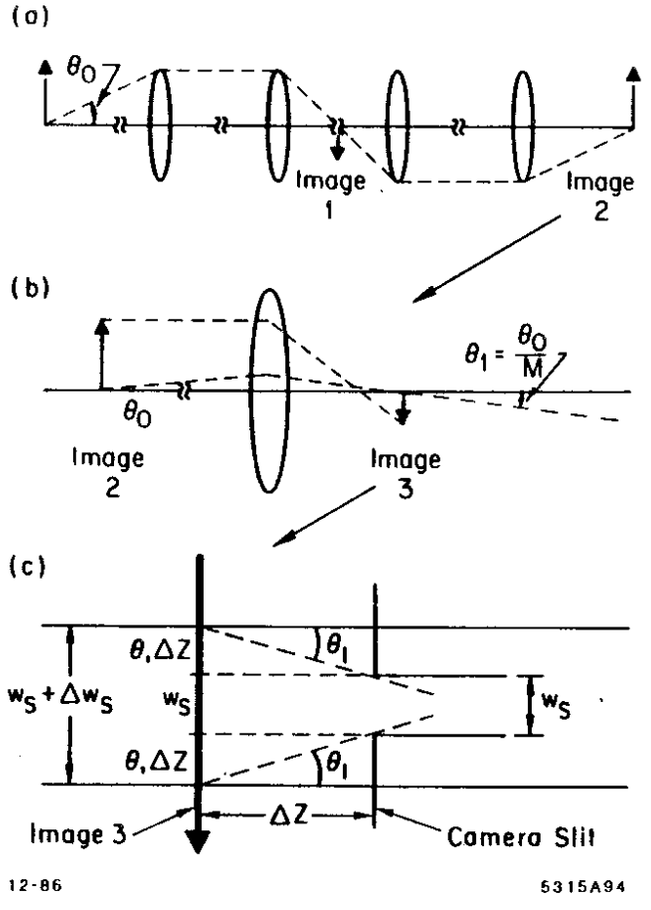

Fig. A.5. (a) Optics from source to second image; (b) Optics from second to third image; (c) Image broadening due to shift of final image to Δz cm in front of slit.

From Fig. A.5(c) we see that if image 3 is a distance ΔZ in front of (or behind) the camera slit, the image formed inside the camera is broadened by $2\theta_1 \Delta Z$. Thus the slit width of Eq. (A.3) is effectively increased by

$$\Delta w_s = 2\theta_1 \Delta Z = \frac{2d}{LM} \Delta Z \quad . \tag{A.6}$$

The additional resolution degradation due to Δw_s is given by Eqs. (A.3) and (A.6)

$$\Delta t_3 = \frac{2d \sin \theta_c}{LM^2 c} \Delta Z \quad . \tag{A.7}$$

The error in the position of the final image, ΔZ, results from two sources, uncertainty in the position of image 2 (Fig. A.1) and uncertainty in the position of the final lens. The slit position (relative to image 2) and focal length of the final lens were chosen to achieve a magnification of 0.3 for the final image. While this magnification increases resolution degradation, it is necessary to obtain a reasonable signal-to-noise ratio from the streak camera system. A magnification of 0.3 is achieved by choosing

f = focal length of final lens = 4.6 cm

p = distance from image 2 to final lens = 19.9 cm

q = distance from final lens to image 3 = 6.0 cm

The exact position of image 2 is difficult to measure, but we are confident in its position within ± 2 cm. If p is in error, the error in q is given by

$$q = \frac{1}{1/f - 1/p} \Rightarrow \frac{\Delta q}{\Delta p} = -\frac{f^2}{(p-f)^2} \quad .$$

For $\Delta p = 2$ cm, $\Delta q = .09$ cm, or 1 mm of error.

Uncertainty in the position of the final lens with respect to the slit is no more than ± 2 mm. Thus the error in position of the final image is given by

$$\Delta Z \leq .1 \text{ cm} + .2 \text{ cm} = .3 \text{ cm} \quad .$$

This gives a resolution degradation of [Eq. (A.7)]

$$\Delta t_3 = 5.0 \times .3 = 1.6 \text{ ps} \quad .$$

In addition to the external optics system, the camera itself has optical and electronic resolution limitations. In a non-sweeping mode (focus) the camera illuminates a narrow portion of its reticon array with a roughly Gaussian signal. The signal is 10-12 channels FWHM, which corresponds to 1.7 – 3.2 ps on the (20 ps/mm) sweep speed and to 7.0 – 8.4 ps on the (50 ps/mm) sweep speed.

Combining these four resolution errors in the most straightforward way, we estimate the resolution degradation of the beam induced signal. Table A.1 shows resolution degradation for 5 and 15 ps signals at two different camera speeds.

Table A.1. Streak camera resolution.

Camera Focus (channels)	Sweep Speed (ps/channel)	Beam Signal (ps)	Resolution Degraded Signal
12	.27 (20 ps/mm)	5	$\sqrt{(5)^2 + (2.4)^2 + (1.1)^2 + (1.6)^2 + (3.2)^2}$ = 6.7 ps
		15	$\sqrt{15^2 + 19.8}$ = 15.6 ps
	.70 (50 ps/mm)	5	$\sqrt{(5)^2 + (2.4)^2 + (1.1)^2 + (1.6)^2 + (8.4)^2}$ = 10.3 ps
		15	$\sqrt{15^2 + 80.1}$ = 17.5 ps

REFERENCES

1. SLAC Linear Collider Conceptual Design Report, SLAC Report No. 229, June 1980.
2. SLC Design Handbook, SLAC Internal Document, December 1984.
3. G. E. Fischer, SLAC-PUB-3392, July 1984.
4. R. H. Miller *et al.*, IEEE Trans. Nucl. Sci. **NS-12**, 1965, p 804.
5. R. H. Miller *et al.*, The Stanford Two-Mile Accelerator, R. B. Neal, editor, W. A. Benjamin Inc., New York, 1968, pp 241-269.
6. G. Dôme, Electron Bunching by Uniform Sections of Disk-Loaded Waveguide, Part A: General Study. Technical Report M-242-A, Hansen Laboratories, Stanford, California, December 1960.
7. J. C. Slater, Review of Modern Physics **20**, p 473, 1948.
8. E. L. Chu, ML Report No. 140, W. W. Hansen Laboratories of Physics, Stanford University, Stanford, California.
9. A. J. Lichtenberg as referenced in Miller *et al.*, The Stanford Two-Mile Accelerator, *ibid.*
10. P. B. Wilson and K.L.F. Bane, SLAC Report PEP-226A (unpublished), March 1977.
11. A. T. Drobot *et al.*, IEEE Trans. Nucl. Sci **NS-32**, p 2733, October 1985.
12. M. B. James and R. H. Miller, IEEE Trans. Nucl. Sci. NS-28, p 3461, June 1981.
13. C. B. Williams and M. H. MacGregor, IEEE Trans. Nucl. Sci. NS-14, p 581, 1967.
14. G. Mavrogenes *et al.*, IEEE Trans. Nucl. Sci. **NS-20**, p 919, June 1973.
15. W. R. Smythe, Static and Dynamic Electricity, McGraw-Hill Book Company, New York, 1950.

16. W. B. Herrmannsfeldt, SLAC-Note-AP-41, April 1985.
17. R. H. Helm and R. H. Miller, Linear Accelerators, P. M. Lapostolle and A. L. Septier, editors, pp 115-145, North Holland Publishing Company, Amsterdam, 1970.
18. J. E. Clendenin *et al.*, Proceedings of the 1981 Linear Accelerator Conference, p 130, Los Alamos National Laboratory, 1981.
19. M. B. James *et al.*, IEEE Trans. Nucl. Sci. NS-30, p 2992, August 1983.
20. J. E. Clendenin *et al.*, Proceedings of the 1984 Linear Accelerator Conference, Seeheim/Darmstadt, Federal Republic of Germany, 1984.
21. M. C. Ross *et al.*, IEEE Trans. Nucl. Sci. **NS-32**, p 3160, October 1985.
22. R. F. Koontz *et al.*, IEEE Trans. Nucl. Sci. **NS-28**, p 2213, 1981.
23. R. F. Koontz, Proceedings of the 1981 Linear Accelerator Conference, p 64, Los Alamos National Laboratory, 1981.
24. SUPERFISH Calculation by Richard Early, SLAC.
25. G. A. Loew *et al.*, The Stanford Two-Mile Accelerator, *ibid.*
26. G. A. Loew and J. W. Wang, IEEE Trans. Nucl. Sci. **NS-32**, p 3228, October 1985.
27. J. C. Sheppard *et al.*, IEEE Trans. Nucl. Sci. **NS-30**, p 2161, August 1983.
28. J. C. Sheppard *et al.*, IEEE Trans. Nucl. Sci. **NS-32**, p 2006, October 1985.